DISSERTATION

EXPLORATION OF NITRIC OXIDE GENERATION FROM *S*-NITROSOGLUTATHIONE FOR THE ADVANCEMENT OF ANTI-FOULING GLUCOSE BIOSENSOR MEMBRANE MATERIALS

Submitted by

Alyssa C. Melvin

Department of Chemistry

In partial fulfillment of the requirements

For the Degree of Doctor of Philosophy

Colorado State University

Fort Collins, Colorado

Summer 2022

Doctoral Committee:

Advisor: Melissa M. Reynolds

Joseph Zadrozny
Delphine Farmer
Thomas Chen

ABSTRACT

EXPLORATION OF NITRIC OXIDE GENERATION FROM *S*-NITROSOGLUTATHIONE FOR THE ADVANCEMENT OF ANTI-FOULING GLUCOSE BIOSENSOR MEMBRANE MATERIALS

Blood-contacting medical devices such as implantable glucose sensors suffer from biofouling which limits the lifetime of the device and puts the patient at risk of arterial embolism and infection. Researchers have been developing medical device coatings to address the two causes of surface biofouling: thrombus and biofilm formation. One promising strategy is surface-localized production of nitric oxide (NO), a biomolecule with antithrombotic and antibacterial physiological functions, as a multifunctional therapeutic for biofouling prevention. Because NO is a gaseous free radial with a very short physiological half-life, achieving localized NO generation presents a clear challenge. An innovative approach that will be explored herein is incorporating catalysts on the medical device surface that release NO from endogenous NO sources, *S*-nitrosothiols (RSNOs). A water stable copper-based metal–organic framework (MOF) CuBTTri, Cu(II) benzene-1,3,5-tris(1*H*-1,2,3-triazoy-5-yl), has been shown to be an effective catalyst for the generation of NO from RSNOs. Two RSNOs, *S*-nitrosoglutathione (GSNO) and *S*-nitroso-*N*-acetylpenicillamine (SNAP), are commonly used in the development of new NO-generating materials. It is known that RSNOs are susceptible to decomposition by stimuli including heat, light, and trace metal ions which can inadvertently be introduced through basic handling, storage conditions, and experimental setups. Despite their frequent use, there is limited and conflicting literature examining the comparative stability of GSNO and SNAP. In order to

accurately characterize and quantify the behavior of NO-generating materials, reliable and robust methods must be developed to prevent spontaneous RSNO decomposition under the desired experimental conditions. In Chapter 2, the comparative stability of GSNO and SNAP was thoroughly examined to inform subsequent experiments in the development of CuBTTri-based anti-fouling materials with RSNOs as the NO source. Though CuBTTri is an effective catalyst for this reaction, solid state material must be immobilized into a flexible, processable scaffold for coating devices. In Chapter 3, the effects of incorporating CuBTTri into a medical grade polyurethane composite material on NO generation is explored. In Chapter 4, the effects of three key parameters of CuBTTri composite materials, MOF particle size, MOF loading, and polymer concentration, on NO generation are evaluated to assess the tunability of these next-generation materials. In Chapter 5, the effects of the CuBTTri/polyurethane composite material on the enzyme function and analytical performance of a glucose biosensor are examined. Though metal ion-promoted NO release from RSNOs is promising strategy for the development of NO-generating materials, the majority of studies focus on copper, and few have surveyed the ability of other common metal ions to produce this effect. Finally, in Chapter 6, NO generation from GSNO by Cu^{2+} and twenty transition and post-transition metal ions was monitored using NO-selective chemiluminescence-based detection to expand the range of potential metals for the development of NO-based anti-fouling materials.

ACKNOWLEDGEMENTS

Individual contributions and funding sources:

Chapter 2: TGA measurements were performed by W. Matthew Jones. NMR and FTIR analyses were performed by Alec Lutzke. Mass spectrometry was performed by Christopher Allison. All other work was carried out by Alyssa Melvin. Funding for this research was supported by the National Science Foundation (DGE-1450032) and National Institutes of Health (5R01HL140301-02).

Chapter 3: H_3BTTri was synthesized by Jon Thai and Tracey Wick. GSNO was synthesized and characterized by Maga Mohnike. Robert Tuttle assisted in the preparation of the manuscript. All other work was carried out by Alyssa Melvin. Funding for this research was supported by the National Institutes of Health (1R01HL140301-01).

Chapter 4: H_3BTTri was synthesized by Jon Thai and Tracey Wick. GSNO was synthesized and characterized by Maga Mohnike. All other work was carried out by Alyssa Melvin Funding for this research was supported by the National Institutes of Health (1R01HL140301-01).

Chapter 5: H_3BTTri was synthesized by Jon Thai and Tracey Wick. GSNO was synthesized and characterized by Maga Mohnike. All other work was carried out by Alyssa Melvin. Funding for this research was supported by the National Institutes of Health (1R01HL140301-01).

Chapter 6: NOA measurements at 250 μM GSNO were performed by Megan Neufeld. GSNO and SNAP syntheses and NMR analysis were performed by Alec Lutzke. Mass spectrometry was performed by Christopher Allison. ICP-AES analysis was performed by the

Soil, Water and Plant Testing Laboratory at Colorado State University. All other work was carried out by Alyssa Melvin. Funding for this research was funded by the National Science Foundation (DGE-1450032 and 1352201), the Monfort Family Foundation, and the National Institutes of Health (5R21EB016838- 02).

TABLE OF CONTENTS

CHAPTER 1

INTRODUCTION

1.1 Overview

Blood is complex mixture of plasma, erythrocytes, leukocytes, and platelets. When designing a material for blood-contacting medical devices (e.g. sensors, catheters, dialyzers, stents), the material must be hemocompatible, meaning that it will not cause a negative reaction with any component of blood, according to the standards set by the International Organization for Standardization (ISO 10993-4).[1] ISO designates five test categories (thrombosis, coagulation, platelets, hematology, and complement system) in order to evaluate hemocompatibility, and appropriate tests are selected based on the features of the particular device to evaluate safety and efficacy prior to clinical studies. Despite substantial improvements to the international standards in 2017 and promising advancements by researchers, an ideal biocompatible material has yet to be designed and implemented.[2-4]

1.2 Enzymatic Glucose Biosensors

1.2.1 Electrochemical Glucose Sensor Overview

Implantable glucose sensing devices have been an active area of research in recent years as a more effective way for diabetic patients to monitor their blood glucose levels.[5-9] These devices record blood glucose levels in real-time compared to the traditional method of measurement which requires relies on the patient to draw blood from finger prick at frequent intervals throughout the day. Glucose sensors can be implanted subcutaneously or intravenous; subcutaneous implantation is the less invasive option but suffers from the time delay of blood glucose diffusion into interstitial fluid that is required for measurement.[10] For critically-ill

patients, intravascular implantation is ideal so that any acute changes in blood glucose levels can be treated immediately. However, as with all blood-contacting medical devices, biofouling at the artificial sensor surface begins immediately after implantation, ultimately resulting in the formulation of life-threatening blood clots and/or biofilm formation.[11] This phenomenon also impacts the analytical performance of the sensor by reducing the mass transport of glucose to the electrode for measurement.

1.2.2 Needle-Type Glucose Sensor

A modern needle-type electrochemical glucose biosensor was developed in the 1990s which remains a useful platform for glucose sensing research (Fig. 1.1).[12,13] It consists of a silver-silver chloride reference electrode and a platinum-iridium (Pt-Ir) working electrode. At one end of the Pt-Ir, an inner polymer layer consisting of alternating layers of Nafion (charge exclusion) and cellulose acetate (size exclusion). The enzyme layer consists of glucose oxidase enzyme (GOx) crosslinked with bovine serum albumin by glutaraldehyde. The outer polymer layer consists of a biocompatible semipermeable membrane.

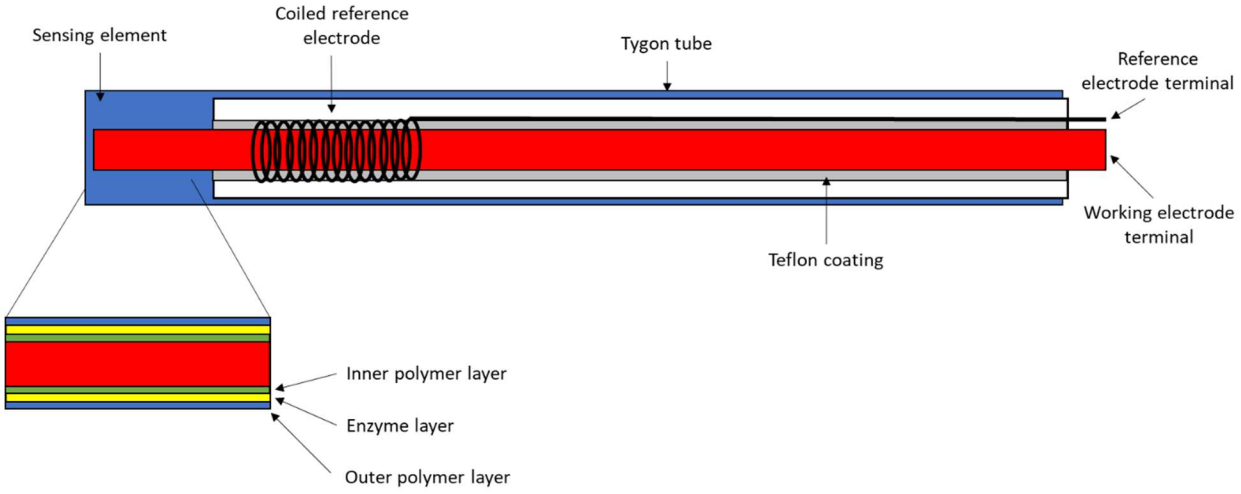

Figure 1.1. A needle-type electrochemical enzymatic glucose sensor.

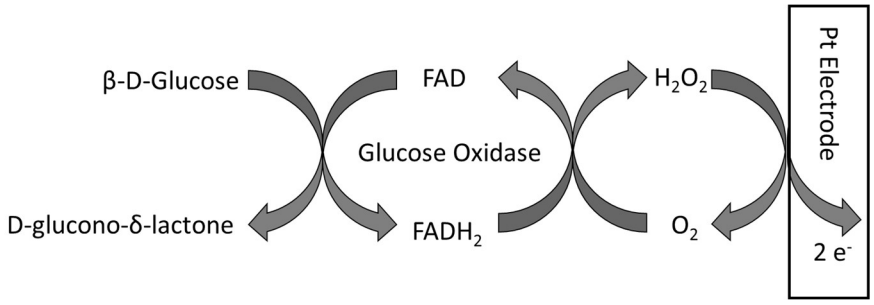

Figure 1.2. Sensing mechanism of a first generation glucose biosensor.

A general schematic of the sensing mechanism of this first-generation glucose biosensor is depicted in Fig. 1.2.[14] In blood, glucose passes through the outer polymer membrane to the enzyme layer. Glucose is oxidized by the FAD cofactor of GOx to gluconolactone. $FADH_2$ reacts with oxygen to produce hydrogen peroxide. A potential of at least +0.6 V is applied to the platinum electrode, oxidizing hydrogen peroxide, producing two electrons (Eqn. 1.1). The electrons produce a current at the working electrode relative to the current produced by the reference electrode (Eqn. 1.2) which can be correlated to glucose concentration.

$$H_2O_2(aq) \rightarrow O_2(g) + 2H^+(aq) + 2e^- \qquad \text{Eqn. 1.1}$$

$$2AgCl(s) + 2e^- \rightarrow 2Ag(s) + 2Cl^-(aq) \qquad \text{Eqn. 1.2}$$

Because of the complexity of the glucose sensing mechanism, the outer polymer membrane plays a key role in the performance of the sensor. It must be permeable to glucose and oxygen, minimize permeation from interferent species, and resist biofouling—the spontaneous accumulation of biological matter which prevents the diffusion of glucose to the sensor surface, resulting in inaccurate measurements and sensor failure.[11]

1.3 Biocompatibility Challenges of Blood-Contacting Medical Devices

1.3.1 Medical Device-Induced Thrombosis

All intravenous medical devices such as implantable glucose sensors suffer from

biofouling, or incidence of infection and thrombosis, which inhibits device function and places the patient at risk for developing severe complications.[15] Medical device-induced thrombosis is caused by the attachment of fibrin, platelets, and cells to a blood-contacting surface, resulting thrombus formation which begins immediately upon contact with blood (Fig. 1.3).[33] Ultimately, this adverse reaction limits the lifetime of implanted devices and has potential to lead to further, more serious complications such as arterial embolism. Thrombus formation proceeds through a series of processes that begins with plasma protein adsorption to the surface.[16] Protein adsorption is described by the Vroman effect; highly abundant proteins adsorb rapidly but are eventually replaced by proteins with lower relative abundance but greater affinity for the surface.[17,18] Fibrinogen is one of the first proteins to adsorb to the surface but is displaced by other proteins such as high molecular weight kininogen.[19] Platelet adhesion is facilitated by proteins with a specific amino acid sequence, such as fibronectin, von Willebrand factor and, most critically, fibrinogen.[20] Typically, for platelets to bind with fibrinogen, an integrin on the platelet surface (glycoprotein IIb-IIIa) must be activated; however, that is not necessary for fibrinogen adsorbed to artificial surfaces.[21] The activated, fibrinogen-bound platelets initiate a positive feedback loop in which multiple pathways contribute to and amplify platelet thrombus formation: platelet adhesion, activation, and aggregation; adhesion and degranulation of leukocytes; and passive attachment of red blood cells.[16] The final phase of coagulation is achieved through activation of the contact system. A cascade of reactions generates fibrin monomers from fibrinogen which polymerize into fibrin strands, forming a platelet–fibrin thrombus. Further, activation of the complement system is linked to coagulation, which promotes leukocyte adhesion and activation on artificial surfaces. At this stage, device failure is inevitable, and incidence of an arterial embolism is possible.

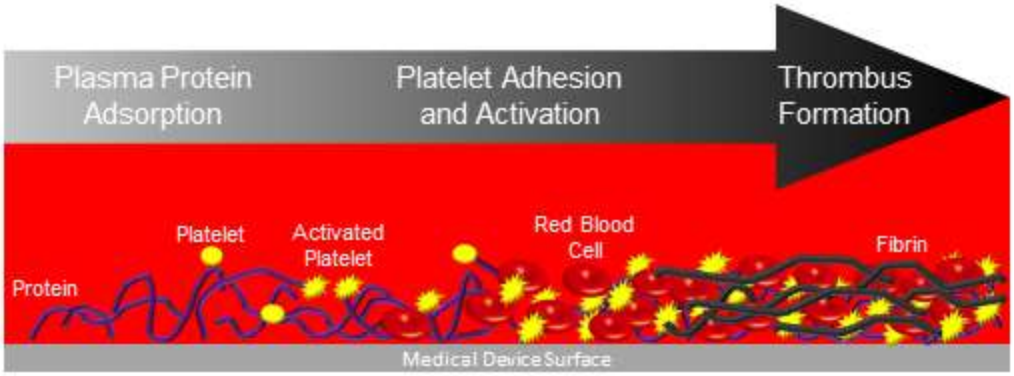

Figure 1.3. Progression of medical device-induced thrombosis.

In hospitals today, administration of anticoagulant drugs is the standard therapy to prevent thrombosis.[22] Unfractionated heparin and warfarin are the two most common drug treatment options; however, they have several limitations including the need for routine monitoring, dietary restrictions, and increased risk of bleeding.[22,23] Newer, promising alternatives include drugs such as dabigatran, fondaparinux, apixaban, edoxaban, and rivaroxaban or different ways of administering drugs such as lower dose anticoagulant therapy, extended treatment periods, or combination drug therapies.[22,24]

1.3.2 Medical Device-Associated Infections

The second cause of biofouling is medical device-associated infections. Indwelling blood contacting medical devices are prone to developing biofilms, the attachment and aggregation of bacteria to a synthetic surface.[15,16] Biofilm formation on surfaces occurs through the attachment of cells to the surface which form into multiple layers of bacteria with a complex, structured community protected by a polymeric matrix, and can ultimately result in the detachment of planktonic cells that spread to other locations causing infection.[26] There are a number of bacteria responsible for biofilm formation, but the most common sources of infection are from P. *aeruginosa,* P. *candida*, and, most notably, S. *aureus*.[27] Because of their highly protected

structure, biofilms are resistant to immune responses and traditional antibiotic treatments.[27] Preventing biofilm formation involves strict adherence to sterilization techniques and monitoring.

1.4 Strategies for Designing Anti-Fouling Materials

Because of the risks, limitations, and/or inadequacies of systemic drug treatments to alleviate biofouling complications, synthesizing anti-fouling materials is a superior, yet challenging, alternative solution. Strategies for synthesizing materials resistant to these effects typically involve surface modifications or eluting therapeutic drugs.

1.4.1 Surface Modifications for Anti-Fouling Materials

Surface modifications of materials involves altering the surface structure of medical device materials to prevent attachment of fouling agents. Successful examples include implementation of hydrophilic, hydrophobic, zwitterionic, or biomimetic surfaces.[5,28-30] Hydrophilic and zwitterionic polymer surfaces form a hydration layer through hydrogen bonding for the former and electrostatic interactions for the latter with the aqueous biological environment which minimizes the attachment of proteins and cells on the surface.[15] Hydrophobic polymers, alternatively, prevent adhesion of fouling agents through the incorporation of materials that repel water and hydrogen bonding. Biomimetic surfaces can be fabricated through a variety of means including micropatterning that mimics biological features of aquatic animals or deposition of biomolecules on the surface.[15,27] Though these materials show promise for reducing biofouling, the effectiveness tends to decrease over long-term blood contact.

1.4.2 Drug Eluting Surfaces for Anti-Fouling Materials

Materials can be functionalized to elute therapeutics such as antibiotics, immunosuppressants, and antiproliferative drugs to reduce the attachment of biofouling agents.[15]

Though this form of surface modification presents an active, targeted approach to reducing incidence of infection and thrombus formation, it has substantial drawbacks. Antiproliferative drugs can prevent healthy issue growth and sustained release of antibiotics can result in antibiotic resistance. And, as with surface modifications of polymers, the effectiveness of these materials is maintained over short time periods, limited by the drug loading capacity of the material.[31]

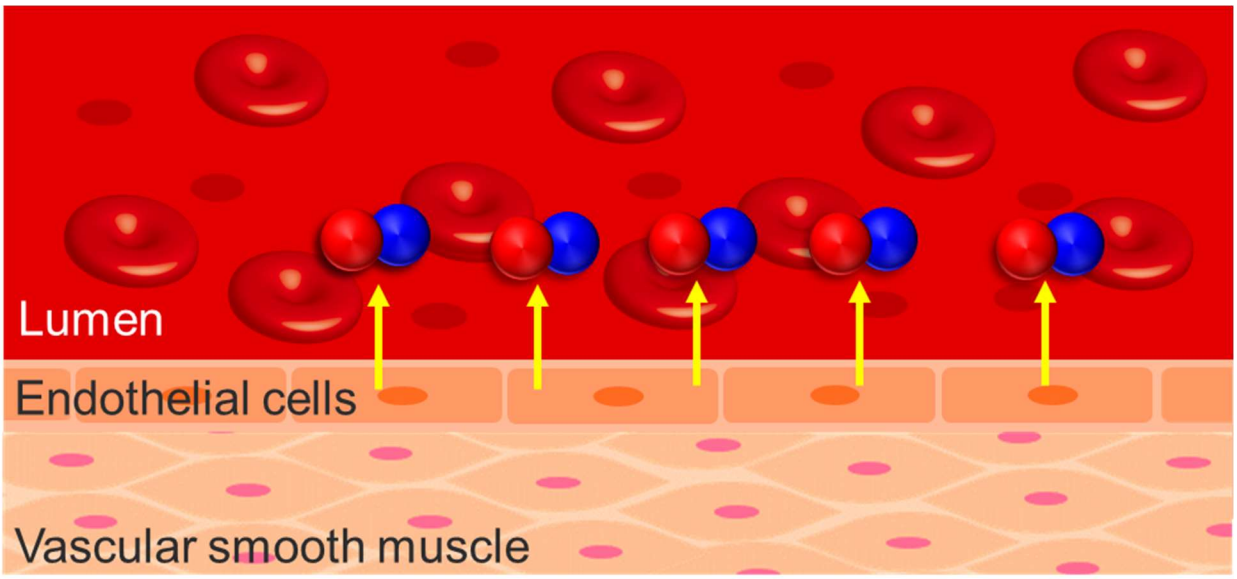

Figure 1.4. Endothelial NO flux.

1.4.3 Nitric Oxide as an Anti-Fouling Therapeutic

One therapeutic of particular interest for the design of drug-eluting surfaces is nitric oxide (NO). Nitric oxide plays a role in many aspects of physiology, particularly in the immune, cardiovascular, and nervous systems, and has well-established antithrombotic and antibacterial properties.[32-40] In the vascular endothelium, NO is synthesized by the enzyme endothelial nitric oxide synthase (eNOS or NOS III) by converting *L*-arginine to *L*-citrulline (Fig. 1.4), generating a flux of 0.05-0.4 nmol cm^{-2} min^{-1} to prevent the adhesion of platelets on the endothelium.[41,42]

On this basis, researchers have successfully demonstrated the use of artificially-induced NO release for reducing platelet adhesion, activation, and aggregation on synthetic blood-contacting polymeric surfaces.

Because NO is a reactive gaseous radical with a short half-life, NO is typically derived from NO donor compounds or macromolecular scaffolds for controlled NO delivery.[43-47] Common NO donor species include organic nitrates, organic nitrites, metal nitrosyl complexes, *S*-nitrosothiols (RSNOs), and *N*-diazeniumdiolates (NONOates) (Table 1.1), with RSNOs and NONOates being the most widely studied.[47-49] *S*-Nitrosothiols are endogenous NO donors, formed through *S*-nitrosation of cysteine residues on peptides and proteins.[50] Two commonly used RSNOs are *S*-nitrosoglutathione (GSNO), a bioavailable primary RSNO in mammalian blood, and *S*-nitroso-*N*-acetylpenicillamine (SNAP), a synthetic tertiary RSNO derived from the amino acid penicillamine (Fig. 1.5a and b).[40,51-59] These RSNOs are reported to exhibit sufficient stability as solids to permit handling and storage for prolonged periods of time.[60,61] It has been proposed that NO release from RSNOs occurs through homolytic cleavage of the S-N bond to form NO and thiyl radicals, and the latter product may dimerize to form the corresponding disulfide (Fig. 1.5c).

Table 1.1. Common NO donor species.

NO Donor	General Structure	Examples
Organic nitrates	$R–NO_2$	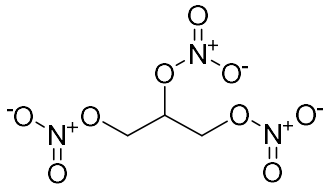 Glyceryl trinitrate
Organic nitrites	R–O–NO	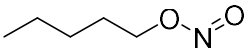 Amyl nitrite
Metal nitrosyl complexes	M–NO	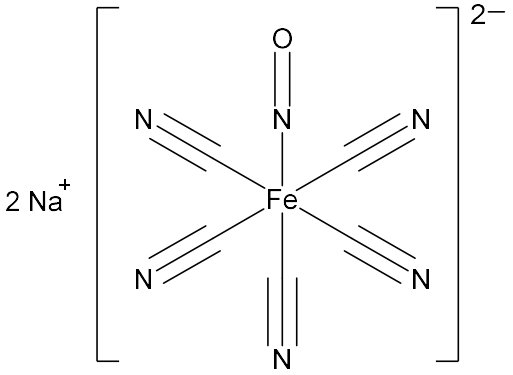 Sodium nitroprusside
S-Nitrosothiols (RSNOs)	R–S–NO	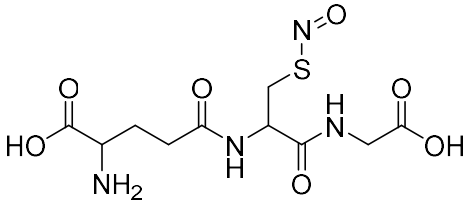 *S*-Nitrosoglutathione (GSNO)
N-Diazeniumdiolates (NONOates)	$R_2N[N(O)NO]^-$	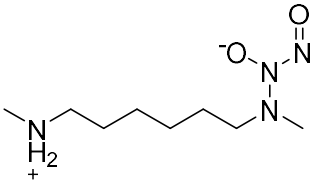 MAHMA/NO

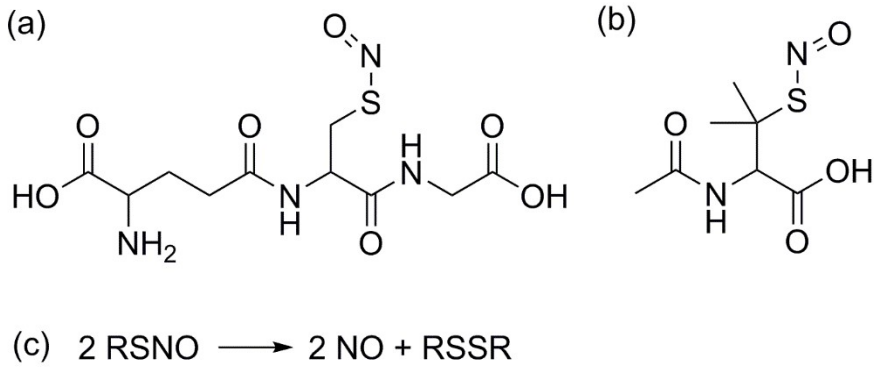

Figure 1.5. (a) *S*-Nitrosoglutathione (GSNO), (b) *S*-nitroso-*N*-acetyl-penicillamine (SNAP), (c) *S*-nitrosothiol (RSNO) decomposition.

1.4.4 Nitric Oxide-Releasing Materials

Researchers have approached the challenge of fabricating NO-releasing polymeric coatings using a variety of techniques.[62-68] Popular techniques involve either the covalent attachment or noncovalent impregnation of NO donor species with medical-grade polymers. For example, The Meyerhoff group prepared biomedical coatings comprised of a polymethacrylate copolymer with covalently attached diazeniumdiolate species.[69] In 2017 the same group achieved stable, long-term (14 days) NO release by impregnating the biocompatible medical grade polymer CarboSil 20 80A with SNAP.[70] They also showed that intravascular catheters prepared with the composite coating exhibited a 96% reduction in thrombus area compared to the control after 7 h of implantation in a rabbit.

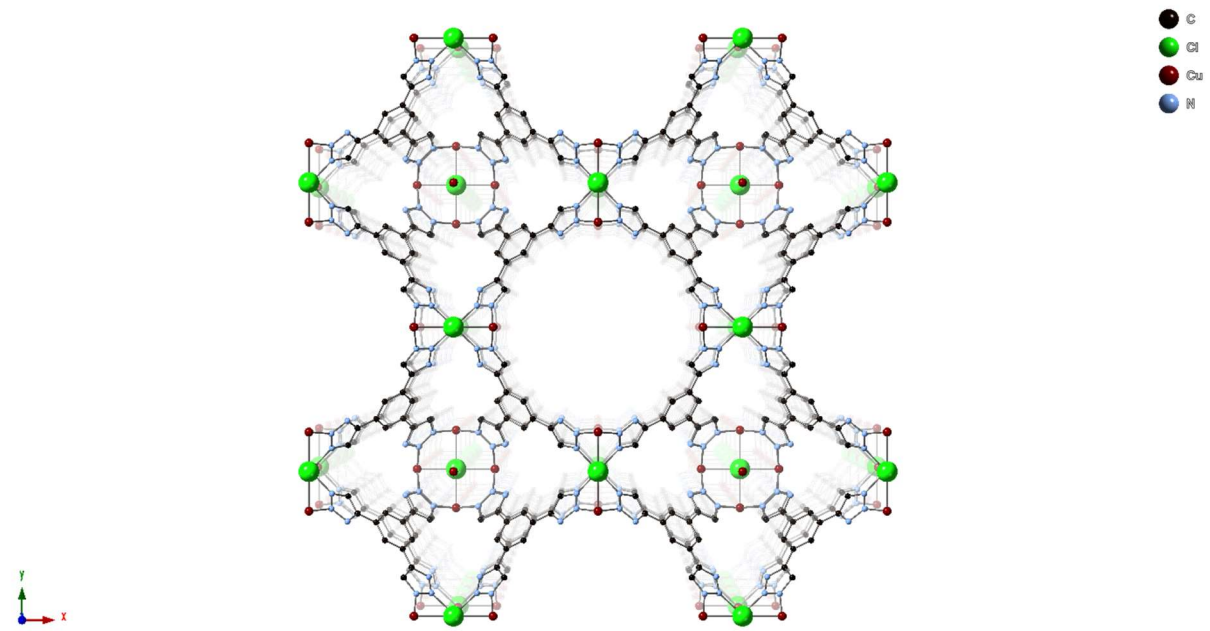

Figure 1.6. Cu(II) 1,3,5-Benzene-tris-triazole (CuBTTri) crystal structure.

Arguably the most promising strategy for fabricating NO-releasing materials is the catalytic generation of NO from endogenous NO donors to overcome the limitations of drug eluting materials by harvesting the antibacterial and antiplatelet therapeutic from the surrounding biological environment.[64,67] A copper-azolate metal–organic framework (MOF) CuBTTri, $H_3[(Cu_4Cl)_3(BTTri)_8]$ (H_3BTTri = 1,3,5-tris(1*H*-1,2,3-triazol-5-yl)benzene) (Fig. 1.6), has been shown to catalyze the oxidation of GSNO to generate NO alone and embedded within polymeric matrices.[71-75] Metal–organic frameworks are crystalline coordination polymers consisting of metal centers connected by organic linkers.[76] The tunable, highly ordered, and porous nature of these materials makes them favorable for a variety of applications from gas storage to catalysis. MOFs have been employed as heterogeneous catalysts extensively in recent years due to their distinctive physical properties including rational design/tunability, structural diversity, and coordinatively unsaturated metal sites.[77]

As MOF applications continue to expand, hybrid MOF/polymer composite materials (also referred to as mixed-matrix membranes, MMMs) have attracted attention as an effective way to incorporate the solid-state material on devices for commercial or industrial applications by merging the functionalities of MOFs with the flexibility and processability of polymers.[78-81] Various synthetic methods such as polymer grafting to or from MOFs, polymerizing within MOFs, and polymer templating MOFs have been employed to fabricate these hybrid materials; though the most widely-used conventional method involves dispersing solid MOF particles in a polymer solution.[81-86] This method is attractive for its relative ease, accessibility, and tunability, and has been demonstrated for a range of MOF and polymer combinations.[82,87-89] But poor interactions between the two phases can result in agglomerations of MOF particles during the fabrication or evaporation process.[82] Reducing MOF particle size, altering MOF particle morphology, priming the MOF particles with the polymer solution, and slowing the evaporation rate of the solvent are a few strategies to improve the uniformity of these films. For catalytic MOFs, composites provide the benefit of increased catalyst stability and recoverability, but must retain its desired catalytic properties.[78,87,90] Compared to the powder MOF system, the catalytic performance of the polymer-embedded systems has been shown to range from moderately reduced[91] to sustained[87] to moderately enhanced.[92]

1.4.5 Nitric Oxide Quantification

NO release can be measured indirectly by measuring RSNO decomposition or using a Griess assay with ultraviolet visible spectroscopy (UV-Vis) or directly using NO-specific chemiluminescence-based detection using nitric oxide analyzers (NOAs).[93,94] Nitric oxide analyzers are more sensitive and selective for NO detection than spectroscopy techniques. In brief, NO is generated in the reaction vessel and enters the reaction chamber of the NOA where it

reacts with artificially-generated ozone to produce oxygen gas and nitrogen dioxide in the excited state (Eqn. 1.3).[95-97] As the nitrogen dioxide relaxes to the ground state, a photon is emitted (Eqn. 1.4). The photon is amplified by the photomultiplier tube and the signal is exported as an electrical potential in mV which is converted to concentration (e.g., ppb or ppm) and plotted against time. Using an instrument-specific calibration constant in ppb mol^{-1} s^{-1} and the known amount of NO donor added to the system, quantitative measurements can be collected for NO-generating systems.

$$NO + O_3 \rightarrow NO_2^* + O_2 \qquad \text{Eqn. 1.3}$$

$$NO_2^* \rightarrow NO_2 + h\nu \qquad \text{Eqn. 1.4}$$

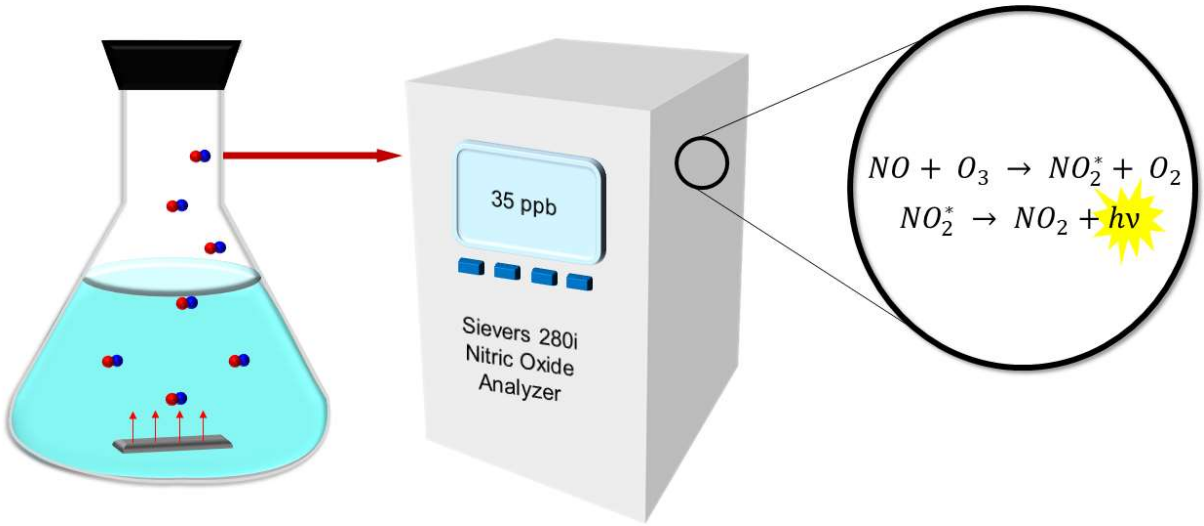

Figure 1.7. Schematic representation of NO quantification using a nitric oxide analyzer (NOA).

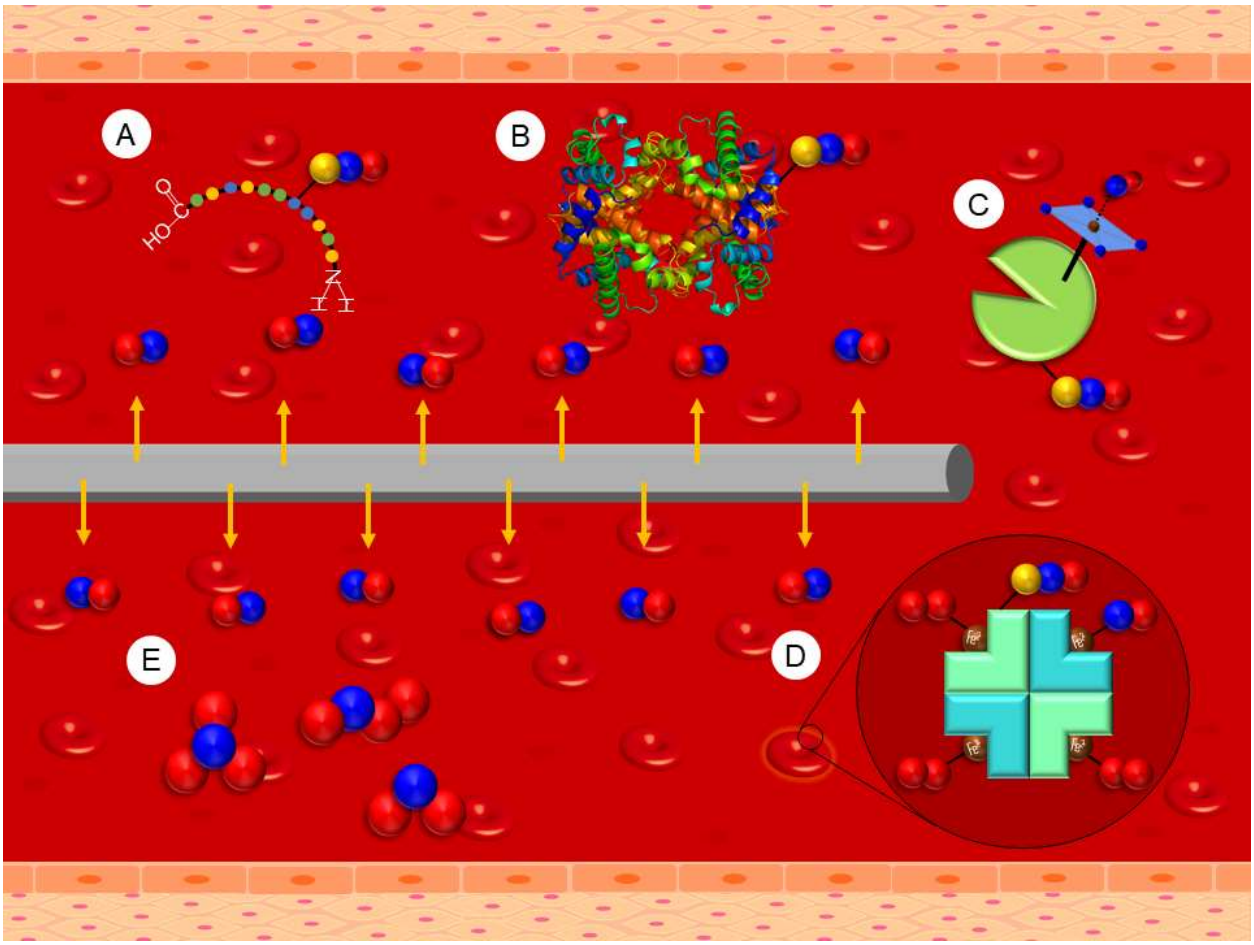

Figure 1.9. Schematic representation of NO reactions near a vascular implanted NO releasing glucose sensor. A) peptide RSNO, B) protein RSNO, C) enzyme nitrosylation and enzyme RSNO, D) hemoglobin nitrosylation and *S*-nitrosohemoglobin, E) reactive nitrogen species formed through the reactions of oxygen and NO species.

1.5 Overview of Reactions with NO at Sensor Surface

Blood is a complex mixture composed of 55% plasma, 44% erythrocytes, and 1% leukocytes and platelets. Plasma is 90% water with the remaining 10% being a mixture of proteins, inorganic species (e.g., ions and dissolved gases), and organic species (e.g., metabolites and waste products). Because it is known to serve many physiological functions, it is imperative to understand the range of reactions in which NO can participate. Herein, the reactivity of NO in blood at pH 7.4 conditions are described (Fig. 1.8).

Despite being a gaseous free radical, the reactivity of NO under physiological conditions is limited to a few cellular targets, as it is a poor oxidizing agent, reducing agent, and nucleophilic agent.[98] Three key properties of NO dictate its physiological roles: small molecular size, electrical neutrality, and presence of an unpaired electron in a nonbonding molecular orbital (Table 1.1 and Fig. 1.9).[99]

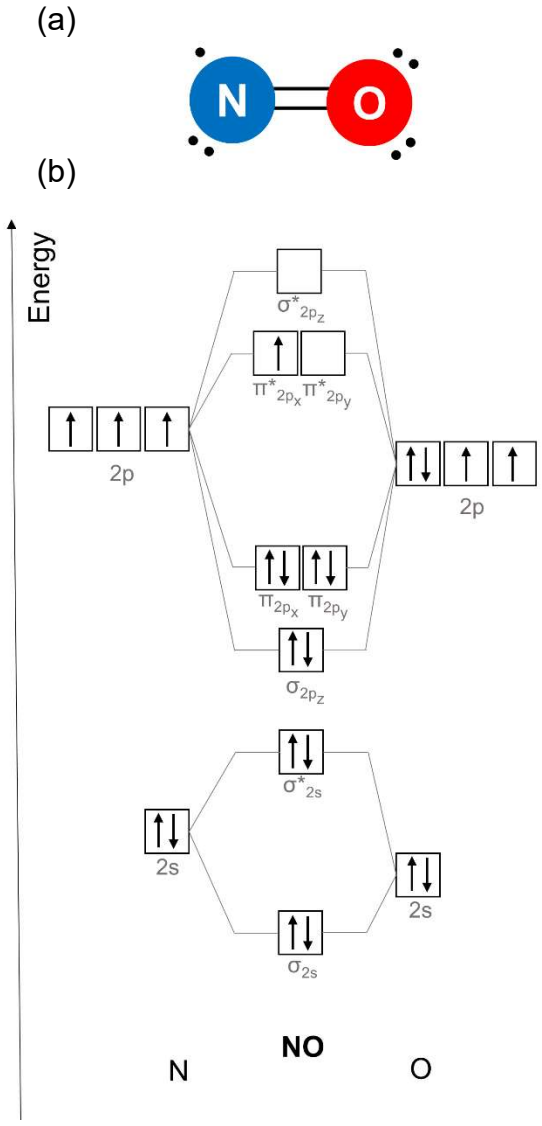

Figure 1.9. a) Lewis dot structure and b) molecular orbital bonding diagram for nitric oxide.

1.5.1 Reaction of NO with Ferrous Heme

The simple association of NO with transition metal ions (M^{n+}), known as nitrosylation (Eqn. 1.5), is the primary mechanism underlying many of the biological functions of NO.

$$\boldsymbol{NO} + M^{n+} \rightleftharpoons \boldsymbol{NO}\text{—}M^{n+} \qquad \text{Eqn. 1.5}$$

One of the fastest, and most important, reactions of NO is the formation of a ferrous-nitrosyl complex in heme-containing proteins.[37,100-102] NO-mediated activation of the ferrous heme-containing cytosolic receptor soluble guanylate cyclase (sGC) is responsible for many diverse biological functions including smooth muscle relaxation, vasodilation, neurotransmission, immune responses, and inflammation.[38,103] Relevant to the current work, the inhibition of platelet aggregation is initiated by NO binding to the ferrous heme moiety in platelet sGC (Eqn. 1.6).[32,36,104-106]

$$\boldsymbol{NO} + sGC(Fe^{2+}) \rightleftharpoons sGC(Fe^{2+}\text{—}\boldsymbol{NO}) \qquad \text{Eqn. 1.6}$$

Similarly, activity of the heme-containing enzymes cytochrome p450 (CYP450) (Eqn. 1.7), nitric oxide synthases (NOS) (Eqn. 1.8), cytochrome *c* oxidase (CcOx) (Eqn. 1.9) are regulated through the formation of ferrous-nitrosyl complexes.[37]

$$\boldsymbol{NO} + CYP450(Fe^{2+}) \rightarrow CYP450(Fe^{2+}\text{—}\boldsymbol{NO}) \qquad \text{Eqn. 1.7}$$

$$\boldsymbol{NO} + NOS(Fe^{2+}) \rightarrow NOS(Fe^{2+}\text{—}\boldsymbol{NO}) \qquad \text{Eqn. 1.8}$$

$$\boldsymbol{NO} + CcOx(Fe^{2+}) \rightarrow CcOx(Fe^{2+}\text{—}\boldsymbol{NO}) \qquad \text{Eqn. 1.9}$$

NO also reacts with nonheme iron moieties. Enzymes such as aconitase that contain iron–sulfur clusters are susceptible to nitrosylation.[107,108]

1.5.2 Formation of Reactive Nitrogen Species

Table 1.2. Redox states of nitrogen species in biology.

Name	Nitrate	Nitrite	Nitric Oxide	Nitroxyl	Hydroxylamine	Ammonia
Chemical formula	NO_3^-	NO_2^-	NO	HNO	NH_2OH	NH_3
Nitrogen redox state	V	III	II	I	-I	-III

Under biological conditions, NO reacts with molecular oxygen to form strong oxidizing agents known as reactive nitrogen species (RNS) (Tables 1.2 and 1.3).[98,109-112] Nitric oxide reversibly react with oxygen to form peroxynitrite radical (ONOO) (Eqn. 1.10). ONOO can react with a second molecule of NO to form two molecules of nitrogen dioxide (NO_2) (Eqn. 1.11). Nitrogen dioxide (NO_2) reversibly react with a second molecule of NO_2 to form dinitrogen tetroxide (N_2O_4) (Eqn. 1.12) or with NO to form dinitrogen trioxide (N_2O_3) (Eqn. 1.13). Water reacts with N_2O_3 to form nitrite (NO_2^-) (Eqn. 1.14) or with N_2O_4 form NO_2^- and nitrate (NO_3^-) (Eqn. 1.15). NO can also react with superoxide to generate peroxynitrite ($ONOO^-$) (Eqn. 1.16). $ONOO^-$ can reversibly form peroxynitrous acid (ONOOH) which decomposes into NO_3^- (Eqn. 1.17) or react with NO to form NO_2^- and NO_2 (Eqn. 1.18).

$$\boldsymbol{NO} + O_2 \rightleftharpoons ONOO \qquad \text{Eqn. 1.10}$$

$$\boldsymbol{NO} + ONOO \rightarrow 2\,NO_2 \qquad \text{Eqn. 1.11}$$

$$2\,NO_2 \rightleftharpoons N_2O_4 \qquad \text{Eqn. 1.12}$$

$$\boldsymbol{NO} + NO_2 \rightleftharpoons N_2O_3 \qquad \text{Eqn. 1.13}$$

$$N_2O_3 + H_2O \rightarrow 2\,NO_2^- + 2\,H^+ \qquad \text{Eqn. 1.14}$$

$$N_2O_4 + H_2O \rightarrow NO_2^- + NO_3^- + 2\,H^+ \qquad \text{Eqn. 1.15}$$

$$\boldsymbol{NO} + O_2^- \rightarrow ONOO^- \qquad \text{Eqn. 1.16}$$

$$ONOO^- \rightleftharpoons ONOOH \rightarrow NO_3^- + H^+ \qquad \text{Eqn. 1.17}$$

$$\boldsymbol{NO} + ONOO^- \rightarrow NO_2^- + NO_2 \qquad \text{Eqn. 1.18}$$

Table 1.3. Reduction potentials of select RNS.[98]

Radical Species	Reduction Potential (E°', V)
NO/NO^-	−0.80
$ONOO/ONOO^-$	0.40
NO_2/NO_2^-	1.04

1.5.3 Nitric Oxide Reactions with Proteins and RSNO Formation Pathways

NO bonds with cysteine residues in peptides and proteins to form RSNOs.[40,113] Several mechanisms for RSNO formation have been proposed, the majority of which favor reactions involving reactive nitrogen species or enzymes, rather than the direct interaction of thiol moieties with NO. The direct reaction of NO with a cysteine thiol moiety is considered a plausible, though likely minor, pathway for RSNO formation.[40] The initial attack involves the addition of NO to the thiol (RSH) to form an aminoxyl radical (RSNOH·) (Eqn. 1.19), then molecular oxygen acts as the electron acceptor to form an RSNO.

$$RSH + \boldsymbol{NO} \rightarrow RSNOH\cdot \qquad \text{Eqn. 1.19}$$

A second proposed mechanism is a radical-radical addition of NO to a previously-oxidized thiyl radical (RS·) (Eqn. 1.20).[40]

$$RS\cdot + \boldsymbol{NO} \rightarrow RSNO \qquad \text{Eqn. 1.20}$$

A third proposed mechanism involves the copper-containing enzyme ceruloplasmin (CP).[113] In this reaction, NO is oxidized by the copper(II) prosthetic group in CP (CP(Cu^{2+})) to form nitrosonium (NO^+) (Eqn. 1.21), which can react with a thiol moiety to form an RSNO (Eqn. 1.22).

$$\boldsymbol{NO} + CP(Cu^{2+}) \rightarrow CP(Cu^{+}\text{—}NO^{+}) \qquad \text{Eqn. 1.21}$$

$$CP(Cu^{+}—NO^{+}) + RSH \rightarrow CP(Cu^{+}) + RSNO + H^{+} \quad \text{Eqn. 1.22}$$

1.5.4 Lipid Peroxidation

NO has been shown to be an inhibitor of lipid peroxidation due to its nature as a free radical species.[110] NO combines with lipid radicals (lipidO·) formed during oxidative stress (Eqn. 1.23) to terminate the process of lipid peroxidation.

$$\boldsymbol{NO} + lipidO\cdot \rightarrow lipid - ONO \quad \text{Eqn. 1.23}$$

1.5.5 Nitric Oxide Reactions with Red Blood Cells

NO interacts with red blood cells (RBCs) through different mechanisms depending on the oxidation state and coordination number of the iron prosthetic group. Under aerobic conditions, NO rapidly reacts with the heme moiety of oxyhemoglobin ($Hb(Fe^{2+}—O_2)$) (Eqn. 1.24) in which both NO and heme are oxidized by molecular oxygen ($k = 3.7\times10^{7}\ M^{-1}s^{-1}$) to form methemoglobin and nitrate.[98] This reaction is the primary influence on the short half-life of NO in blood (<2 ms).[102,114]

$$\boldsymbol{NO} + Hb(Fe^{2+}—O_2) \rightarrow Hb(Fe^{3+}) + NO_3^{-} \quad \text{Eqn. 1.24}$$

Under hypoxic conditions, nitrosylation of deoxyhemoglobin ($Hb(Fe^{2+})$) occurs rapidly ($k_{forward} = 2.0\times10^{7}\ M^{-1}s^{-1}$, $k_{reverse} = 5.0\times10^{-5}\ M^{-1}s^{-1}$) (Fig. 1.10, Eqn. 1.25).[98,100]

$$\boldsymbol{NO} + Hb(Fe^{2+}) \rightleftharpoons Hb(Fe^{2+}—\boldsymbol{NO}) \quad \text{Eqn. 1.25}$$

The protein structure comprising hemoglobin is also known to form the RSNO *S*-nitrosohemoglobin (SNO-Hb).[35,115,116] The mechanism for this process has yet to be elucidated, but is thought to play a critical role in vascular function.

$$\boldsymbol{NO} + \cdot S—Hb \rightarrow SNO—Hb \quad \text{Eqn. 1.26}$$

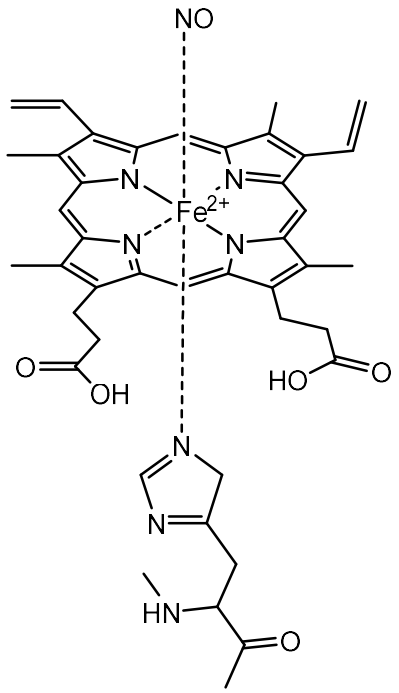

Figure 1.10. Nitric oxide bound to the heme moiety in hemoglobin.

1.6 Dissertation Overview

The research in this dissertation seeks to address biofouling associated with intravascular glucose biosensors using a novel NO-generating platform. Though considerable research has been conducted exploring NO-releasing scaffolds for enhanced blood compatibility, they are limited by the finite NO loading capacity of the material. We seek to incorporate the catalytic copper-based MOF CuBTTri into a medical grade polyurethane matrix for NO generation from endogenous NO sources for continuous NO release at the device surface. To accurately characterize and quantify the behavior of NO-generating materials, reliable and robust methods must be developed to prevent spontaneous RSNO decomposition under the desired experimental conditions. In Chapter 2, this research begins by evaluating the stability of two RSNOs, GSNO and SNAP, commonly used in the design NO-based biomaterials. In Chapter 3 and Chapter 4, the NO-generating performance of CuBTTri embedded within a polymer matrix was extensively

characterized and evaluated. The results of these experiments informed the selection of the optimal formulation to be implemented in an enzymatic glucose sensor in Chapter 5. And finally, in Chapter 6, we survey the effects of other metal ions to promote NO release to expand the range of potential catalysts for enhanced biocompatibility through NO generation. Ultimately, this dissertation provides valuable insights for the rational design of catalytic MOF composite biomaterials for enhanced blood compatibility using NO generation.

CHAPTER 1

REFERENCES

(1) Biological Evaluation of Medical Devices-Part 4: Selection of Tests for Interactions with Blood; 2017.

(2) Wolf, M. F.; Anderson, J. M. Practical Approach to Blood Compatibility Assessments: General Considerations and Standards. In Biocompatibility and Performance of Medical Devices; *Woodhead Publishing Series in Biomaterials*, **2020**; pp 167–205.

(3) Liu, X.; Yuan, L.; Li, D.; Tang, Z.; Wang, Y.; Chen, G.; Chen, H.; Brash, J. L. Blood Compatible Materials: State of the Art. *J. Mater. Chem. B* **2014**, *2*, 5718–5738.

(4) Hedayati, M.; Neufeld, M. J.; Reynolds, M. M.; Kipper, M. J. The Quest for Blood-Compatible Materials: Recent Advances and Future Technologies. *Mater. Sci. Eng. R Reports* **2019**, *138* (May), 118–152.

(5) Wolf, A. K.; Qin, Y.; Major, T. C.; Meyerhoff, M. E. Improved Thromboresistance and Analytical Performance of Intravascular Amperometric Glucose Sensors Using Optimized Nitric Oxide Release Coatings. *Chinese Chem. Lett.* **2015**, *26* (4), 464–468.

(6) Wang, J. Electrochemical Glucose Biosensors. *Chem. Rev.* **2008**, *108*, 814-825.

(7) Soto, R. J.; Hall, J. R.; Brown, M. D.; Taylor, J. B.; Schoenfisch, M. H. In Vivo Chemical Sensors: Role of Biocompatibility on Performance and Utility. *Anal. Chem.* **2017**, *89* (1), 276–299.

(8) Wang, H. C.; Lee, A. R. Recent Developments in Blood Glucose Sensors. *J. Food Drug Anal.* **2015**, *23* (2), 191–200.

(9) Chen, C.; Zhao, X.-L.; Li, Z.-H.; Zhu, Z.-G.; Qian, S.-H.; Flewitt, A. Current and

Emerging Technology for Continuous Glucose Monitoring. *Sensors* **2017**, *17* (1), 182.

(10) Schmelzeisen-Redeker, G.; Schoemaker, M.; Kirchsteiger, H.; Freckmann, G.; Heinemann, L.; Del Re, L. Time Delay of CGM Sensors: Relevance, Causes, and Countermeasures. *J. Diabetes Sci. Technol.* **2015**, *9* (5), 1006–1015.

(11) Xu, J.; Lee, H. Anti-Biofouling Strategies for Long-Term Continuous Use of Implantable Biosensors. *Chemosensors* **2020**, *8* (3), 1–29.

(12) Zhang, Y.; Hu, Y.; Wilson, G. S.; Moatti-Sirat, D.; Poitout, V.; Reach, G. Elimination of the Acetaminophen Interference in an Implantable Glucose Sensor. *Anal. Chem.* **1994**, *66* (7), 1183–1188.

(13) Bindra, D. S.; Zhang, Y.; Wilson, G. S.; Sternberg, R.; Thévenot, D. R.; Moatti, D.; Reach, G. Design and in Vitro Studies of a Needle-Type Glucose Sensor for Subcutaneous Monitoring. *Anal. Chem.* **1991**, *63* (17), 1692–1696.

(14) Ngoepe, M.; Choonara, Y. E.; Tyagi, C.; Tomar, L. K.; du Toit, L. C.; Kumar, P.; Ndesendo, V. M. K.; Pillay, V. Integration of Biosensors and Drug Delivery Technologies for Early Detection and Chronic Management of Illness. *Sensors (Switzerland)* **2013**, *13* (6), 7680–7713.

(15) Harding, J. L.; Reynolds, M. M. Combating Medical Device Fouling. *Trends Biotechnol.* **2014**, *32* (3), 140–146.

(16) Jaffer, I. H.; Fredenburgh, J. C.; Hirsh, J.; Weitz, J. I. Medical Device-Induced Thrombosis: What Causes It and How Can We Prevent It? *J. Thromb. Haemost.* **2015**, *13* (S1), S72–S81.

(17) Tsai, W. B.; Grunkemeier, J. M.; McFarland, C. D.; Horbett, T. A. Platelet Adhesion to Polystyrene-Based Surfaces Preadsorbed with Plasmas Selectively Depleted in

Fibrinogen, Fibronectin, Vitronectin, or von Willebrand's Factor. *J. Biomed. Mater. Res.* **2002**, *60* (3), 348–359.

(18) Vroman, L. The Importance of Surfaces in Contact Phase Reactions. *Semin. Thromb. Hemost.* **1987**, *13* (1).

(19) Turbill, P.; Beugeling, T.; Poot, A. A. Proteins Involved in the Vroman Effect during Exposure of Human Blood Plasma to Glass and Polyethylene. *Biomaterials* **1996**, *17*, 1279–1287.

(20) Plow, E. F.; Pierschbacher, M. D.; Ruoslahti, E.; Marguerie, G.; Ginsberg, M. H. Arginyl-Glycyl-Aspartic Acid Sequences and Fibrinogen Binding to Platelets. *Blood* **1987**, *70* (1), 110–115.

(21) Savage, B.; Ruggeri, Z. M. Selective Recognition of Adhesive Sites in Surface-Bound Fibrinogen by Glycoprotein IIb-IIIa on Nonactivated Platelets*. *J. Biol. Chem.* **1991**, *266* (17), 11227–11233.

(22) Fernández-Ruiz, I. In Search of Better Therapies to Prevent Device-Induced Thrombosis. *Nat. Milestones Anticoagul.* **2017**.

(23) Anticoagulation (Blood Thinners) and Congenital Heart Defects https://www.heart.org/en/health-topics/congenital-heart-defects/care-and-treatment-for-congenital-heart-defects/anticoagulation-and-congenital-heart-defects (accessed Apr 10, 2020).

(24) Chan, N. C.; Weitz, J. I. Antithrombotic Agents. *Circ. Res.* **2019**, *124* (3), 426–436.

(25) Mack, D.; Rohde, H.; Harris, L. G.; Davies, A. P.; Horstkotte, M. A.; Knobloch, J. K. M. Biofilm Formation in Medical Device-Related Infection. *Int. J. Artif. Organs* **2006**, *29* (4), 343–359.

(26) Costerton, J. W.; Stewart, P. S.; Greenberg, E. P. Bacterial Biofilms: A Common Cause of Persistent Infections. *Science* **1999**, *284* (5418), 1318–1322.

(27) Wallace, A.; Albadawi, H.; Patel, N.; Khademhosseini, A.; Zhang, Y. S.; Naidu, S.; Knuttinen, G.; Oklu, R. Anti-Fouling Strategies for Central Venous Catheters. *Cardiovasc. Diagn. Ther.* **2017**, *7*, S246–S257.

(28) Desrousseaux, C.; Sautou, V.; Descamps, S.; Traoré, O. Modification of the Surfaces of Medical Devices to Prevent Microbial Adhesion and Biofilm Formation. *J. Hosp. Infect.* **2013**, *85* (2), 87–93.

(29) Labarrere, C. A.; Dabiri, A. E.; Kassab, G. S. Thrombogenic and Inflammatory Reactions to Biomaterials in Medical Devices. *Front. Bioeng. Biotechnol.* **2020**, *8* (March), 1–18.

(30) Zander, Z. K.; Becker, M. L. Antimicrobial and Antifouling Strategies for Polymeric Medical Devices. *ACS Macro Lett.* **2018**, *7* (1), 16–25.

(31) Wilson, A. C.; Neuenschwander, P. F.; Chou, S. Engineering Approaches to Prevent Blood Clotting from Medical Implants. *Arch Biomed Eng Biotechnol.* **2019**, *1* (2), 1–9.

(32) Moncada, S.; Higgs, E. A. The Discovery of Nitric Oxide and Its Role in Vascular Biology. *Br. J. Pharmacol.* **2006**, *147*, S193–S201.

(33) Bogdan, C. Nitric Oxide and the Immune Response. *Nat. Immunol.* **2001**, *2* (10), 907–916.

(34) Guzik, T. J.; Korbut, R. NO and Superoxide in Inflammation and Immune Regulation. *J. Phys. Pharmacol.* **2003**, *54* (4) 469–487.

(35) Schulz, R.; Rassaf, T.; Massion, P. B.; Kelm, M.; Balligand, J.-L. Recent Advances in the Understanding of the Role of Nitric Oxide in Cardiovascular Homeostasis. *Pharmacol. Ther.* **2005**, *108* (3), 225–256.

(36) Gkaliagkousi, E.; Ritter, J.; Ferro, A. Platelet-Derived Nitric Oxide Signaling and Regulation. *Circ. Res.* **2007**, *101* (7), 654–662.

(37) Wink, D. A.; Mitchell, J. B. Chemical Biology of Nitric Oxide: Insights into Regulatory, Cytotoxic, and Cytoprotective Mechanisms of Nitric Oxide. *Free Radic. Biol. Med.* **1998**, *25* (4/5), 434–456.

(38) Bryan, N. S.; Ka, B.; Murad, F. Discovery of the Nitric Oxide Signaling Pathway and Targets for Drug Development. *Front. Biosci.* **2009**, *14*, 1–18.

(39) Loscalzo, J. The Identification of Nitric Oxide as Endothelium-Derived Relaxing Factor. *Circ. Res.* **2013**, *113* (2), 100–103.

(40) Broniowska, K. A.; Hogg, N. The Chemical Biology of S-Nitrosothiols. *Antioxid. Redox Signal.* **2012**, *17* (7), 969–980.

(41) Andrew, P. Enzymatic Function of Nitric Oxide Synthases. *Cardiovasc. Res.* **2002**, *43* (3), 521–531.

(42) Vaughn, M. W.; Kuo, L.; Liao, J. C. Estimation of Nitric Oxide Production and Reaction Rates in Tissue by Use of a Mathematical Model. *Am. J. Physiol.* **1998**, *274* (6), H2163–H2176.

(43) Wang, P. G.; Xian, M.; Tang, X.; Wu, X.; Wen, Z.; Cai, T.; Janczuk, A. J. Nitric Oxide Donors: Chemical Activities and Biological Applications. *Chem. Rev.* **2002**, *102* (4), 1091–1134.

(44) Williams, D. L. H. Nitric Oxide Releasing Compounds (NO Donors). *In Nitrosation Reactions and the Chemistry of Nitric Oxide*; **2004**; pp 199–220.

(45) Miller, M. R.; Megson, I. L. Recent Developments in Nitric Oxide Donor Drugs. *Br. J. Pharmacol.* **2007**, *151* (3), 305–321.

(46) Liang, H.; Nacharaju, P.; Friedman, A.; Friedman, J. M. Nitric Oxide Generating/Releasing Materials. *Futur. Sci OA* **2015**, *1* (1), 1–18.

(47) Hanson, S. R.; Hutsell, T. C.; Keefer, L. K.; Mooradian, D. L.; Smith, D. J. Nitric Oxide Donors: A Continuing Opportunity in Drug Design. *Adv. Pharmacol.* **1995**, *34*, 383–398.

(48) Gasco, A.; Fruttero, R.; Sorba, G.; Di Stilo, A.; Calvino, R. NO Donors: Focus on Furoxan Derivatives. *Pure Appl. Chem.* **2007**, *76* (5), 973–981.

(49) Riccio, D. A.; Schoenfisch, M. H. Nitric Oxide Release Part I. Macromolecular Scaffolds. *Chem. Soc. Rev.* **2012**, *41* (10), 3731–3741.

(50) Sun, J.; Murphy, E. Protein S-Nitrosylation and Cardioprotection. *Circ. Res.* **2010**, *106* (2), 285–296.

(51) Broniowska, K. A.; Diers, A. R.; Hogg, N. S-NITROSOGLUTATHIONE. *Biochim. Biophys. Acta* **2013**, *1830* (5), 3173–3181.

(52) Major, T. C.; Brant, D. O.; Burney, C. P.; Amoako, K. A.; Annich, G. M.; Meyerhoff, M. E.; Handa, H.; Bartlett, R. H. The Hemocompatibility of a Nitric Oxide Generating Polymer That Catalyzes S-Nitrosothiol Decomposition in an Extracorporeal Circulation Model. *Biomaterials* **2011**, *32* (26), 5957–5969.

(53) Major, T. C.; Handa, H.; Brisbois, E. J.; Reynolds, M. M.; Annich, G. M.; Meyerhoff, M. E.; Bartlett, R. H. The Mediation of Platelet Quiescence by NO-Releasing Polymers via CGMP-Induced Serine 239 Phosphorylation of Vasodilator-Stimulated Phosphoprotein. *Biomaterials* **2013**, *34* (33), 8086–8096.

(54) Hopkins, S. P.; Pant, J.; Goudie, M. J.; Schmiedt, C.; Handa, H. Achieving Long-Term Biocompatible Silicone via Covalently Immobilized S-Nitroso- N-Acetylpenicillamine (SNAP) That Exhibits 4 Months of Sustained Nitric Oxide Release. *ACS Appl. Mater.*

Interfaces **2018**, *10* (32), 27316–27325.

(55) Brisbois, E. J.; Handa, H.; Meyerhoff, M. E. Recent Advances in Hemocompatible Polymers for Biomedical Applications. *In Advanced Polymers in Medicine*; Springer International Publishing: Cham, **2015**; pp 481–511.

(56) Brisbois, E. J.; Handa, H.; Major, T. C.; Bartlett, R. H.; Meyerhoff, M. E. Long-Term Nitric Oxide Release and Elevated Temperature Stability with S-Nitroso-N-Acetylpenicillamine (SNAP)-Doped Elast-Eon E2As Polymer. *Biomaterials* **2013**, *34* (28), 6957–6966.

(57) Pant, J.; Goudie, M. J.; Hopkins, S. P.; Brisbois, E. J.; Handa, H. Tunable Nitric Oxide Release from S-Nitroso-N-Acetylpenicillamine via Catalytic Copper Nanoparticles for Biomedical Applications. *ACS Appl. Mater. Interfaces* **2017**, *9* (18), 15254–15264.

(58) Hogg, N. Biological Chemistry and Clinical Potential of S-Nitrosothiols. *Free Radic. Biol. Med.* **2000**, *28* (10), 1478–1486.

(59) Blanchard, B.; Servy, C.; Ducrocq, C. Chemical Evaluation of Compounds as Nitric Oxide or Peroxynitrite Donors Using the Reactions with Serotonin. *Free Radic. Res.* **2001**, *34* (2), 189–191.

(60) Singh, R. J.; Hogg, N.; Joseph, J.; Kalyanaraman, B. Mechanism of Nitric Oxide Release from S-Nitrosothiols*. *J. Biol. Chem.* **1996**, *271* (31), 18596–18603.

(61) Melvin, A. C.; Jones, W. M.; Lutzke, A.; Allison, C. L.; Reynolds, M. M. S-Nitrosoglutathione Exhibits Greater Stability than S-Nitroso-N-Acetylpenicillamine under Common Laboratory Conditions: A Comparative Stability Study. *Nitric Oxide* **2019**, *92*, 18–25.

(62) Reynolds, M. M.; Frost, M. C.; Meyerhoff, M. E. Nitric Oxide-Releasing Hydrophobic

Polymers: Preparation, Characterization, and Potential Biomedical Applications. *Free Radic. Biol. Med.* **2004**, *37* (7), 926–936.

(63) Seabra, A. B.; Duran, N. Nitric Oxide-Releasing Vehicles for Biomedical Applications. *J. Mater. Chem.* **2010**, *20* (1624–1637).

(64) Yang, T.; Zelikin, A. N.; Chandrawati, R. Progress and Promise of Nitric Oxide-Releasing Platforms. *Advanced Science* **2018**, *5*, 1701043.

(65) Fleming, G.; Aveyard, J.; Fothergill, J. L.; McBride, F.; Raval, R.; D'Sa, R. A. Nitric Oxide Releasing Polymeric Coatings for the Prevention of Biofilm Formation. *Polymers (Basel).* **2017**, *9*, 601.

(66) Yang, L.; Feura, E. S.; Ahonen, M. J. R.; Schoenfisch, M. H. Nitric Oxide–Releasing Macromolecular Scaffolds for Antibacterial Applications. *Adv. Healthc. Mater.* **2018**, *7* (13), 1–18.

(67) Wo, Y.; Brisbois, E. J.; Bartlett, R. H.; Meyerhoff, M. E. Recent Advances in Thromboresistant and Antimicrobial Polymers for Biomedical Applications: Just Say Yes to Nitric Oxide (NO). *Biomater. Sci.* **2016**, *4* (8), 1161–1183.

(68) Vlcek, J. R.; Hedayati, M.; Melvin, A. C.; Reynolds, M. M.; Kipper, M. J. Blood-Compatible Materials: Vascular Endothelium-Mimetic Surfaces That Mitigate Multiple Cell-Material Interactions. *Adv. Healthc. Mater.* **2021**, *2001748*, 20–25.

(69) Zhou, Z.; Meyerhoff, M. E. Polymethacrylate-Based Nitric Oxide Donors with Pendant N-Diazeniumdiolated Alkyldiamine Moieties: Synthesis, Characterization, and Preparation of Nitric Oxide Releasing Polymeric Coatings. *Biomacromolecules* **2005**, *6* (2), 780–789.

(70) Wo, Y.; Brisbois, E. J.; Wu, J.; Li, Z.; Major, T. C.; Mohammed, A.; Wang, X.; Colletta,

A.; Bull, J. L.; Matzger, A. J.; et al. Reduction of Thrombosis and Bacterial Infection via Controlled Nitric Oxide (NO) Release from S-Nitroso-N-Acetylpenicillamine (SNAP) Impregnated CarboSil Intravascular Catheters. ACS Biomater. Sci. Eng. 2017, 3 (3), 349–359.

(71) Roberts, T. R.; Neufeld, M. J.; Meledeo, M. A.; Cap, A. P.; Cancio, L. C.; Reynolds, M. M.; Batchinsky, A. I. A Metal Organic Framework Reduces Thrombus Formation and Platelet Aggregation Ex Vivo. *J. Trauma Acute Care Surg.* **2018**, *85* (3), 572–579.

(72) J. Neufeld, M.; Lutzke, A.; B. Tapia, J.; M. Reynolds, M. Metal–Organic Framework/Chitosan Hybrid Materials Promote Nitric Oxide Release from S-Nitrosoglutathione in Aqueous Solution. *ACS Appl. Mater. Interfaces* **2017**, *9* (6), 5139–5148.

(73) Harding, J. L.; Metz, J. M.; Reynolds, M. M. A Tunable, Stable, and Bioactive MOF Catalyst for Generating a Localized Therapeutic from Endogenous Sources. *Adv. Funct. Mater.* **2014**, *24* (47), 7503–7509.

(74) Tuttle, R. R.; Rubin, H. N.; Rithner, C. D.; Finke, R. G.; Reynolds, M. M. Copper Ion vs Copper Metal–Organic Framework Catalyzed NO Release from Bioavailable *S*-Nitrosoglutathione En Route to Biomedical Applications: Direct ^{1}H NMR Monitoring in Water Allowing Identification of the Distinct, True Reaction Stoichiometries and Thio. J. *Inorg. Biochem.* **2019**, *199* (July), 110760.

(75) Garren, M.; Maffe, P.; Melvin, A.; Griffin, L.; Wilson, S.; Douglass, M.; Reynolds, M.; Handa, H. Surface-Catalyzed Nitric Oxide Release via a Metal Organic Framework Enhances Antibacterial Surface Effects. *ACS Appl. Mater. Interfaces* **2021**, *13*, 56931–56943.

(76) Kang, Y. S.; Lu, Y.; Chen, K.; Zhao, Y.; Wang, P.; Sun, W. Y. Metal–Organic Frameworks with Catalytic Centers: From Synthesis to Catalytic Application. Coord. *Chem. Rev.* **2019**, *378*, 262–280.

(77) Bavykina, A.; Kolobov, N.; Khan, I. S.; Bau, J. A.; Ramirez, A.; Gascon, J. Metal-Organic Frameworks in Heterogeneous Catalysis: Recent Progress, New Trends, and Future Perspectives. *Chem. Rev.* **2020**, *120* (16), 8468–8535.

(78) Stock, N.; Biswas, S. Synthesis of Metal-Organic Frameworks (MOFs): Routes to Various MOF Topologies, Morphologies, and Composites. *Chem. Rev.* **2012**, *112* (2), 933–969.

(79) Wang, Z.; Liu, L.; Li, Z.; Goyal, N.; Du, T.; He, J.; Li, G. K. Shaping of Metal-Organic Frameworks: A Review. *Energy and Fuels* **2022**, *36*, 2927–2944.

(80) Ma, Q.; Zhang, T.; Wang, B. Shaping of Metal-Organic Frameworks, a Critical Step toward Industrial Applications. *Matter* **2022**, *5* (4), 1070–1091.

(81) Kalaj, M.; Bentz, K. C.; Ayala, S.; Palomba, J. M.; Barcus, K. S.; Katayama, Y.; Cohen, S. M. MOF-Polymer Hybrid Materials: From Simple Composites to Tailored Architectures. *Chem. Rev.* **2020**, *120* (16), 8267–8302.

(82) Kitao, T.; Zhang, Y.; Kitagawa, S.; Wang, B.; Uemura, T. Hybridization of MOFs and Polymers. *Chem. Soc. Rev.* **2017**, *46* (11), 3108–3133.

(83) Husna, A.; Hossain, I.; Jeong, I.; Kim, T.-H. Mixed Matrix Membranes for Efficient CO2 Separation Using an Engineered UiO-66 MOF in a Pebax Polymer. *Polymers (Basel).* **2022**, *14* (4), 655.

(84) Zhang, W.; Li, B.; Duan, W.; Yao, X.; Lu, X.; Li, S.; Tian, Y.; Li, D. Confined: In Situ Polymerization in a Nanoscale Porphyrinic Metal-Organic Framework for Fluorescence

Imaging-Guided Synergistic Phototherapy. *Inorg. Chem. Front.* **2022**, *9* (4), 670–677.

(85) Kobayashi, Y.; Honjo, K.; Kitagawa, S.; Uemura, T. Preparation of Porous Polysaccharides Templated by Coordination Polymer with Three-Dimensional Nanochannels. *ACS Appl. Mater. Interfaces* **2017**, *9* (13), 11373–11379.

(86) Zahir, M. H.; Helal, A.; Hakeem, A. S. Hybrid PolyMOF Materials Prepared by Combining an Organic Polymer with a MOF and Their Application for Solar Thermal Energy Storage. *Energy and Fuels* **2021**, *35* (12), 10199–10209.

(87) Jiang, Y.; Sun, J.; Yang, X.; Shen, J.; Fu, Y.; Fan, Y.; Xu, J.; Wang, L. Cd-MOF@PVDF Mixed-Matrix Membrane with Good Catalytic Activity and Recyclability for the Production of Benzimidazole and Amino Acid Derivatives. *Inorg. Chem.* **2021**, *60* (3), 2087–2096.

(88) Gao, K.; Guo, X.; Zheng, B.; Wang, J.; Wang, L. Investigation of Interface Compatibility in Stiff Polymer/Metal–Organic Frameworks. Mater. Today Chem. 2021, 20, 100458.

(89) Palomba, J. M.; Wirth, D. M.; Kim, J. Y.; Kalaj, M.; Clarke, E. M.; Peterson, G. W.; Pokorski, J. K.; Cohen, S. M. Strong, Ductile MOF-Poly(Urethane Urea) Composites. *Chem. Mater.* **2021**, *33* (9), 3164–3171.

(90) Denny, M. S.; Kalaj, M.; Bentz, K. C.; Cohen, S. M. Multicomponent Metal-Organic Framework Membranes for Advanced Functional Composites. *Chem. Sci.* **2018**, *9* (47), 8842–8849.

(91) Sorribas, S.; Kudasheva, A.; Almendro, E.; Zornoza, B.; de la Iglesia, Ó.; Téllez, C.; Coronas, J. Pervaporation and Membrane Reactor Performance of Polyimide Based Mixed Matrix Membranes Containing MOF HKUST-1. *Chem. Eng. Sci.* **2015**, *124*, 37–44.

(92) McCarthy, D. L.; Liu, J.; Dwyer, D. B.; Troiano, J. L.; Boyer, S. M.; Decoste, J. B.; Bernier, W. E.; Jones, W. E. Electrospun Metal-Organic Framework Polymer Composites for the Catalytic Degradation of Methyl Paraoxon. *New J. Chem.* **2017**, *41* (17), 8748–8753.

(93) Hetrick, E. M.; Schoenfisch, M. H. Analytical Chemistry of Nitric Oxide. *Annu Rev Anal Chem* **2009**, *2*, 409–433.

(94) Coneski, P. N.; Schoenfisch, M. H. Nitric Oxide Release: Part III. Measurement and Reporting. *Chem. Soc. Rev.* **2012**, *41* (10), 3753–3758.

(95) Sangster, J. Kinetics of the Chemiluminescent Reaction Between Ozone and Nitric Oxide. *Transactions of the Faraday Society* **1964**, *60*, 359-370.

(96) Gudem, M.; Hazra, A. Mechanism of the Chemiluminescent Reaction between Nitric Oxide and Ozone. *J. Phys. Chem. A* **2019**, *123* (4), 715–722.

(97) Sievers Nitric Oxide Analyzer NOA 280i: Operation and Maintenance Manual; Boulder, CO, **2010**.

(98) Toledo, J. C.; Augusto, O. Connecting the Chemical and Biological Properties of Nitric Oxide. *Chem. Res. Toxicol.* **2012**, *25* (5), 975–989.

(99) Kapil, V.; Khambata, R. S.; Jones, D. A.; Rathod, K.; Primus, C.; Massimo, G.; Fukuto, J. M.; Ahluwalia, A. The Noncanonical Pathway for in Vivo Nitric Oxide Generation: The Nitrate-Nitrite-Nitric Oxide Pathway. *Pharmacol. Rev.* **2020**, *72* (3), 692–766.

(100) Vinogradov, S. N.; Moens, L. Diversity of Globin Function: Enzymatic, Transport, Storage, and Sensing. *J. Biol. Chem.* **2008**, *283* (14), 8773–8777.

(101) Yu, B.; Ichinose, F.; Bloch, D. B.; Zapol, W. M. Inhaled Nitric Oxide. *Br. J. Pharmacol.* **2019**, *176* (2), 246–255.

(102) Liu, X.; Miller, M. J. S.; Joshi, M. S.; Sadowska-Krowicka, H.; Clark, D. A.; Lancaster, J. R. Diffusion-Limited Reaction of Nitric Oxide with Erythrocytes vs Free Hemoglobin. *J. Biol. Chem.* **1998**, *273* (30), 18709–18713.

(103) Zhang, G.; Xiang, B.; Dong, A.; Skoda, R. C.; Daugherty, A.; Smyth, S. S.; Du, X.; Li, Z. Biphasic Roles for Soluble Guanylyl Cyclase (SGC) in Platelet Activation. *Blood* **2011**, *118* (13), 3670–3679.

(104) Denninger, J. W.; Marletta, M. A. Guanylate Cyclase and the .NO/CGMP Signaling Pathway. *Biochim. Biophys. Acta* **1999**, *1411*, 334–350.

(105) Radomski, M. W.; Palmer, R. M. J.; Moncada, S. The Role of Nitric Oxide and CGMP in Platelet Adhesion to Vascular Endothelium. Biochem. *Biophys. Res. Commun.* **1987**, *148* (3), 1482–1489.

(106) Wang, G. R.; Zhu, Y.; Halushka, P. V; Lincoln, T. M.; Mendelsohn, M. E. Mechanism of Platelet Inhibition by Nitric Oxide: In Vivo Phosphorylation of Thromboxane Receptor by Cyclic GMP-Dependent Protein Kinase. *Proc. Natl. Acad. Sci. U. S. A.* **1998**, *95* (9), 4888–4893.

(107) Heinrich, T. A.; Da Silva, R. S.; Miranda, K. M.; Switzer, C. H.; Wink, D. A.; Fukuto, J. M. Biological Nitric Oxide Signalling: Chemistry and Terminology. *Br. J. Pharmacol.* **2013**, *169* (7), 1417–1429.

(108) Cooper, C. E. Nitric Oxide and Iron Proteins. *Biochim. Biophys. Acta* **1999**, *1411* (2–3), 290–309.

(109) Beckman, J. S.; Koppenol, W. H. Nitric Oxide, Superoxide, and Peroxynitrite: The Good, the Bad, and the Ugly. *Am. J. Physiol. - Cell Physiol.* **1996**, *73*, C1424-C1437.

(110) Bianco, C. L.; Toscano, J. P.; Fukuto, J. M. An Integrated View of the Chemical Biology

of NO, CO, H_2S, and O_2. *In Nitric Oxide: Biology and Pathobiology*; Elsevier Inc., **2017**; pp 9–21.

(111) Kharitonov, V. G.; Sundquist, A. R.; Sharma, V. S. Kinetics of Nitric Oxide Autoxidation in Aqueous Solution. *J. Biol. Chem.* **1994**, *269* (8), 5881–5883.

(112) Wang, J.; Mei, F.; Bai, L.; Zhou, S.; Liu, D.; Yao, L.; Ahluwalia, A.; Ghiladi, R. A.; Su, L.; Shu, T.; et al. Serum Nitrite and Nitrate: A Potential Biomarker for Post-Covid-19 Complications? *Free Radic. Biol. Med.* **2021**, *175* (June), 216–225.

(113) Nagababu, E.; Rifkind, J. M. Routes for Formation of S-Nitrosothiols in Blood. *Cell Biochem Biophys* **2013**, *67* (2), 385–398.

(114) Thomas, D. D.; Liu, X.; Kantrow, S. P.; Lancaster, J. R. The Biological Lifetime of Nitric Oxide: Implications for the Perivascular Dynamics of NO and O_2. *Proc. Natl. Acad. Sci.* **2012**, *98* (1), 355–360.

(115) Helms, C. C.; Gladwin, M. T.; Kim-Shapiro, D. B. Erythrocytes and Vascular Function: Oxygen and Nitric Oxide. *Front. Physiol.* **2018**, *9* (FEB), 1–9.

(116) Manukhina, E. B.; Downey, H. F.; Mallet, R. T. Role of Nitric Oxide in Cardiovascular Adaptation to Intermittent Hypoxia. *Exp. Biol. Med.* **2006**, *231* (4), 343–365.

CHAPTER 2

COMPARATIVE STABILITY OF TWO COMMON *S*-NITROSOTHIOLS FOR ROBUST ANALYTICAL METHOD DEVELOPMENT OF NITRIC OXIDE-GENERATING SYSTEMS[1]

2.1 Overview

S-Nitrosothiols (RSNOs) are a bioavailable source of nitric oxide (NO). A new generation of thromboresistant medical device materials are being designed to generate NO from endogenous RSNOs at the blood-device interface to prevent thrombus formation. *S*-nitrosoglutathione (GSNO) and *S*-nitroso-*N*-acetylpenicillamine (SNAP) are commonly used as a proxy for endogenous RSNO concentrations in the development of new NO-generating materials. It is known that RSNOs are susceptible to decomposition by stimuli including heat, light, and trace metal ions which can inadvertently be introduced through basic handling, storage, and experimental setups. Despite their frequent use, there is limited and conflicting literature examining the comparative stability of GSNO and SNAP. In order to accurately characterize and quantify the behavior of NO-generating materials, reliable and robust methods must be developed to prevent spontaneous RSNO decomposition under the desired experimental conditions.

2.2 Introduction

S-Nitrosothiols (RSNOs) represent attractive substrates for the controlled delivery of nitric oxide (NO), a radical species that participates in a variety of physiological processes such

[1] This chapter was reproduced in part from:
Melvin, A. C.; Jones, W. M.; Lutzke, A.; Allison, C. L.; Reynolds, M. M. *S*-Nitrosoglutathione Exhibits Greater Stability than *S*-Nitroso-N-Acetylpenicillamine under Common Laboratory Conditions: A Comparative Stability Study. *Nitric Oxide* **2019**, *92*, 18–25. Copyright 2019 Elsevier Inc. https://doi.org/10.1016/j.niox.2019.08.002.

as vasodilation, immune response, and cell signaling.[1] In the development of antithrombotic biomaterials, RSNOs serve as NO donors in polymer formulations used to fabricate blood-compatible biomedical devices.[2-8] Other applications use RSNOs as a convenient NO source in biological research, where the cytotoxic properties of NO can be exploited for antimicrobial effects, treatment of cancer, or as a method of eliciting unique biochemical responses.[9-11] NO release from RSNOs can be triggered through physical and chemical stimuli including heat, visible and ultraviolet light, and exposure to transition metal ions (most notably copper).[12-14] During handling, preparation, and usage, RSNOs can be exposed to stimuli that initiate their decomposition.[15] As a consequence of this instability, appropriate precautions are necessary to limit premature RSNO decomposition. This consideration is particularly critical in sensitive biological applications, where reliable delivery of NO from RSNO substrates may not be achievable without careful control of environmental factors.

Two commonly used RSNOs are *S*-nitrosoglutathione (GSNO), a bioavailable primary RSNO in mammalian blood, and *S*-nitroso-*N*-acetylpenicillamine (SNAP), a synthetic tertiary RSNO derived from the amino acid penicillamine (Fig. 2.1a and b).[2-8,16-18] These RSNOs are reported to exhibit sufficient stability as solids to permit handling and storage for prolonged periods of time.[14] It has been proposed that NO release from RSNOs occurs through homolytic cleavage of the S-N bond to form NO and thiyl radicals, and the latter product may dimerize to form the corresponding disulfide (Fig. 2.1c). Homolytic S-N bond dissociation energies are estimated to fall within the range of 20-32 kcal mol^{-1}, which encompasses half-lives of minutes to years.[15,19,20]

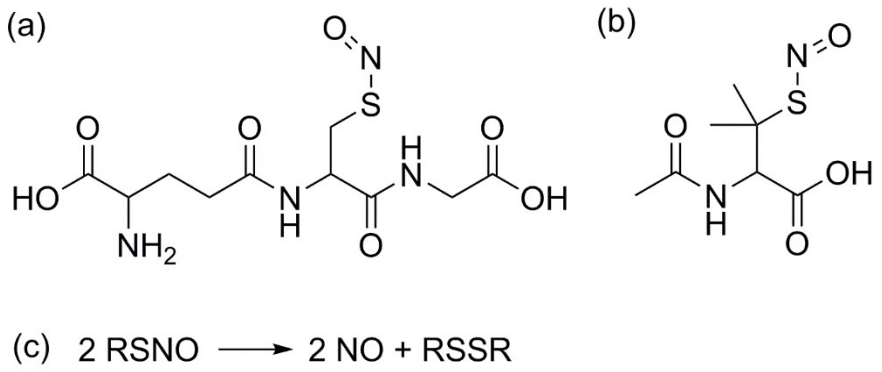

Figure 2.1. (a) *S*-Nitrosoglutathione (GSNO), (b) *S*-nitroso-*N*-acetyl-penicillamine (SNAP), (c) *S*-nitrosothiol (RSNO) decomposition.

Despite their frequent use as NO donors, there is limited and conflicting literature examining the comparative stability of GSNO and SNAP. Existing literature indicates that tertiary RSNOs are more stable than their primary counterparts.[21-24] There is also literature to suggest that GSNO is an exception to this trend.[2] However, other research has shown that both RSNOs thermally lyse NO near 150 °C, indicating that the strength of the S-N bonds are equivalent despite substitution differences.[25]

Herein, we investigated these discrepancies using stepwise isothermal thermogravimetric analysis (TGA). The decomposition products obtained from TGA experiments were characterized by mass spectrometry (MS), nuclear magnetic resonance (NMR), and attenuated total reflectance Fourier transform infrared spectroscopy (ATR-FTIR). Furthermore, the solution stability of GSNO and SNAP was investigated as a function of temperature, pH, and light exposure in the presence of a metal ion chelator using ultraviolet-visible spectroscopy (UV-Vis), with the goal of establishing proper handling, preparation, and usage techniques.

2.3 Materials and Methods

2.3.1 Materials

The following chemicals and reagents were used as received: acetone (99.5%, Sigma-Aldrich), *N*-acetyl-D-penicillamine (NAP; 99.0%, Sigma-Aldrich), citric acid monohydrate (ACS certified, Fisher), deuterium oxide (99.9% D, Cambridge Isotopes Laboratories), dinitrogen (ultra-high purity, Airgas), ethylenediaminetetraacetic acid disodium salt dihydrate (EDTA; 99.0%, Sigma-Aldrich), L-glutathione, oxidized (GSSG; 98%, Sigma-Aldrich), glutathione, reduced (GSH; 98%, AMRESCO), helium (ultra-high purity, Airgas), hydrochloric acid (35.0–38.0 wt. %, Fisher), magnesium sulfate (98.0%, EMD), methanol (99.9%, Fisher), methanol-d_4 (99.8% D, Cambridge Isotope Laboratories), nitric acid (68.0–70.0 wt. %, EMD), phosphate-buffered saline (PBS) tablets (Biotechnology grade, AMRESCO), sodium hydroxide (98.9%, Fisher), sodium nitrite (97.0%, EMD; 99.999%, Alfa-Aesar), sodium phosphate dibasic (anhydrous, 99.0%, Sigma-Aldrich), and sulfuric acid (95.0-98.0 wt. %, BDH/VWR International). Water (18.2 MΩ·cm) was prepared using a Millipore Direct-Q water purification system (EMD Millipore).

2.3.2 S-*Nitroso*-N-*acetyl-penicillamine (SNAP) Synthesis*

In a typical reaction, *S*-nitroso-*N*-acetyl-penicillamine (SNAP) was prepared following an adapted protocol of the method reported by Field et. al.[26] A solution of methanol (10 mL) and 1 M hydrochloric acid (10 mL) was prepared and cooled to 0 °C using an ice-water bath. Concentrated sulfuric acid (1 mL) was added to the solution. *N*-Acetyl-D-penicillamine (NAP; 0.956 g, 5.0 mmol) was added to the solution while stirring, resulting in a NAP suspension. Separately, sodium nitrite (0.690 g, 10.0 mmol) was dissolved in ultrapure water (5 mL), and this solution was sequentially added in small portions to the NAP suspension, resulting in vigorous bubbling and development of a green color for the mixture. The reaction was immediately shielded from light and stirred for 40 minutes at room temperature. The resulting mixture was

filtered to isolate a green precipitate, which was subsequently washed with 4 × 10 mL of 0-5 °C ultrapure water. The product was placed under dynamic vacuum (<100 mTorr) for 4 h to remove residual solvent, affording 0.594 g of SNAP (54% yield, 97% pure). The product was stored in a light-free, −20 °C freezer when not in use. ^{1}H NMR (400 MHz, CD_3OD): 5.32 (m, 1H), 2.04 (s, 3H), 2.01 (s, 3H), 1.97 ppm (s, 3H).[27] ^{13}C NMR (101 MHz, D_2O): 174.70, 173.47, 61.49, 57,77, 26.65, 25.17, 22.26 ppm. UV-Vis (H_2O): 339 nm ($\pi \rightarrow \pi^*$), 591 ($n_N \rightarrow \pi^*$).[13]

2.3.3 S-*Nitrosoglutathione (GSNO) Synthesis*

In a typical reaction, *S*-nitrosoglutathione (GSNO) was prepared following an adapted protocol of the method reported by Hart.[28] Reduced glutathione (1.54 g, 5.0 mmol) was suspended in ultrapure water (8 mL) and dissolved with the addition of 2 M hydrochloric acid (2.5 mL). The reaction was cooled to 0 °C using an ice-water bath, and sodium nitrite (0.345 g, 5.0 mmol) was added. The reaction was immediately shielded from light and stirred for 40 minutes at 0 °C. The resulting mixture was filtered to isolate a reddish-pink precipitate, which was subsequently washed with 5 × 5 mL of 0-5 °C ultrapure water and 3 × 5 mL of acetone. The product was placed under dynamic vacuum (<100 mTorr) for 4 h to remove residual solvent, affording 0.865 g of GSNO (51% yield, 98% pure). The obtained product was stored in a light-free, −20 °C freezer when not in use. ^{1}H NMR (400 MHz, D_2O): 4.70-4.61 (m, 1H), 4.20-3.90 (m, 2H), 3.93 (s, 2H), 3.78 (t, 1H, J = 6.4 Hz), 2.42 (t, 2H, J = 7.6 Hz), 2.18-2.01 (m, 2H).[29] ^{13}C NMR (101 MHz, D_2O): 175.27, 174.04, 174.01, 172.42, 54.28, 53.14, 42.08, 34.03, 31.69, 26.49 ppm. UV-Vis (H_2O): 335 nm ($\pi \rightarrow \pi^*$), 545 nm ($n_N \rightarrow \pi^*$).[28]

2.3.4 Sample Handling

Experimental techniques and sample handling were performed on the benchtop or on a dual-manifold Schlenk line using N_2 in the inert gas manifold.

2.3.5 Thermal Analyses

Stepwise isothermal thermogravimetric analyses (TGA) were performed using a TA Instruments TGA Q500 instrument equipped with a standard ceramic furnace. Stepwise isothermal thermogravimetric analyses with coupled mass spectrometry (TGA-MS) were performed using a TA Instruments TGA Q500 instrument equipped with an Evolved Gas Analysis (EGA) quartz-lined furnace coupled to a Discovery Mass Spectrometer. For the standard ceramic furnace, ultra-high purity (UHP) N_2 was used as the purge gas at a flow rate of 40 mL min^{-1} for the balance purge and 60 mL min^{-1} for the furnace purge. For the EGA furnace, ultra-high purity (UHP) helium was used as the purge gas at a flow rate of 10 mL·min^{-1} for the balance purge and 90 mL·min^{-1} for the furnace purge. Samples (~ 5-10 mg) were contained in platinum sample pans. Step-wise isothermal heating was programmed as follows: ramp 10 °C min^{-1} to 100 °C, stepwise isothermal ramp at 2 °C min^{-1} to 145 °C with isotherm entry-exit values of % wt. change/min at 0.4% min^{-1}, isothermal 1000 min until entry-exit condition met or 145 °C reached, return to stepwise isothermal ramp conditions.

2.3.6 Nuclear Magnetic Resonance (NMR) Analyses

NMR spectroscopy was performed using a Bruker AVANCE NEO 400 spectrometer to observe ^{1}H and ^{13}C nuclei. In ^{1}H NMR experiments, samples were dissolved in deuterium oxide (D_2O) or methanol-d_4 and spectra were acquired at 400 MHz from 32 transients at 25 °C. Chemical shifts were referenced to the solvent peak (HDO; 4.790 ppm). In ^{13}C NMR experiments, samples were dissolved in D_2O and spectra were acquired at 101 MHz from 512 transients at 25 °C. Methanol (49.50 ppm) was added to the D_2O as an internal reference at a concentration of 1 μL mL^{-1}.

2.3.7 Attenuated Total Reflectance Fourier Transform Infrared Spectroscopy (ATR-FTIR) Analyses

ATR-FTIR was performed using a Nicolet iS50 FTIR spectrometer equipped with an ATR sampling accessory with a diamond crystal. Representative spectra are shown for ATR-FTIR data.

2.3.8 Solution Stability Studies

Glassware was cleaned using aqua regia and ultrapure water. All RSNO solutions (20 mL) were prepared at 1.5×10^{-3} M with 100 μM EDTA under aerobic conditions and shielded from light in 20 mL amber scintillation vials. Temperatures sampled were 5 °C, 22 °C, and 37 °C in 10 mM PBS (pH 7.4). Solutions of 0.12 M pH 3.0 and 0.15 M 5.0 were prepared in citric acid-sodium phosphate dibasic buffer. Solution stability under fluorescent light exposure was performed in a fume hood with a light-to-benchtop distance of 122 cm. The intensity of the fume hood light was reported at 861 lux (2.4 m candles) by the manufacturer (Bedcolab).

2.3.9 Ultraviolet-Visible Spectroscopy (UV-Vis) Analyses

RSNO decomposition was measured by UV-Vis spectroscopy in 1.0 cm quartz cuvettes using a Nicolet Evolution 300 UV-Vis spectrophotometer.

2.3.10 Light Spectra Analysis

Laboratory light spectra were acquired using an Ocean Optics STS-UV microspectrometer with a 400 μm QP400-2-SR optical fiber.

2.3.11 Mass Spectrometry (MS) Analyses

Mass spectra were obtained using an Agilent 6224 time-of-flight mass spectrometer (TOF-MS) equipped with a dual electrospray ionization source operated in negative ion mode using a 100% methanol mobile phase.

2.3.12 Data Reporting and Analysis

All data were reported as a mean ± standard deviation of n ≥ 3 replicate measurements. Statistical difference was determined using two-tailed Student's t-test (p <0.01). Thermal decomposition temperatures were determined using the Onset Point analysis function with the TRIOS (v. 4.2.1.36612, TA Instruments) software platform. Percent RSNO remaining in solution was determined by monitoring the decomposition via decreasing absorption at λ_{max} (GSNO, 335 nm; SNAP, 339 nm). The absorption at time t (A_t) was compared to the initial absorbance at t_0 (A_{t0}) by the equation: $(A_t/A_{t0})\cdot 100\%$.

2.4 Results and Discussion

2.4.1 Thermal Stability of Solid GSNO and SNAP

RSNOs possess modest thermal stability with bond dissociation energies reported in the range of 20-32 kcal mol^{-1}.[19,20] Thermal scission of the S-N bond is believed to proceed through homolytic dissociation, resulting in the formation of NO and the corresponding thiyl radical (Fig. 2.1c).[13] We examined the thermal stability of solid GSNO and SNAP using stepwise isothermal TGA to determine the temperature at which NO is released (Fig. 2.2). Our results indicate that GSNO and SNAP decompose at 134.7 ± 0.8 °C and 132.8 ± 0.9 °C, respectively. These decomposition temperatures are substantially lower than previously published values obtained by thermal methods. For example, Bainbrigge et al. reported that both GSNO and SNAP decompose at 148 °C, while Parent et al. found that the NO-forming decomposition of GSNO occurs at 150.3 °C.[25,29] We observed that routine variation in purity and age of RSNO samples is insufficient to account for this 15 °C difference in decomposition temperature. For example, we found that low-purity (81%) GSNO decomposed at 138.0 ± 0.1 °C, overestimating the decomposition temperature by approximately 3 °C. The discrepancy in the temperature may be

due to the rapid heating of the sample (e.g., >10 °C min^{-1} in common furnace configurations) during TGA resulting in substantial overestimation of temperatures at which thermal phenomena are resolved.[30] We hypothesize that this overestimation is minimized by our heating rate of 2 °C min^{-1}, and that the actual thermal decomposition temperatures of GSNO and SNAP are lower than previously reported.[25,29] Thermal decomposition of GSNO (336.32 g mol^{-1}; $C_{10}H_{16}N_4O_7S$) resulted in a weight decrease of 9.3 ± 0.1%, which is largely consistent with the theoretical 8.9% reduction in mass expected from stoichiometric loss of NO. Thermogravimetric analysis coupled with mass spectrometry (TGA-MS) was used to evaluate the gaseous products evolved during the thermal decomposition of GSNO. At 134 °C, species of 30 *m*/*z* were rapidly released, consistent with the production of NO (Fig. 2.3). GSNO TGA experiments were halted at 145 °C and cooled to ambient temperature inside the furnace (UHP N_2, light-free) for further analysis by ATR-FTIR and ^{1}H NMR. Over the course of the thermal experiments, GSNO transitioned from a light pink powder to an off-white powder that remained soluble in water. The ATR-FTIR spectra (Fig. 2.4) show the disappearance of the diagnostic NO band at 1477 cm^{-1} (N=O stretching mode), supporting the absence of the RSNO functional group in the organic decomposition product.[13] Analysis by ^{1}H NMR reveals that the decomposition product is clearly distinct from GSNO and is consistent with commercial GSSG (Fig. 2.5). These findings, in addition to the TGA data, support that thermal decomposition of GSNO yields GSSG and NO stoichiometrically according to the scheme depicted in Fig. 2.1c.[25]

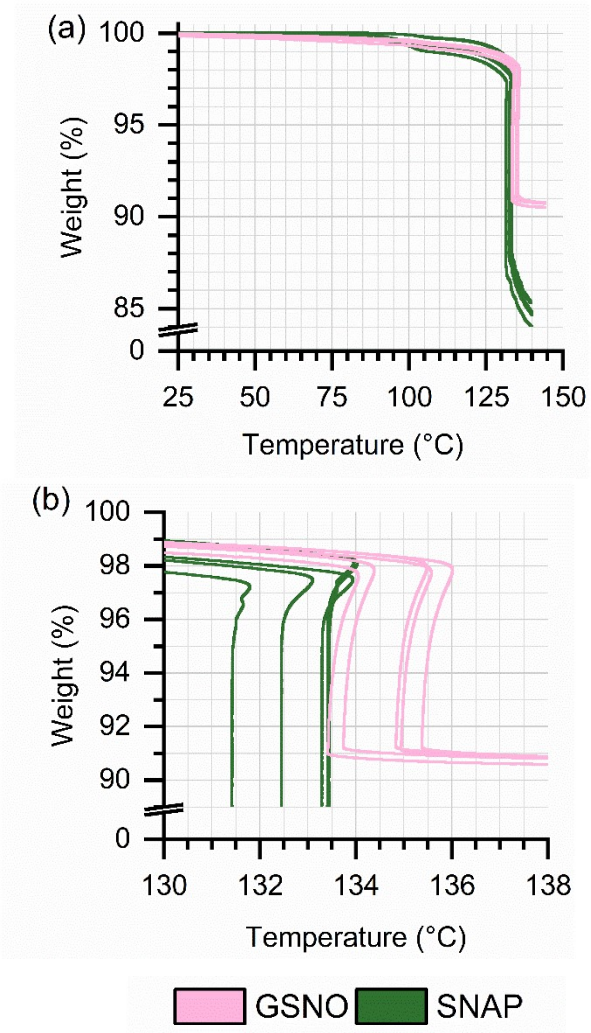

Figure 2.2. Stepwise-isothermal thermogravimetric analyses of GSNO (pink) and SNAP (green). GSNO and SNAP thermally decompose to release NO at 134.7 ± 0.8 °C and 132.8 ± 0.9 °C, respectively. Data reported as mean ± SD of n = 5 replicate measurements.

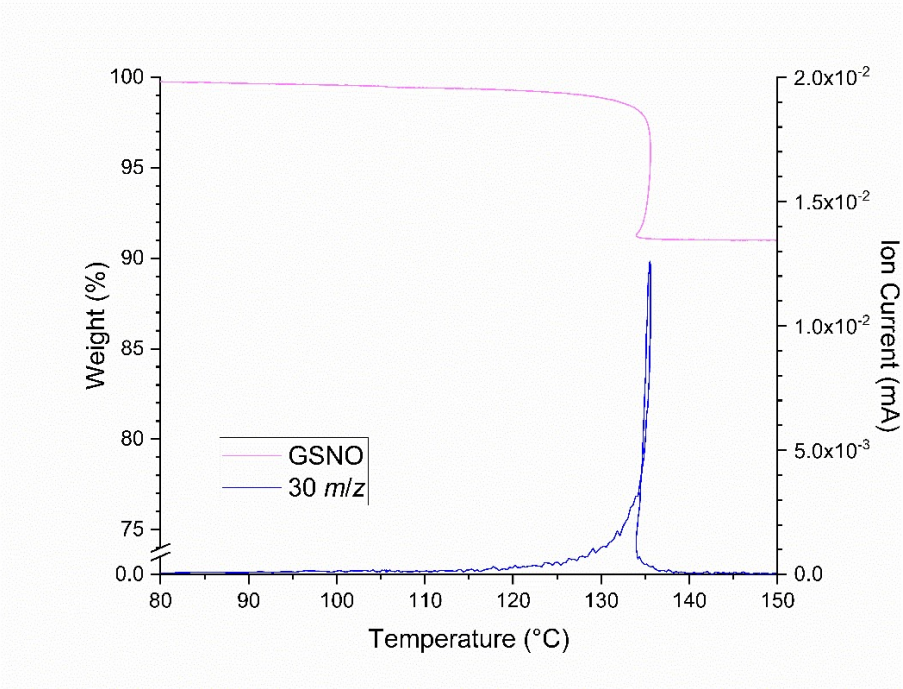

Figure 2.3. Representative thermogravimetric analysis coupled with mass spectrometry (TGA-MS) of GSNO (pink). The thermal transition observed at 134 °C is consistent with a 30 *m*/*z* molecular fragment detected by MS (blue), indicating thermal decomposition of the GSNO isothermally yields gaseous NO.

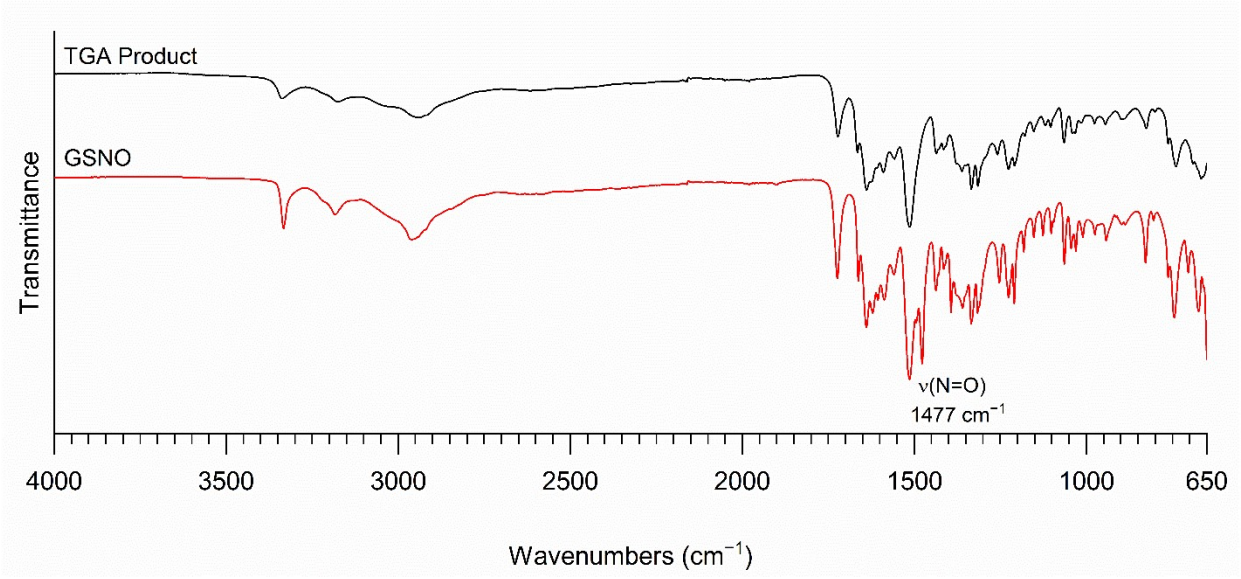

Figure 2.4. ATR-FTIR spectra of GSNO before (red) and after thermal analysis (black).

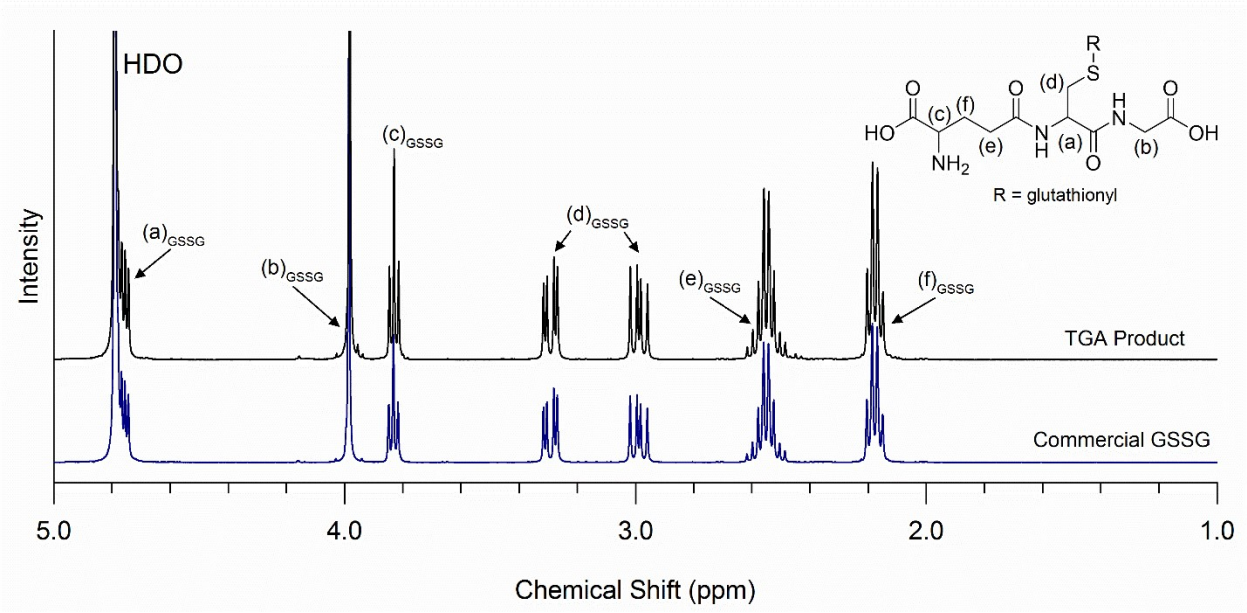

Figure 2.5. ^{1}H NMR spectra comparing GSNO TGA product to commercial GSSG. Spectrum acquired in D_2O at 25 °C.

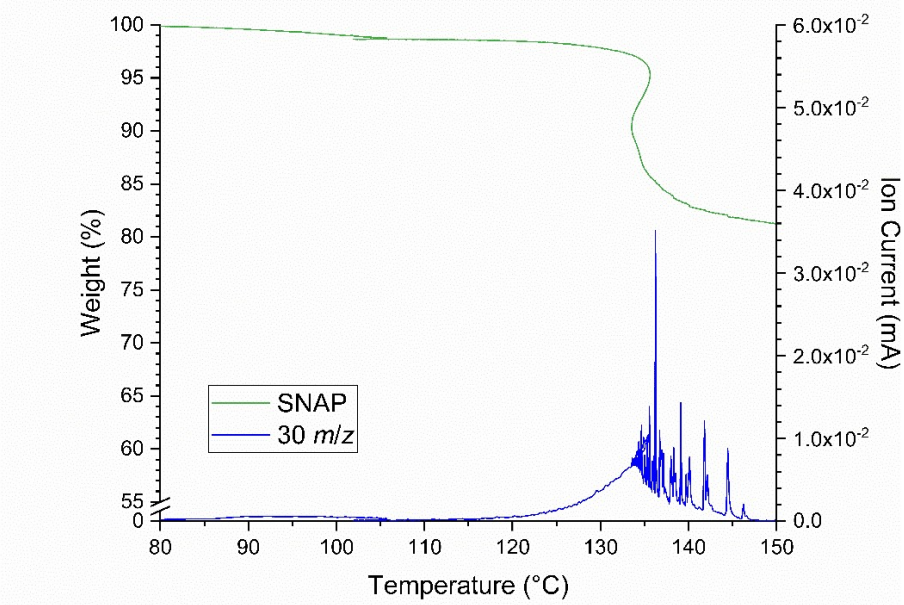

Figure 2.6. Representative thermogravimetric analysis coupled with mass spectrometry (TGA-MS) of SNAP (green). The thermal transition observed at 132 °C is consistent with a 30 *m*/*z* molecular fragment detected by MS (blue), indicating thermal decomposition of the SNAP yields gaseous NO over an extended temperature range.

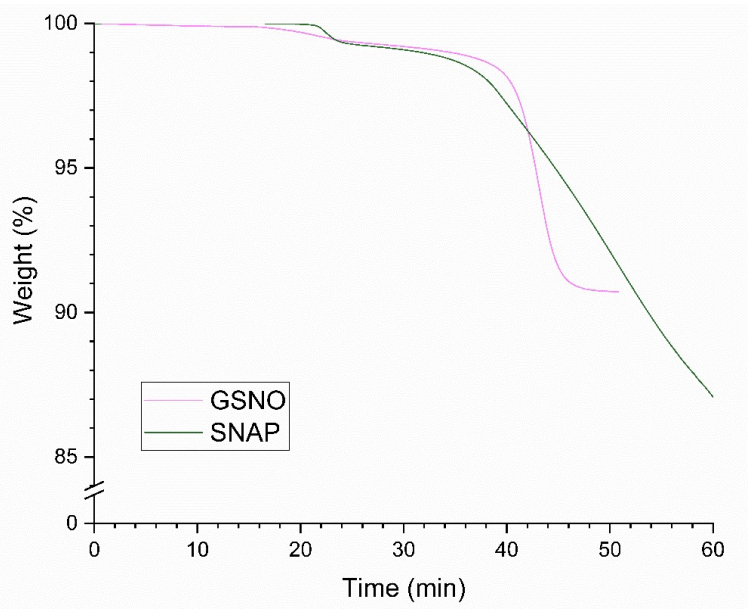

Figure 2.7. Time resolution of the thermogravimetric analyses. GSNO exhibits rapid mass loss at its thermal decomposition temperature and subsequently plateaus, while SNAP continuously loses mass until the experiment is terminated.

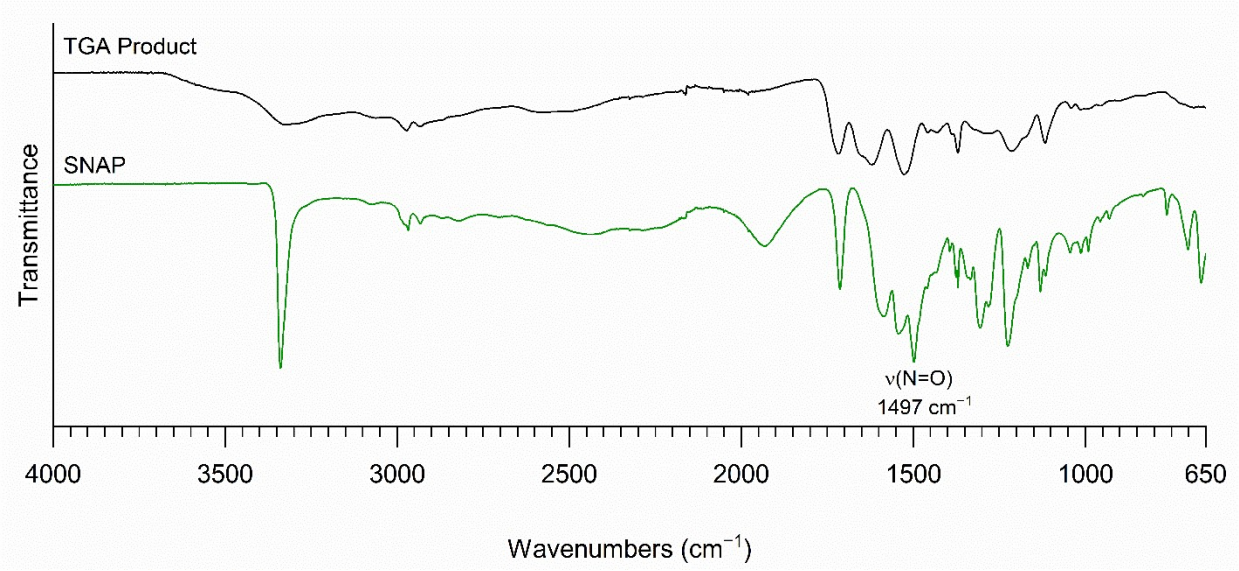

Figure 2.8. ATR-FTIR spectra of SNAP before (green) and after thermal analysis (black).

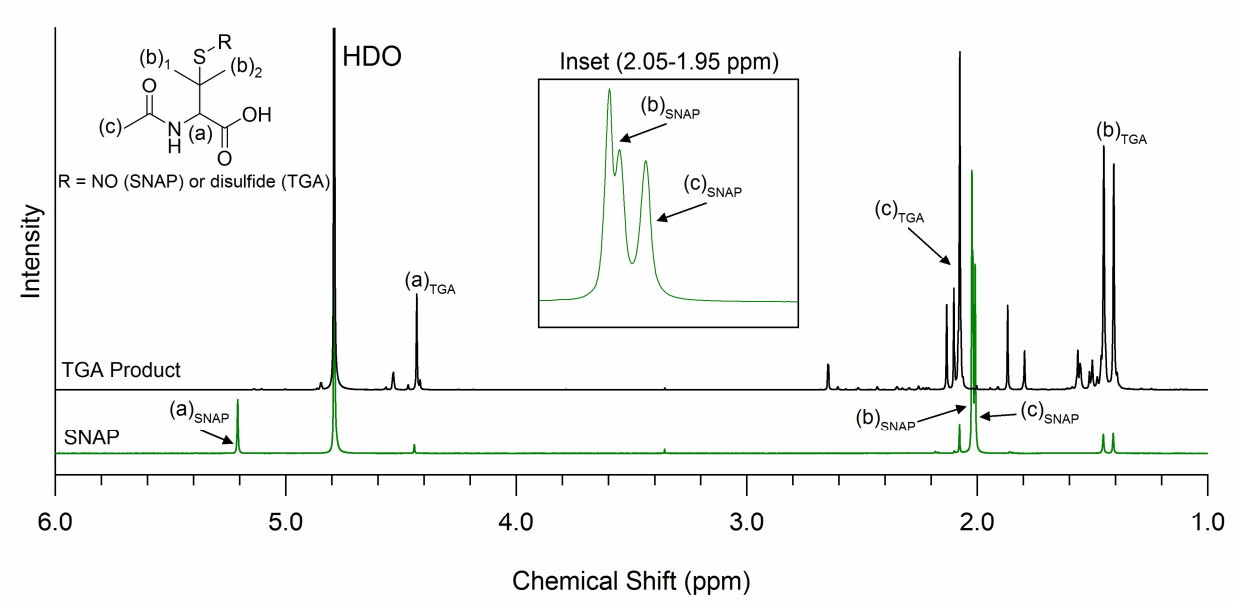

Figure 2.9. ^{1}H NMR spectra comparing SNAP TGA product to SNAP. Spectrum acquired in D_2O at 25 °C.

In contrast, SNAP (220.24 g mol^{-1}; $C_7H_{12}N_2O_4S$) experienced a 15.2 ± 0.6% decrease in weight following TGA experiments, modestly exceeding the theoretical value of 13.6% that corresponds to exclusive loss of NO. This discrepancy may indicate that thermal decomposition of SNAP or SNAP products is not limited to homolytic cleavage of the S-N bond and subsequent release of NO. At 132 °C, TGA-MS revealed the evolution of species of 30 *m*/*z* consistent with NO release and continued through the remainder of the experiment (Fig. 2.6). Heating to a final temperature of 145 °C during thermal analysis produced a yellow oil that was difficult to collect from the pan. During TGA, SNAP exhibited continuous mass loss after 132 °C (Fig. 2.7), likely due to concurrent melting and decomposition of both SNAP and NAP disulfide. This hypothesis can be inferred from visual observations of the SNAP product, as well as reported melting points of SNAP (152-154 °C) and NAP disulfide (128-131 °C).[26] In both cases, prior literature indicates melting is accompanied by decomposition. Although these referenced observations are not derived from rigorous thermal analyses, it is clear that a binary mixture of SNAP and NAP

disulfide must experience multiple thermal transitions and decomposition processes when heated to 145 °C. When using a lower final temperature of 140 °C, a resinous, light blue-green solid could be recovered and characterized by ATR-FTIR and ^{1}H NMR. ATR-FTIR spectra (Fig. 2.8) revealed the absence of the diagnostic N=O stretching band at 1497 cm^{-1}, supporting decomposition of the RSNO functional group. ^{1}H NMR analysis of the SNAP TGA product (Fig. 2.9) indicates that thermal decomposition of SNAP primarily yields NAP disulfide, as well as other unidentified compounds that may represent significant products. Accurate-mass TOF-MS was used to confirm the presence of NAP disulfide (379.1020 *m*/*z*, $[M-H]^-$), as well as homologous tri- and tetrasulfides (411.0734 and 443.0438 *m*/*z*, $[M-H]^-$) that may contribute to the unknown products detected by ^{1}H NMR (Table 2.1). The presence of these higher sulfides may be rationalized as the outcome of various radical combination events that occur during thermal decomposition.[31] We propose that the NO-producing decomposition of SNAP at 132.8 ± 0.9 °C results in formation of NAP disulfide, which is itself thermally unstable and undergoes

Table 2.1. TOF-MS analysis of SNAP after TGA

m/z	Formula	Mass Error (ppm)	Assignment
156.0670	$[C_7H_{11}NO_3 - H]-$	−2.46	NAP, sulfur elimination product
190.0554	$[C_7H_{13}NO_3S - H]^-$	−5.59	NAP
219.0458	$[C_7H_{12}N_2O_4S - H]^-$	−5.93	SNAP
379.1020	$[C_{14}H_{24}N_4O_{12}S_2 - H]^-$	−4.48	NAP disulfide
411.0746	$[C_{14}H_{24}N_4O_{12}S_3 - H]^-$	−5.42	NAP trisulfide
443.0443	$[C_{14}H_{24}N_4O_{12}S_4 - H]^-$	0.32	NAP tetrasulfide
759.2092	$[C_{28}H_{48}N_4O_{12}S_4 - H]^-$	−1.74	NAP disulfide dimer

further decomposition to produce the series of products observed by MS. This accumulation of products may result in a eutectic mixture that is molten below the 152-154 °C melting range of SNAP and perhaps facilitates more rapid or complex decomposition.

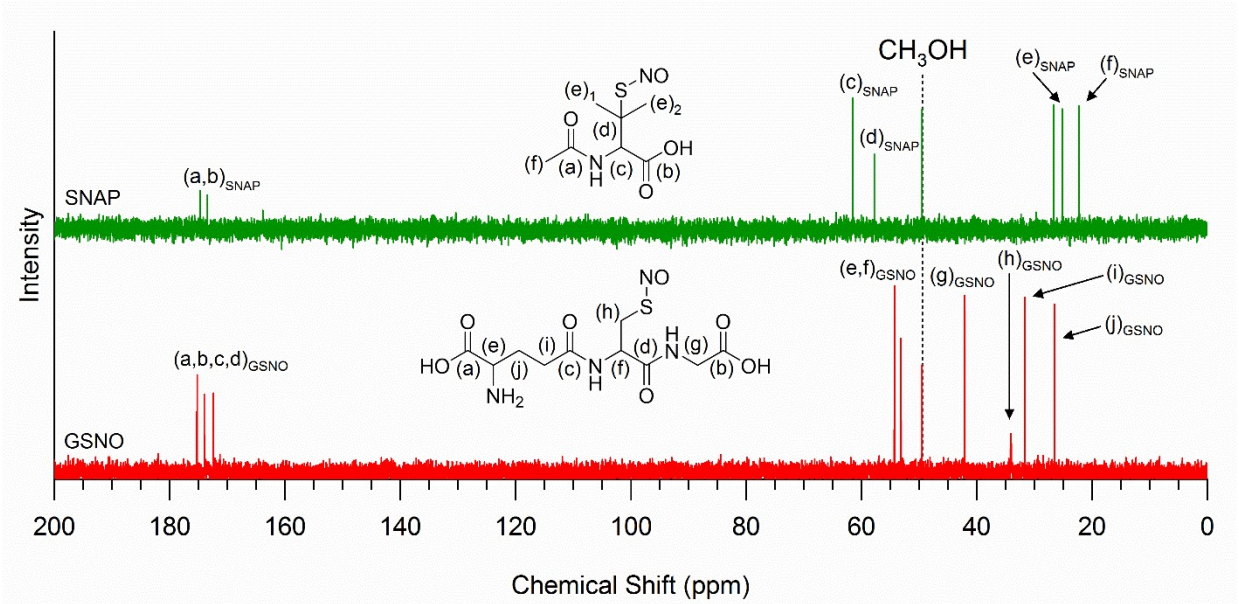

Figure 2.10. ^{13}C NMR spectra comparing GSNO (red) and SNAP (green). Spectrum acquired in D_2O at 25 °C with 1 µL mL^{-1} methanol added as an internal reference.

The mean NO-forming decomposition of SNAP (132.8 ± 0.9 °C) occurs at a lower temperature than the equivalent phenomenon in GSNO (134.7 ± 0.8 °C). In solution, it is believed that the rate of RSNO decomposition is influenced by steric considerations during thiyl combination,[25] as well as the possibility of both geminate and non-geminate recombination of thiyl and NO radicals.[21] Since these complex reaction equilibria are unlikely to become established during high-temperature thermal decomposition, it is feasible that TGA results reflect a genuine difference in S-N bond stability. On this basis, Bainbrigge *et al.* reasoned that geminal dimethyl substitution in SNAP did not significantly influence the stability of the S-N bond, due to apparently identical decomposition temperatures of 148 °C. Our higher resolution data suggests that SNAP exhibits modestly decreased stability, which may be attributable to tertiary

substitution. In any event, it is evident that tertiary substitution influences the electronic environment of the RSNO functional group. In GSNO, the RSNO carbon is primary and exhibits a ^{13}C NMR chemical shift of 34.03 ppm (Fig. 2.10). In SNAP, the dimethyl-substituted tertiary RSNO carbon is shifted downfield to 57.77 ppm and is comparatively electron deficient. A similar deshielding effect has been observed using ^{15}N NMR which indicates that geminal dimethyl substitution exerts a considerable influence on the electronic properties of the RSNO functional group.[32]

2.4.2 Effect of Temperature on Solution Stability

RSNO stability as a function of temperature and pH has been previously examined,[22,23,33] but many older studies neglect to account for the presence of trace metal ions which catalyze the decomposition of RSNOs.[14] de Souza et al. report chelation protocols;[34] however, the magnitude of the impact of trace metal ions on RSNO stability is seldom quantified. We conducted an experiment in which the decomposition of GSNO and SNAP was compared in PBS (pH 7.4) prepared in ultrapure water (18.2 MΩ·cm) with and without 100 μM EDTA (Table 2.2). Over 24 h, both RSNOs exhibited statistically greater (p <0.01) decomposition without the chelator in solution, particularly in the case of SNAP, which underwent near complete decomposition. Because the absence of EDTA results in accelerated decomposition even when buffer solutions are prepared with ultrapure water, we hypothesize that metal ions may be introduced by glassware or the RSNOs themselves. The particular sensitivity of SNAP to the absence of EDTA could be explained by a higher concentration of adventitious copper or perhaps a greater inherent susceptibility to decomposition by trace metal ions. Furthermore, it is known that GSNO is capable of chelating and inactivating copper ions in a self-stabilizing manner, which could also account for this difference.[2] The individual components of our experiments were determined to

contain ≤0.2 μM copper (method detection limit) by ICP-AES (Table 2.3). It has been reported previously that copper ion concentrations as low as 10^{-5} to 10^{-6} M (typical of buffer components) are capable of decomposing RSNOs.[35] Although we fail to detect copper using ICP-AES, its presence in trace quantities is evidently a factor in the stability of GSNO and SNAP, reinforcing the necessity of trace metal chelation for proper evaluation and use of RSNO solutions.

Table 2.2. Percent decomposition of RSNOs in the presence and absence of metal ion chelators.

	Average decomposition (%)[a]	
RSNO[b]	**Chelator**[c]	**Without chelator**
GSNO[d]	1.4 ± 0.2	2.5 ± 0.2
SNAP[d]	10.8 ± 0.3	98.0 ± 0.1

[a] Average decomposition measured over 24 h. Data reported as mean ± SD of $n \geq 3$ replicate measurements.
[b] RSNO (1.5×10^{-3} M; PBS; pH 7.4).
[c] EDTA (100 μM).
[d] Average decomposition statistically different ($p < 0.01$) in the presence and absence of metal ion chelator by two-tailed Student's t-test.

Table 2.3. Copper concentration of each component of stability experiments.

Component	**Concentration (M)**	**Copper Concentration (mg L^{-1})**[a,b]
GSNO	1.5×10^{-3}	<LoD
SNAP	1.5×10^{-3}	<LoD
PBS	1.0×10^{-2}	<LoD
Citric acid	0.1	<LoD
Na_2HPO_4	0.2	<LoD
EDTA	1.0×10^{-3}	<LoD

[a] Each component of the experiments was analyzed by ICP-AES to determine the copper concentration (0.2 μM LoD).
[b] Tabulated data of $n = 3$ replicate measurements is reported.

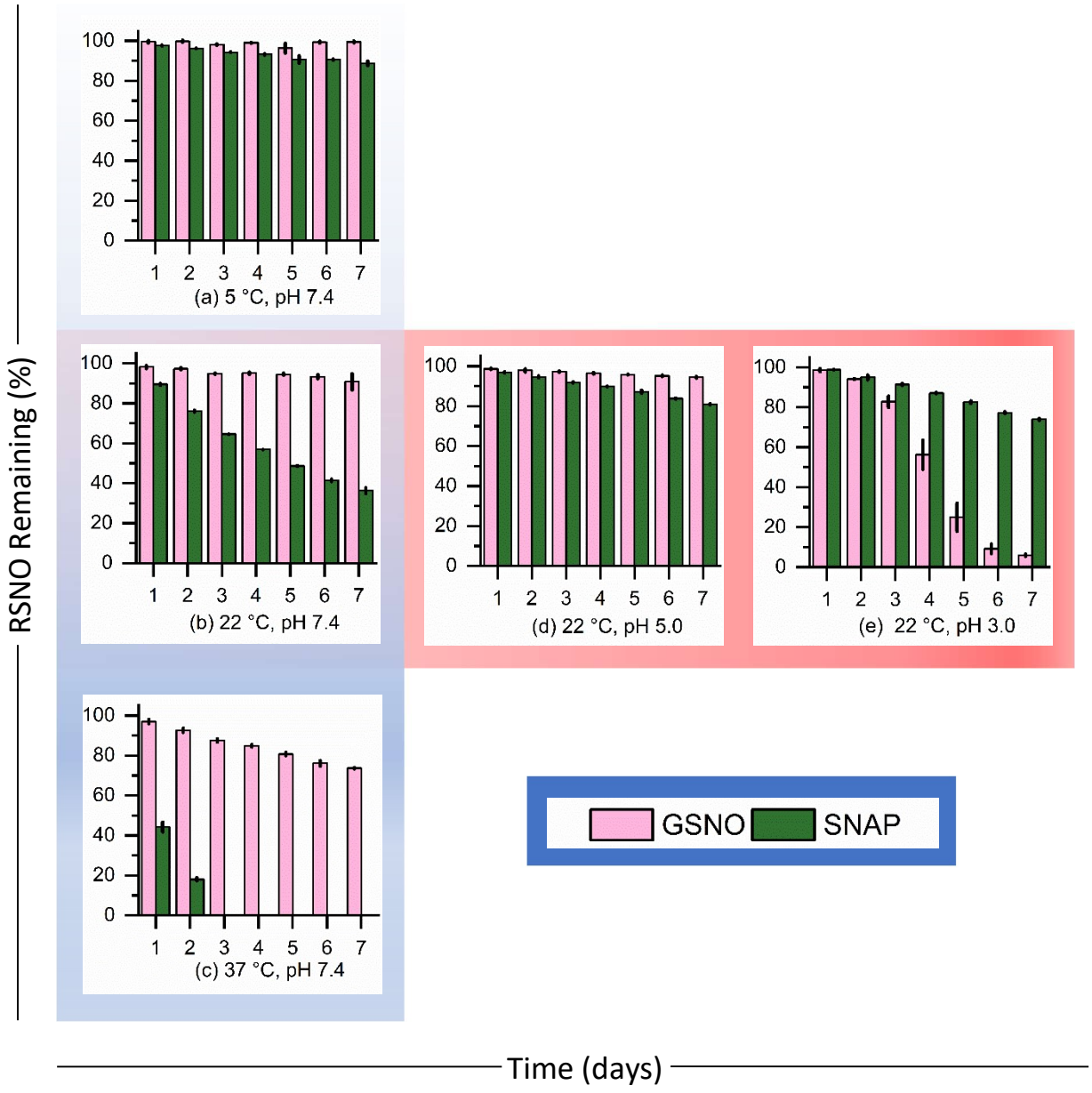

Figure 2.11. RSNO solution stability as a function of temperature (PBS) and pH (citric acid/Na_2HPO_4 buffer) at (a) 5 °C, pH 7.4 (b) 22 °C, pH 7.4, (c) 37 °C, pH 7.4 (d) 22 °C, pH 5.0 and (e) 22 °C, pH 3.0. GSNO (1.5×10^{-3} M; monitored at 335 nm) and SNAP (1.5×10^{-3} M; monitored at 339 nm) decay monitored over a one-week period. Data reported as mean ± SD of $n \geq 3$ replicate measurements.

We evaluated the effect of temperature on the relative stability of 1.5×10^{-3} M solutions of GSNO and SNAP (PBS; pH 7.4) with 100 μM EDTA as the chelating species. The three temperatures tested were 5 °C (refrigeration), 22 °C (room temperature), and 37 °C (physiological) due to their relevance in laboratory settings. Our results indicate increased RSNO stability with decreasing temperature (Fig. 2.11). At 5 °C, GSNO showed minimal (0.4 ± 0.6%) decomposition over a 7-day period, suggesting light-free refrigeration is sufficient for preserving samples over this timespan. In contrast, SNAP decomposed 2.3 ± 0.3% after 1 day and 11 ± 1% after 1 week, which suggests that solutions of SNAP should be prepared immediately prior to use. After 1 week at 22 °C, GSNO and SNAP exhibited 10 ± 4 and 64 ± 1% decomposition, respectively, revealing an even greater difference in stability between the two RSNOs. At 37 °C, GSNO decomposed 3 ± 1% in a 24 h period and 26 ± 1% over 7 days, whereas SNAP was almost fully decomposed after 2 days (82 ± 1%). Depending on the application, GSNO is apparently more suitable for experiments in which prolonged stability is required under physiological temperatures. In contrast, SNAP in aqueous solution is clearly susceptible to rapid decomposition. The results of these solution-phase stability studies are unremarkable and consistent with our solid-phase TGA experiments, which suggest that the S-N bond in SNAP may be marginally weaker than in GSNO. However, it has been observed elsewhere that SNAP exhibits remarkable resistance to decomposition (<12% over 8 months) at 37 °C when crystallized within a polymer matrix, an outcome that was attributed to the stabilizing effect of intermolecular hydrogen bonding.[36] We must therefore conclude that the observed stability of SNAP is highly contingent upon phase and local chemical environment, although dissolution in water assuredly accelerates decomposition. Interestingly, our IR data indicates that the N=O stretching frequency of crystalline SNAP is 20 cm^{-1} greater than that of GSNO (1477 cm^{-1}),

which may be indicative of a stronger N=O bond. The RSNO functional group is frequently described in terms of the three distinct resonance forms depicted in Fig. 2.12, and contribution of the S=N bond in structure **I** may rationalize the existence of *syn*/*anti* conformers that produce the characteristic red-pink color of primary and secondary RSNOs (*syn*) and green tertiary RSNOs (*anti*). Chemical factors that increase the contribution of structure **I** are theorized to impart greater resistance to homolytic cleavage, which is clearly disfavored by the presence of the double bond. The apparent strength of the N=O bond in SNAP suggests that the relative contribution of structure **I** may be reduced compared to GSNO, where hydrogen bonding to the RSNO oxygen may favor the double-bonded form and lower the frequency at which the ν(N=O) mode is observed. However, it is also feasible that ν(N=O) frequency differences are a direct consequence of *syn*/*anti* conformation and do not provide insight into the local hydrogen bonding environment.[37]

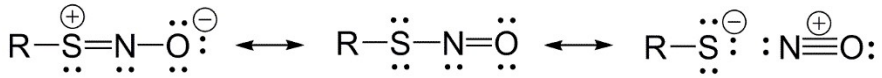

Figure 2.12. RSNO resonance structures.

In a recent study, de Souza et al. examined the long-term (>35 days) solution stability of 1×10^{-3} M solutions of the primary RSNOs GSNO and *S*-nitroso-*N*-acetylcysteine (SNAC) in pH 7 PBS containing 0.1 wt.% EDTA.[34] Their results support an inverse relationship between temperature and RSNO stability for both RSNOs. They found that GSNO was less stable than SNAC at all tested temperatures (15, 25, 30, 35, and 40 °C) and that both were modestly stable (<5% decomposition) at 15 °C over several weeks. Interestingly, we observed that SNAP (a tertiary analogue of SNAC) is *less* stable than GSNO in pH 7.4 PBS at 5, 22, and 37 °C, in spite of geminal dimethyl substitution of the RSNO carbon that has been thought to confer additional

stability relative to primary RSNOs.[23] Indeed, our combined studies suggest that the order of stability is SNAC > GSNO > SNAP at neutral or near-neutral pH.

To explain the exceptional stability of SNAC, de Souza et al. invoke the formation of a seven-membered ring through hydrogen bonding between the carbonyl oxygen of the acetamido group and the hydrogen atom of the protonated carboxylic acid group.[21] The formation of this seven-membered ring facilitates a favorable hydrogen bonding interaction between the *syn* RSNO oxygen and the amide hydrogen, which acts to stabilize the molecule with respect to NO-forming decomposition. However, this model does not directly address the likelihood that the carboxylic acid group of SNAC will be predominately deprotonated at or above neutral pH. In computational studies, Meyer et al. developed an alternative model in which a *five*-membered ring involving a negatively-charged carboxylate oxygen and the amide hydrogen is favored at physiological pH.[38] This configuration may stabilize SNAC through formation of an unusual hydrogen bond-like interaction between the RSNO oxygen and hydrogen atoms bound to the RSNO carbon, a phenomenon that is impossible in tertiary substrates such as SNAP. In solids, the feasibility of this interaction is potentially supported by crystal structures of *S*-nitrosocaptopril and the ethyl ester of *S*-nitrosocysteine, in which the NO moiety preferentially eclipses a C-H bond of the RSNO carbon.[39] Meyer et al. argued that this interaction may explain preference for the *syn* conformation in primary RSNOs, while *trans* is preferred in tertiary substrates. Furthermore, Meyer et al. identified that both SNAC and SNAP are subject to a chalcogen-chalcogen interaction between the thiyl radical generated as a decomposition intermediate and the neighboring carboxylate group. The magnitude of this interaction was greater in the case of SNAP which may stabilize the sulfur-centered radical and consequently promote decomposition. This model appears to be generally consistent with the

reduced stability of SNAP compared to SNAC and may partially rationalize the apparent stability of GSNO. If the proposed hydrogen bonding interaction between the RSNO oxygen and hydrogen atoms bound to the RSNO carbon is the major factor that determines *syn*/*anti* configuration, then GSNO may also experience this interaction. This possibility is supported by the red-pink color of GSNO, which arises from an absorbance maximum at 545 nm ($n_N \rightarrow \pi^*$) that is attributable to the electronic properties of the *syn* conformer. Furthermore, GSNO lacks neighboring carboxylate groups to stabilize intermediate thiyl radicals. We hypothesize that a combination of the intramolecular effects described by Meyer et al. and the ability of GSNO to chelate copper ions are largely responsible for its greater stability relative to SNAP. Curiously, we observed that the red-pink color of GSNO is retained when cooled with liquid nitrogen, while SNAP loses its green color and develops a vivid pink appearance (Fig. 2.13). This property is not shared with *S*-nitrosotriphenylmethanethiol, a tertiary RSNO that remains green when cooled in an identical manner. We propose that this observation may be indicative of an unexpected temperature-dependent conformational change in SNAP from *anti* to *syn*, although the apparent color change may also represent a conformationally-unrelated hypsochromic shift of the $n_N \rightarrow \pi^*$ transition at 591 nm or other purely electronic or optical phenomenon.

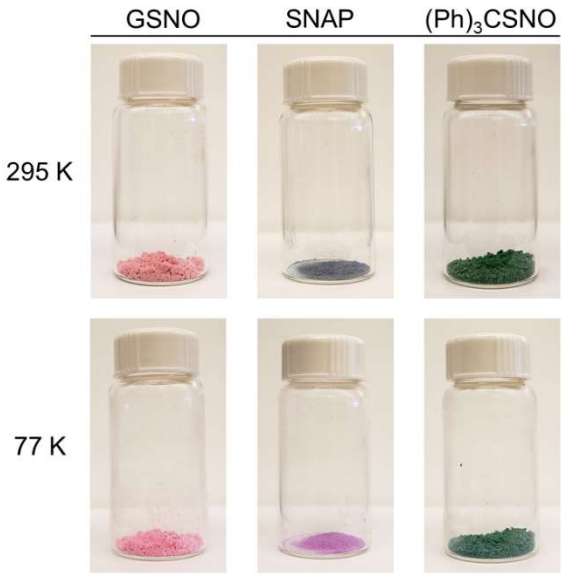

Figure 2.13. Comparison of GSNO, SNAP, and *S*-nitrosotriphenylmethanethiol ($(Ph)_3CSNO$) at ambient temperature (295 K) and after cooling with liquid N_2 (77 K).

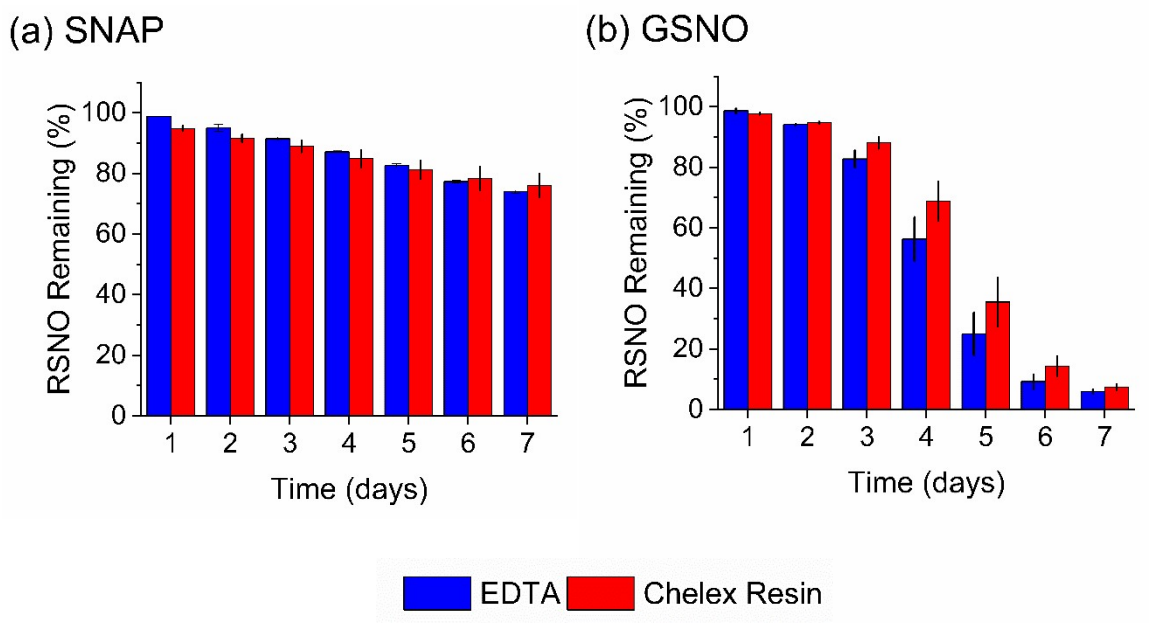

Figure 2.14. Comparison of average decomposition of SNAP and GSNO at pH 3.0 using EDTA (blue) or Chelex resin (red) as the chelator.

2.4.3 Effect of pH on Solution Stability

The majority of studies examining the influence of pH on RSNO stability hypothesize that RSNOs exhibit enhanced solution stability in acidic media[13,22,23] while one study reports enhanced stability in mildly basic media.[33] To address this apparent discrepancy, we used GSNO and SNAP to assess the comparative stability of RSNOs at physiological (PBS; pH 7.4) and mildly acidic (citric acid/Na_2HPO_4 buffer; pH 5.0 and 3.0) pH over 7 days. The results of this pH variation study are presented in Fig. 2.11. Compared with experiments performed at pH 7.4, GSNO and SNAP exhibit an appreciable increase in stability at pH 5.0. Acidic conditions may stabilize RSNOs by protonation of the RSNO oxygen, leading to enhanced S-N bond strength via resonance, as depicted in Fig. 2.12(**I**).[21-24] However, a further decrease in pH to 3.0 demonstrated that SNAP is *less* stable than at pH 5.0 (p <0.01). In the case of GSNO, a distinct decomposition phenomenon manifests at pH 3.0. Over 2 days, GSNO shows a similar linear decomposition rate to that of SNAP. However, from 3-7 days, GSNO exhibited a rapid increase in decomposition as indicated in Fig. 2.11e. This unusual decomposition behavior was also observed when EDTA was replaced with 1 w/v % Chelex 100, a solid phase iminodiacetic acid chelating resin active in strongly basic to weakly acidic solutions (Fig. 2.14).[40] The possibility that copper is directly responsible for the increased rate of decomposition at pH 3.0 is unlikely, considering that the effect requires several days to manifest and does not extend to SNAP. One hypothesis for this irregular behavior is that peptide bonds in GSNO are slowly hydrolyzed at pH 3.0, ultimately resulting in decay of the entire molecule. However, peptide bonds are reasonably stable, and hydrolysis by 6 M HCl at 110 °C is a slow process.[41] A second hypothesis is that GSNO exhibits autocatalytic decomposition at pH 3.0, indicated by the possible sigmoidal decay behavior. Potential factors capable of inducing this rapid decay are oxygenated conditions or the presence

of thiols in solution. One possible aerobic mechanism is N_2O_3-catalyzed decomposition resulting from reaction of NO and oxygen.[42] Oxygenated conditions have also been proposed to effect nitrosonium-catalyzed decomposition, which is perhaps enhanced at low pH where the production of nitrosonium is likely more favorable.[20] Thiols such as GSH may accelerate decomposition by reducing Cu^{2+} to Cu^{+}, the active form of copper in the metal ion-mediated RSNO decomposition mechanism.[12,14] To assess these hypotheses, we performed experiments under anaerobic conditions and with the addition of *N*-ethylmaleimide (NEM) as a thiol scavenger (Table 2.4). We found that GSNO exhibited similar, if not more rapid, decomposition behavior in the presence of NEM. Interestingly, in the absence of oxygen GSNO was more stable and exhibited linear decomposition. This observation may be explained as the inhibition of autocatalytic decomposition under anaerobic conditions.[42,43] As described by Grossi et al., the formation of N_2O_3 may catalyze the rapid decomposition of RSNOs.[42] The rate of this N_2O_3-mediated chain reaction decreases as the substituents of the RSNO carbon increase in steric bulk, suggesting that GSNO (primary) may be more inherently susceptible to this pathway than SNAP (tertiary) in a manner consistent with our observations. Because N_2O_3 exists in equilibrium with nitrous acid (the immediate oxidation product of NO; pK_a 3.16), it seems reasonable to hypothesize that this pathway is particularly influential at lower pH values and therefore manifests in our study at pH 3.0.[44,49] In a related study using the same citric acid/Na_2HPO_4 buffer system, de Souza et al. observed that GSNO exhibited first-order exponential decay kinetics at pH 3.[34] After 10 days, GSNO appeared to be fully decomposed, which aligns reasonably well with our observation that GSNO was almost fully decomposed by 7 days. However, de Souza et al. observed greater comparative GSNO stability at pH 7 than pH 5 over a period of 30 days, while we observe that GSNO is marginally more stable at pH 5.0 over 7 days. To explain this

phenomenon, de Souza et al. argue somewhat tautologically that the biological role of GSNO may obligate increased stability at physiological pH. We note that a modest increase in RSNO stability is a predicted effect of acidic conditions, in line with our own observations of both GSNO and SNAP. In any case, the solution stability of RSNOs in mildly acidic or physiological media is likely to be influenced by a variety of factors, including solvent, the presence of ionizable functional groups, and resulting intra- and intermolecular hydrogen bonding interactions.

Table 2.4. Percent decomposition of GSNO at pH 3.0 excluding oxygen and thiols

	Average decomposition (%)[a,b]		
Time (days)	**Aerobic conditions**	**Anaerobic conditions**	**Thiol scavenger**[c]
1	98.6 ± 0.8	96.9 ± 0.5	97.8 ± 0.9
2	94.1 ± 0.2	94.9 ± 0.1	91.1 ± 0.7
3	83 ± 3	92.7 ± 0.9	76 ± 2
4	56 ± 7	89.5 ± 0.6	38 ± 3
5	25 ± 7	88 ± 2	13.1 ± 0.8
6	9 ± 2	85 ± 2	7.5 ± 0.3
7	6.0 ± 0.6	82 ± 1	7.5 ± 0.5

[a] Average decomposition measured over 24 h. Data reported as mean ± SD of $n \geq 3$ replicate measurements.
[b] GSNO (1.5×10^{-3} M; citric acid buffer; pH 3.0; 100 μM EDTA).
[c] N-Ethylmaleimide (1 mM).

2.3.4 Solution Stability with Fluorescent Light Exposure

Although susceptibility of RSNOs to photolytic decomposition has been established, short-term exposure of RSNOs to laboratory lighting is rarely considered a major concern. In fact, it has been advised that the photolytic vulnerability of RSNOs is minimal in the absence of strong, direct light and that particular caution is necessary only in pharmacological studies.[17] Since preparation, handling, and use of RSNO solutions may amount to multiple hours of light exposure, we conducted photolytic decomposition studies over 7 h to evaluate the stability of

GSNO and SNAP under laboratory lighting conditions in a hood (d = 122 cm, 861 lux) in a typical workday. The fluorescent light emits wavelengths from 425 nm to 650 nm (Fig. 2.14). Both GSNO and SNAP were highly susceptible to photolytic decomposition from this light source, as shown in Fig. 2.15. RSNOs have two characteristic absorption bands, one in the 330-335 nm range and one in the 550-600 nm range.[13] The spectrum of the fluorescent light source strongly overlaps with the RSNO absorption band in the visible light region, which is known to accelerate RSNO decomposition.[46] After only 1 h of light exposure, the concentration of a 1.5 $\times 10^{-3}$ M GSNO solution (PBS; pH 7.4) had decreased to 97.9 ± 1.0% of the original value, while SNAP exhibited a comparable decrease to 95.6 ± 0.1%. Both RSNO solutions continued to decompose linearly in proportion to exposure time, with SNAP exhibiting greater susceptibility to visible light-induced decomposition (69.7 ± 1.6% remaining after 7 h) compared to GSNO (80.8 ± 0.5% remaining after 7 h) (p <0.01). For comparison, GSNO decomposed 98.2 ± 0.8% and SNAP decomposed 89.5 ± 0.5% over 24 h in the absence of light under the same conditions. These results show that, even over a 1 h timescale, minimizing lab lighting and utilizing amber glassware is important for maintaining RSNO solution purity. Further considerations include usage of dark rooms or high wavelength (>600 nm) lighting (Fig. 2.16) when handling RSNO samples.

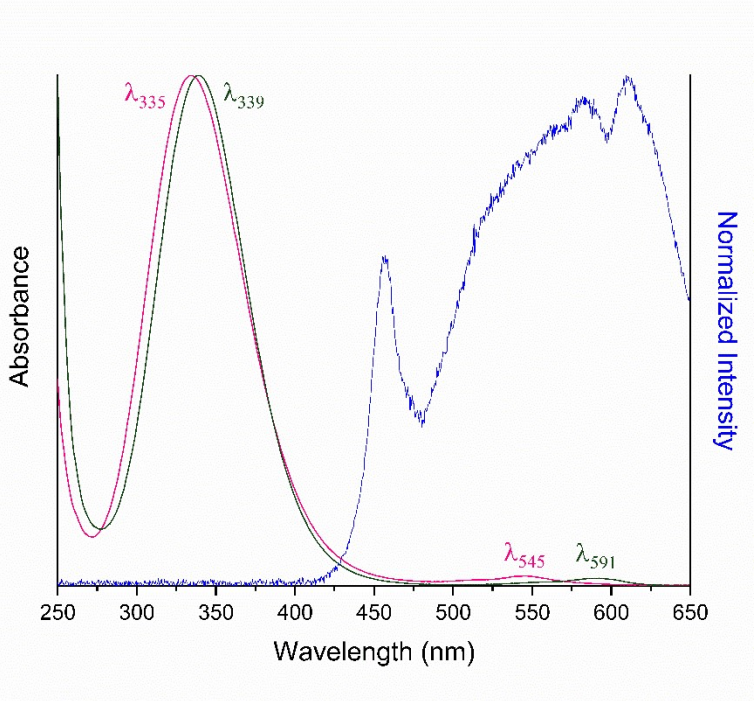

Figure 2.14. Absorbance spectrum of GSNO (pink) and SNAP (green) compared to the intensity of the fluorescent laboratory lighting (861 lux) (blue).

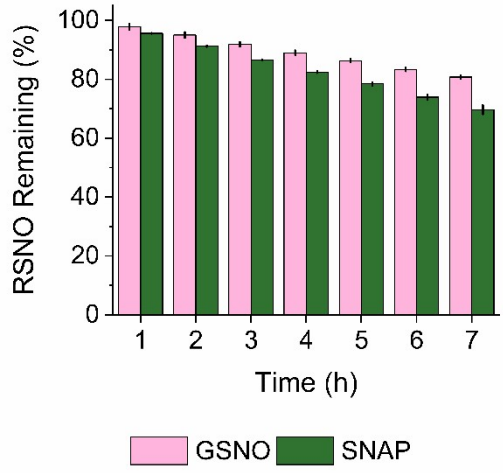

Figure 2.15. RSNO solution stability as a function of white light exposure. GSNO (1.5×10^{-3} M; PBS; pH 7.4; monitored at 335 nm) and SNAP (1.5×10^{-3} M; PBS; pH 7.4; monitored at 339 nm) decay monitored over 7 h with source to sample distance of d = 122 cm (861 lux). Data reported as mean ± SD of n ≥ 3 replicate measurements.

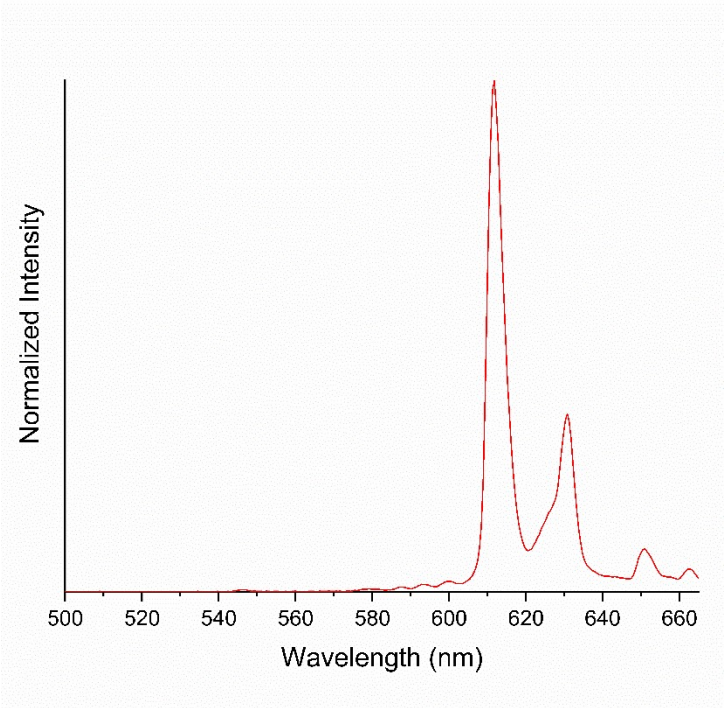

Figure 2.16. Wavelengths emitted from a red light bulb. The absorption bands of GSNO are outside the range of this light source. The absorption band of SNAP in the visible light region (λ = 591) overlaps with the low end of these wavelengths, however the wavelengths are relatively weak.

2.4. Conclusions

In all but one circumstance, GSNO displayed greater stability than SNAP. Data collected from TGA experiments indicated that both RSNOs release NO at temperatures 15 °C below what has been previously reported in the literature. Notably, the thermal decomposition temperatures at which homolytic cleavage of the S-N bond occurs for GSNO (134.7 °C) and SNAP (132.8 °C) were significantly different. GSNO decomposed to yield GSSG stoichiometrically, whereas decomposition of SNAP produced NAP disulfide and tri- and tetrasulfides. In the presence of metal ion chelators in solution, GSNO is stable enough to be stored in a refrigerator for at least 1 week with negligible decomposition. In contrast, it is recommended that SNAP be prepared daily. Additionally, for studies at physiological temperature and pH, SNAP is preferred for uses that require rapid NO release and GSNO is preferred for uses that require greater stability. If

storage at room temperature is preferred or required, decreasing the pH of solutions of GSNO and SNAP to 5.0 would increase stability and prolong the shelf life. The most important consideration, arguably, is the effect of fluorescent laboratory lighting on the stability of RSNOs. Both GSNO and SNAP were appreciably sensitive to photolytic decomposition on an hourly timescale, highlighting the need for effective light shielding techniques during preparation and storage. Further studies are warranted to elucidate the conditions for optimal stability of these RSNOs.

CHAPTER 2

REFERENCES

(1) Giustarini, D.; Milzani, A.; Colombo, R.; Dalle-Donne, I.; Rossi, R. Nitric Oxide and *S*-Nitrosothiols in Human Blood. *Clin. Chim. Acta* **2003**, *330* (1–2), 85–98.

(2) Broniowska, K. A.; Diers, A. R.; Hogg, N. *S*-NITROSOGLUTATHIONE. *Biochim. Biophys. Acta* **2013**, *1830* (5), 3173–3181.

(3) Broniowska, K. A.; Hogg, N. The Chemical Biology of *S*-Nitrosothiols. *Antioxid. Redox Signal.* **2012**, *17* (7), 969–980.

(4) Major, T. C.; Brant, D. O.; Burney, C. P.; Amoako, K. A.; Annich, G. M.; Meyerhoff, M. E.; Handa, H.; Bartlett, R. H. The Hemocompatibility of a Nitric Oxide Generating Polymer That Catalyzes *S*-Nitrosothiol Decomposition in an Extracorporeal Circulation Model. *Biomaterials* **2011**, *32* (26), 5957–5969.

(5) Major, T. C.; Handa, H.; Brisbois, E. J.; Reynolds, M. M.; Annich, G. M.; Meyerhoff, M. E.; Bartlett, R. H. The Mediation of Platelet Quiescence by NO-Releasing Polymers via CGMP-Induced Serine 239 Phosphorylation of Vasodilator-Stimulated Phosphoprotein. *Biomaterials* **2013**, *34* (33), 8086–8096.

(6) Hopkins, S. P.; Pant, J.; Goudie, M. J.; Schmiedt, C.; Handa, H. Achieving Long-Term Biocompatible Silicone via Covalently Immobilized *S*-Nitroso-*N*-Acetylpenicillamine (SNAP) That Exhibits 4 Months of Sustained Nitric Oxide Release. *ACS Appl. Mater. Interfaces* **2018**, *10* (32), 27316–27325.

(7) Brisbois, E. J.; Handa, H.; Meyerhoff, M. E. Recent Advances in Hemocompatible Polymers for Biomedical Applications. In Advanced Polymers in Medicine; *Springer International Publishing: Cham,* **2015**; pp 481–511.

(8) Brisbois, E. J.; Handa, H.; Major, T. C.; Bartlett, R. H.; Meyerhoff, M. E. Long-Term Nitric Oxide Release and Elevated Temperature Stability with *S*-Nitroso-*N*-Acetylpenicillamine (SNAP)-Doped Elast-Eon E2As Polymer. *Biomaterials* **2013**, *34* (28), 6957–6966.

(9) Neufeld, B. H.; Reynolds, M. M. Critical Nitric Oxide Concentration for Pseudomonas Aeruginosa Biofilm Reduction on Polyurethane Substrates. *Biointerphases* **2016**, *11* (3), 031012.

(10) Giri, S.; Rattan, R.; Deshpande, M.; Maguire, J. L.; Johnson, Z.; Graham, R. P.; Shridhar, V. Preclinical Therapeutic Potential of a Nitrosylating Agent in the Treatment of Ovarian Cancer. *PLoS One* **2014**, *9* (6), 1–11.

(11) Gould, N.; Doulias, P. T.; Tenopoulou, M.; Raju, K.; Ischiropoulos, H. Regulation of Protein Function and Signaling by Reversible Cysteine *S*-Nitrosylation*. *J. Biol. Chem*. **2013**, *288* (37), 26473–26479.

(12) Dicks, A. P.; Swift, H. R.; Williams, D. L. H.; Butler, A. R.; Al-Sa'doni, H. H.; Cox, B. G. Identification of Cu^{+} as the Effective Reagent in Nitric Oxide Formation from S-Nitrosothiols (RSNO). *J. Chem. Soc. Perkin Trans. 2* **1996**, *No. 1*, 481–487.

(13) Williams, D. L. H. The Chemistry of *S*-Nitrosothiols. *Acc. Chem. Res.* **1999**, *32* (10), 869–876.

(14) Singh, R. J.; Hogg, N.; Joseph, J.; Kalyanaraman, B. Mechanism of Nitric Oxide Release from *S*-Nitrosothiols. *J. Biol. Chem.* **1996**, *271* (31), 18596–18603.

(15) Wu, Y.; Zhang, F.; Wang, Y.; Krishnamoorthy, M.; Roy-Chaudhury, P.; Bleske, B. E.; Meyerhoff, M. E. Photoinstability of *S*-Nitrosothiols during Sampling of Whole Blood: A Likely Source of Error and Variability in *S*-Nitrosothiol Measurements. *Clin. Chem.* **2008**, *54* (5), 916–918.

(16) Pant, J.; Goudie, M. J.; Hopkins, S. P.; Brisbois, E. J.; Handa, H. Tunable Nitric Oxide Release from *S*-Nitroso-*N*-Acetylpenicillamine via Catalytic Copper Nanoparticles for Biomedical Applications. *ACS Appl. Mater. Interfaces* **2017**, *9* (18), 15254–15264.

(17) Hogg, N. Biological Chemistry and Clinical Potential of *S*-Nitrosothiols. *Free Radic. Biol. Med.* **2000**, *28* (10), 1478–1486.

(18) Blanchard, B.; Servy, C.; Ducrocq, C. Chemical Evaluation of Compounds as Nitric Oxide or Peroxynitrite Donors Using the Reactions with Serotonin. *Free Radic. Res.* **2001**, *34* (2), 189–191.

(19) Stamler, J. S.; Toone, E. J. The Decomposition of Thionitrites. *Curr. Opin. Chem. Biol.* **2002**, *6* (6), 779–785.

(20) Zhao, Y. L.; McCarren, P. R.; Houk, K. N.; Choi, B. Y.; Toone, E. J. Nitrosonium-Catalyzed Decomposition of *S*-Nitrosothiols in Solution: A Theoretical and Experimental Study. *J. Am. Chem. Soc.* **2005**, *127* (31), 10917–10924.

(21) de Oliveira, M. G.; Shishido, S. M.; Seabra, A. B.; Morgon, N. H. Thermal Stability of Primary *S*-Nitrosothiols: Roles of Autocatalysis and Structural Effects on the Rate of Nitric Oxide Release. *J. Phys. Chem. A* **2002**, *106* (38), 8963–8970.

(22) Heikal, L.; Martin, G. P.; Dailey, L. A. Characterisation of the Decomposition Behaviour of S-Nitrosoglutathione and a New Class of Analogues: *S*-Nitrosophytochelatins. *Nitric Oxide* **2009**, *20* (3), 157–165.

(23) Roy, B.; du Moulinet d'Hardemare, A.; Fontecave, M. New Thionitrites: Synthesis, Stability, and Nitric Oxide Generation. *J. Org. Chem.* **1994**, *59* (23), 7019–7026.

(24) Timerghazin, Q. K.; Peslherbe, G. H.; English, A. M. Resonance Description of *S*-Nitrosothiols: Insights into Reactivity. *Org. Lett.* **2007**, *9* (16), 3049–3052.

(25) Bainbrigge, N.; Butler, A. R.; Görbitz, C. H. The Thermal Stability of *S*-Nitrosothiols: Experimental Studies and Ab Initio Calculations on Model Compounds. *J. Chem. Soc. Perkin Trans. 2* **1997**, *No. 2*, 351–353.

(26) Field, L.; Dilts, R. V.; Ravichandran, R.; Lenhert, P. G.; Carnahan, G. E. An Unusually Stable Thionitrite from *N*-Acetyl-D,L-Penicillamine; X-Ray Crystal and Molecular Structure of 2-(Acetylamino)-2-Carboxy-l,Ldimethylethyl Thionitrite. *J. C. S. Chem. Comm.* **1978**, 249–250.

(27) Moynihan, H. A.; Roberts, S. M. Preparation of Some Novel *S*-Nitroso Compounds as Potential Slow-Release Agents of Nitric Oxide *in Vivo*. *J. Chem. Soc. Perkin Trans. 1* **1994**, 797–805.

(28) Hart, T. W. Some Observations Concerning the *S*-Nitroso and *S*-Phenylsulphonyl Derivatives of L-Cysteine and Glutathione. *Tetrahedron Lett.* **1985**, *26* (16), 2013–2016.

(29) Parent, M.; Dahboul, F.; Schneider, R.; Clarot, I.; Maincent, P.; Leroy, P.; Boudier, A. A Complete Physicochemical Identity Card of *S*-Nitrosoglutathione. *Curr. Pharm. Anal.* **2013**, *9*, 31–42.

(30) TA Instruments. High Resolution Thermogravimetric Analysis - A New Technique for Obtaining Superior Analytical Results. *Therm. Anal. Rheol*. TA-023.

(31) Asquith, R. S.; Hirst, L. The Photochemical Degradation of Cystine in Aqueous Solution in the Presence of Air. *Biochim. Biophys. Acta* **1969**, *184*, 345–357.

(32) Wang, K.; Hou, Y.; Zhang, W.; Ksebati, M. B.; Xian, M.; Cheng, J. P.; Wang, P. G. 15N NMR and Electronic Properties of *S*-Nitrosothiols. *Bioorganic Med. Chem. Lett.* **1999**, *9* (19), 2897–2902.

(33) Hornyk, I.; Marosi, K.; Kiss, L.; Gróf, P.; Lacza, Z. Increased Stability of *S*-Nitrosothiol Solutions via PH Modulations. *Free Radic. Res.* **2012**, *46* (2), 214–225.

(34) de Souza, G. F. P.; Denadai, J. P.; Picheth, G. F.; de Oliveira, M. G. Long-Term Decomposition of Aqueous *S*-Nitrosoglutathione and *S*-Nitroso-*N*-Acetylcysteine: Influence of Concentration, Temperature, PH and Light. *Nitric Oxide* **2019**, *84* (October 2018), 30–37.

(35) Williams, D. L. H. The Mechanism of Nitric Oxide Formation from *S*-Nitrosothiols (Thionitrites). *Chem. Commun.* **1996**, *No. 10*, 1085–1091.

(36) Wo, Y.; Li, Z.; Brisbois, E. J.; Colletta, A.; Wu, J.; Major, T. C.; Xi, C.; Bartlett, R. H.; Matzger, A. J.; Meyerhoff, M. E. Origin of Long-Term Storage Stability and Nitric Oxide Release Behavior of CarboSil Polymer Doped with *S*-Nitroso-*N*-Acetyl-D-Penicillamine. *ACS Appl. Mater. Interfaces* **2015**, *7* (40), 22218–22227.

(37) Canneva, A.; Erben, M. F.; Romano, R. M.; Vishnevskiy, Y. V.; Reuter, C. G.; Mitzel, N. W.; Della Védova, C. O. The Structure and Conformation of $(CH_3)_3CSNO$. *Chem. - A Eur. J.* **2015**, *21* (29), 10436–10442.

(38) Meyer, B.; Genoni, A.; Boudier, A.; Leroy, P.; Ruiz-Lopez, M. F. Structure and Stability Studies of Pharmacologically Relevant *S*-Nitrosothiols: A Theoretical Approach. *J. Phys. Chem. A* **2016**, *120* (24), 4191–4200.

(39) Yi, J.; Khan, M. A.; Lee, J.; Richter-Addo, G. B. The Solid-State Molecular Structure of the *S*-Nitroso Derivative of L-Cysteine Ethyl Ester Hydrochloride. *Nitric Oxide* **2005**, *12* (4), 261–266.

(40) Bio-Rad Laboratories. Chelex 100 and Chelex 20 Chelating Ion Exchange Resin Instruction Manual.

(41) Inglis, A. S.; Nicholls, P. W.; Roxburgh, C. M. Hydrolysis of the Peptide Bond and Amino Acid Modification with Hydriodic Acid. *Austrailian J. Biol. Sci.* **1971**, *24*, 1235–1240.

(42) Grossi, L.; Montevecchi, P. C. A Kinetic Study of *S*-Nitrosothiol Decomposition. *Chem. - A Eur. J.* **2002**, *8* (2), 380–387.

(43) Grossi, L.; Montevecchi, P. C.; Strazzari, S. Decomposition of *S*-Nitrosothiols: Unimolecular versus Autocatalytic Mechanism. *J. Am. Chem. Soc.* **2001**, *123* (20), 4853–4854.

(44) Markovits, G. Y.; Schwartz, S. E.; Newman, L. Hydrolysis Equilibrium of Dinitrogen Trioxide in Dilute Acid Solution. *Inorg. Chem.* **1981**, *20* (2), 445–450.

(45) da Silva, G.; Kennedy, E. M.; Dlugogorski, B. Z. Ab Initio Procedure for Aqueous-Phase PKa Calculation: The Acidity of Nitrous Acid. *J. Phys. Chem. A* **2006**, *110* (39), 11371–11376.

(46) Sexton, D. J.; Muruganandam, A.; McKenny, D. J.; Mutus, B. Visible Light Photochemical Release of Nitric Oxide from *S*-Nitrosoglutathione: Potential Photochemotherapeutic Applications. *Photochem. Photobiol.* **1994**, *59* (4), 463–497.

CHAPTER 3

CATALYTIC COPPER-BASED MATERIALS FOR NITRIC OXIDE GENERATION FROM *S*-NITROSOGLUTATHIONE: CHEMICAL AND PRACTICAL ADVANTAGES OF EMBEDDING A COPPER METAL–ORGANIC FRAMEWORK INTO A POLYMER SCAFFOLD

3.1 Overview

Previous research discovered that a water stable copper-based metal–organic framework (MOF) CuBTTri (Cu(II) benzene-1,3,5-tris(1*H*-1,2,3-triazoy-5-yl)) is a promising catalyst for the development of anti-fouling materials via localized nitric oxide (NO) generation from endogenous *S*-nitrosothiols. A significant challenge of using MOFs for this purpose is that these solid-state materials must be immobilized in a flexible, processable scaffold for coating devices. Embedding a MOF within a polymer is an effective, accessible option; however, it is currently unknown how the presence of the polymer will impact the level of observed NO generation catalyzed by the embedded CuBTTri particles. This chapter explores the research question: How is CuBTTri-catalyzed NO generation impacted by incorporation into a polymer composite?

3.2 Introduction

Metal-organic frameworks (MOFs) are solid-state, crystalline, porous materials which offer special opportunities use as heterogeneous catalysts due to their tunability, straightforward synthetic methods, and well-defined structures.[1,2] MOF catalysts have attracted attention for applications in medicine, energy, and synthesis. Our group has extensively studied the Cu-based MOF CuBTTri (Cu(II) 1,3,5-Benzene-tris-triazole, Figure 3.1) for the fabrication of NO-generating medical device materials.[3-6] NO is a promising candidate for preventing or reducing

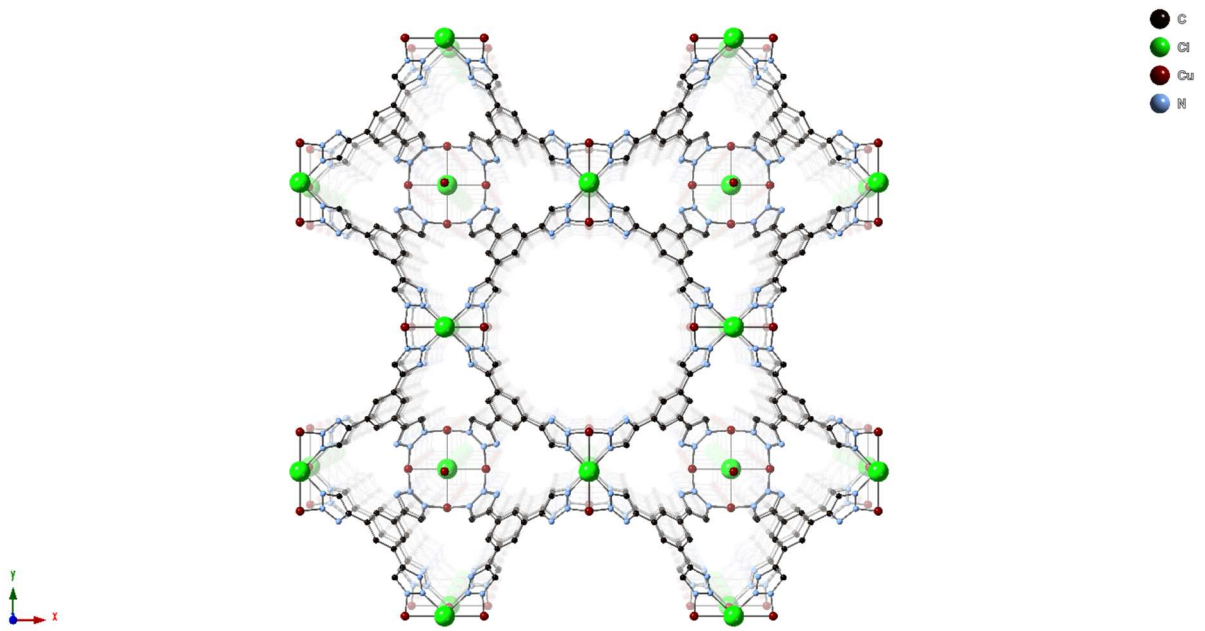

Figure 3.1. Cu(II) 1,3,5-Benzene-tris-triazole (CuBTTri) crystal structure.

biofouling because of its biological role in antithrombotic and antibacterial processes[7,8] CuBTTri is a 3-dimensional, azolate-based MOF with unsaturated Cu(II) centers known to catalytically oxidize the endogenous tripeptide *S*-nitrosoglutathione (GSNO) in the presence of the corresponding thiol (GSH) to generate NO.[9] CuBTTri is well-suited for this biomedical application because it is stable under physiological conditions and compatible with human liver cells.[6] And, importantly, CuBTTri is capable of generating NO from biologically-relevant concentrations of GSNO without leaching Cu^{2+} cations or undergoing framework decomposition. However, the experimental mechanistic studies in which MOF catalyst performance is measured are carried out on MOF *powders*, and in many industry applications, the MOF will have to be dispersed in a continuous phase (for example, a polymer).[10] It is currently unknown, in general, how dispersing MOFs in a continuous phase will impact their catalytic performance for a given reaction. Herein, we tested how CuBTTri powder versus a CuBTTri/polymer composite compare

in terms of performance for GSNO to NO conversion catalysis and examined if the basic experimental rate law was changed.

3.3 Materials and Methods

3.3.1 Materials

L-Glutathione reduced (GSH; ≥98%) was purchased from Sigma-Aldrich (Saint Louis, MO). Azidotrimethylsilane (94%), sodium nitrite (99.999%), 1,3,5-triethynylbenzene (98%), copper(I) iodide (98%), and copper(II) chloride dihydrate (99+%) were purchased from Alfa Aesar (Ward Hill, MA). Tecophilic™ SP-80A-150 thermoplastic polyurethane was purchased from Lubrizol (Wickliffe, Ohio). Ultra-high purity nitrogen, medical grade oxygen, and nitric oxide balance nitrogen (43.6 ppm NO) gases were purchased from Airgas (Denver, CO). Millipore Milli-Q IQ Water Purification System from EMD Millipore (Billerica, MA) supplied ultrapure water.

3.3.2 S-*Nitrosoglutathione (GSNO) Synthesis*

GSNO was synthesized according to a previously reported method by Hart.[11] In a typical synthesis, cold GSH (5 mmol) and 2 M HCl (2.5 mL) were added to a round bottom flask suspended in an ice bath containing ultrapure water (8 mL) and with constant stirring for 10 min. Sodium nitrite (5 mmol) was added to the flask and stirred for 40 min. Acetone (20 mL) was added to the flask and stirred for 10 minutes which produced a pink/red precipitate. The precipitate was washed with cold ultrapure water (3 × 30 mL) and acetone (3 × 30 mL) and dried under vacuum. GSNO was stored at −20 °C shielded from light. ^{1}H NMR (400 MHz, D_2O): 4.68-4.61(dd, 1H, J = 7.14, 5.44 Hz), 4.15-4.02 (br m, 2H), 3.96 (s, 2H), 3.94 (t, 1H, J = 6.59 Hz), 2.46 (t, 2H, J = 7.56 Hz), 2.14 (q, 2H, J = 7.17 Hz).[12]

*3.3.3 Cu(II) Benzene-1,3,5-tris(1*H*-1,2,3-triazoy-5-yl) (CuBTTri) Synthesis*

CuBTTri was synthesized by an adapted version of a previously reported method by Demessence et al.[13] The ligand H_3BTTri (1,3,5-tris(1*H*-1,2,3-triazol-5-yl)benzene) was synthesized by adding azidotrimethylsilane (9.16 g) to a solution containing DMF (90 mL), methanol (10 mL), copper(I) iodide (0.505 g), and 1,3,5-triethynylbenzene (2.65 g) under a nitrogen atmosphere. The solution was stirred for 36 h at 100 °C then filtered, condensed to approximately 10 mL, and combined with 30 mL ultrapure water to produce a precipitate. The precipitate H_3BTTri was washed with diethyl ether and ultrapure water. CuBTTri was synthesized by adding H_3BTTri (0.225 g) and $CuCl_2$ (0.383 g) to DMF (40 mL) and heating for 72 h at 100 °C. The resulting CuBTTri was collected via filtration and washed with DMF and ultrapure water. The powder was added to ultrapure water and heated for 24 h at 100 °C. CuBTTri was collected via filtration and washed with ultrapure water, and the washing process repeated two more times. The resulting CuBTTri was characterized using attenuated total reflectance Fourier transform infrared spectroscopy (ATR-FTIR; Thermo Fisher Scientific Nicolet iS50 FTIR spectrometer with an ATR accessory, Madison, WI; Figure 3.2), powder X-ray diffraction (PXRD; 5-50 2θ, CuKα radiation, Bruker D8 Discovery DaVinci, Billerica, MA; Figure 3.3) and scanning electron microscopy (SEM; 20 nm gold, 15 kV accelerating voltage, JEOL 6500 Field Emission SEM, Peabody, MA, Figures 3.4 and 3.5).

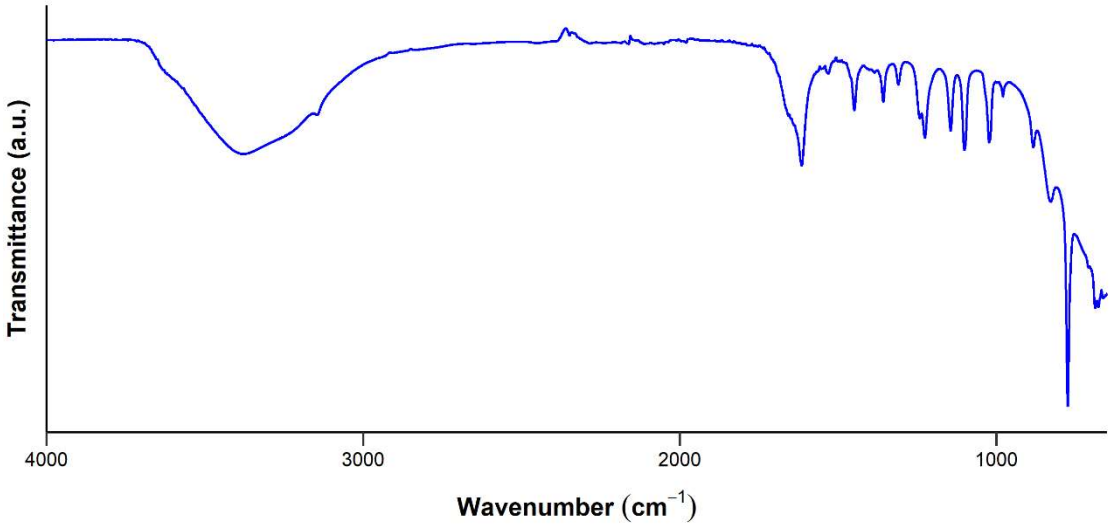

Figure 3.2. ATR-FTIR of CuBTTri powder.

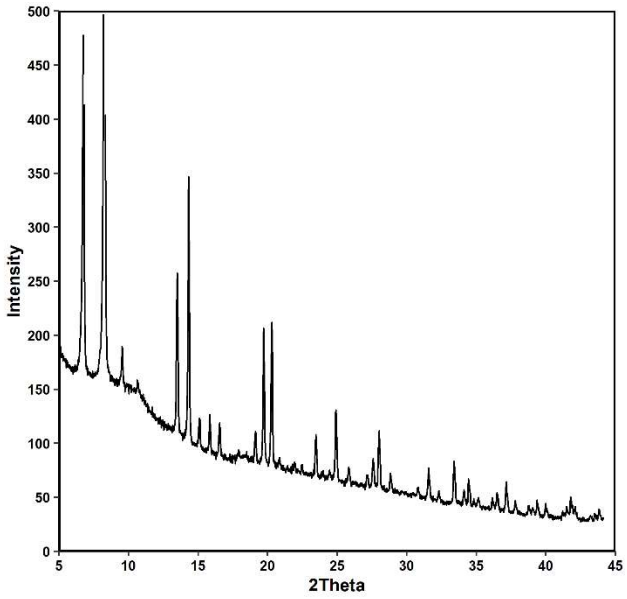

Figure 3.3. PXRD of CuBTTri powder (sloping baseline due to residual adsorbed water).

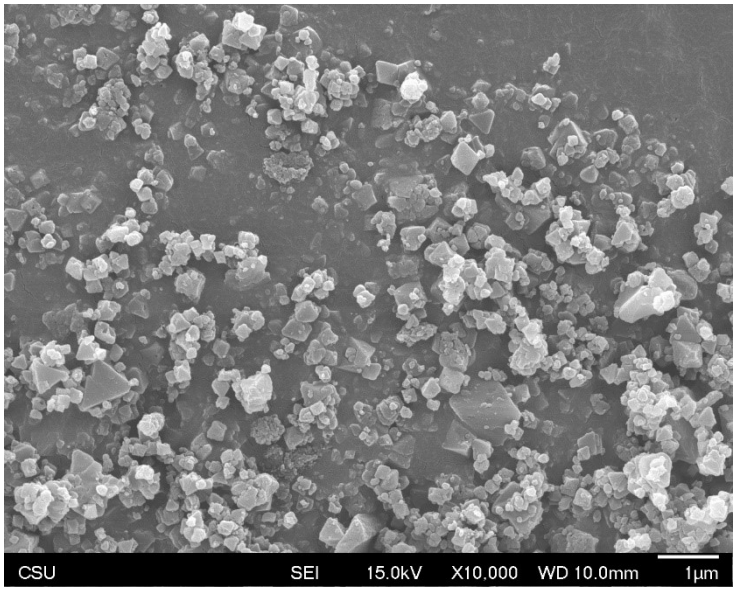

Figure 3.4. SEM image (15 kV, 10,000X) of CuBTTri powder (0.3 ± 0.1 µm, n = 150).

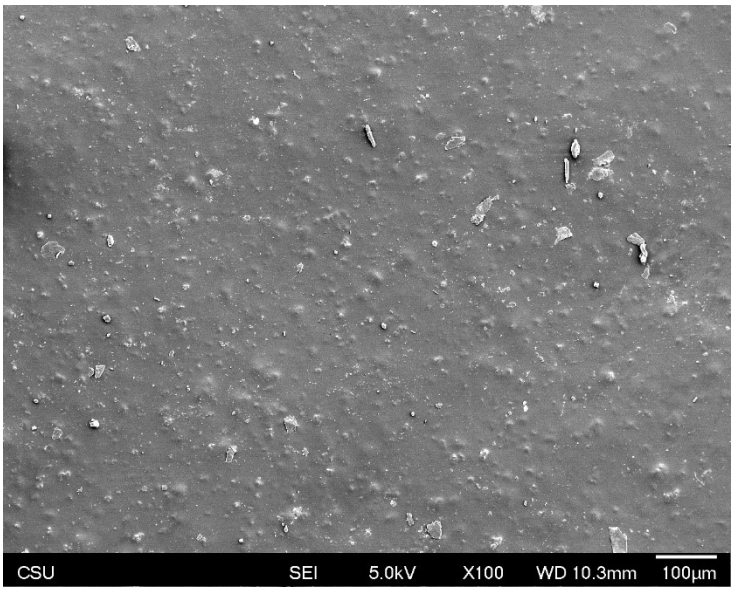

Figure 3.5 SEM image (15 kV, 100X) of CuBTTri/polyurethane composite material.

3.3.4 Composite Material Fabrication

SP-80A-150 polyurethane (0.3 g) was dissolved in THF (7 mL) overnight. Synthesized CuBTTri was hand ground for 5 minutes to produce a fine powder. CuBTTri (15 mg) was added to a 20 mL vial with THF (3 mL) and stirred rapidly for at least 1 h until no visible agglomerations remained. The CuBTTri solution was added to the polyurethane solution and stirred for 15 minutes to fully combine. The solution was poured into a 4.8 cm diameter polytetrafluorethylene (PTFE) mold and covered with a glass cover to slow evaporation to produce a 5 wt.% CuBTTri/3 w/v% polyurethane composite material. After fully evaporated, the 4.8 cm film was punched into 1.2 cm diameter films for analysis.

3.3.5 Nitric Oxide Generation Measurements

NO generation was monitored using NO-selective chemiluminescence-based detection (Nitric Oxide Analyzers, NOA 280i, Zysense, Weddington, NC) at 25 °C in ultrapure water with constant nitrogen bubbling and shielded from light exposure. For CuBTTri powder experiments, CuBTTri (0.9-1.0 mg) was added to a 20 mL vial with ultrapure water (2 mL) and stirred rapidly for at least one hour to replicate composite material fabrication then added to a reaction cell. For CuBTTri composite film experiments, a 1.2 cm diameter film was added to a reaction cell and soaked in ultrapure water for exactly 5 minutes. The reaction cell was injected with a small volume of 1 mM GSNO (and a small volume of 1 mM GSH, for certain experiments) to make a final concentration of 10 μM GSNO (10 μM GSH) with a final volume of 3 mL. Data was collected at 1 s.

3.3.6 Data Reporting and Analysis

Reaction time was measured from GSNO injection until NO release returned to baseline levels (<1 ppb) or after 3 h. NO yield was calculated by converting NO (ppb) to NO (moles)

using an instrument-specific calibration constant (mol ppb^{-1} s^{-1}). This value was divided by the number of moles NO added to the reaction from GSNO and multiplied by 100. Data reported as mean ± standard deviation (SD) of n = 3 replicates.

3.4 Results and Discussion

Our group has recently studied how CuBTTri *powder* catalyzes GSNO to NO conversion from a fundamental, mechanistic perspective.[5,9,14] There are two select findings from this prior work relevant to the current study. First, GSNO oxidation occurs exclusively at exterior surface copper centers, therefore any diffusion limitations observed for the CuBTTri/polymer composite can be attributed to GSNO diffusion into the polymer and *not* into the CuBTTri pores. Second, the reaction is 1st order in [GSH], and GSH must be added to the reaction to observe significant GSNO to NO conversion catalyzed by CuBTTri powder (e.g., in 16 h 10% versus 100% GSNO oxidation is observed without and with added GSH, respectively). Based on these preliminary findings, our initial hypothesis was that NO generation from the CuBTTri dispersed in a polymer would be *slower* than NO generation from the CuBTTri powder due to the rate of GSNO diffusion first into the film and then to the catalytically-active Cu sites. Additionally, we hypothesized that at least some of the catalytically active sites in CuBTTri might be rendered inaccessible from polymer encapsulation.

To test this hypothesis, MOF-embedded films were fabricated by dispersing CuBTTri particles (0.3 ± 0.1 μm diameter) in a hydrophilic medical grade polyurethane (Lubrizol Tecophilic SP-80A-150). The polymer was selected for its ability to absorb water up to 150% its weight based on previous research indicating that water absorptivity is necessary to facilitate the interaction between polymer-embedded CuBTTri and GSNO in solution.[15] For direct comparisons between the powder and composite systems, the studies were conducted with a 5 wt.% CuBTTri/3 w/v% polyurethane composite material and an equivalent mass of CuBTTri

powder present in one 1.2 cm diameter composite film (0.9-1.0 mg CuBTTri). It is worth noting that in our experiments the system is flooded with an excess of CuBTTri relative to the biologically-relevant GSNO concentration selected to simulate the medical application of these materials. This also means that the observed NO generation kinetics are not limited by catalyst availability in comparison to our previous work studying the CuBTTri powder that was carried out with the number of active Cu sites at catalytic/sub-stoichiometric levels.

Surprisingly, we observed that the rate of NO generation from the composite film *significantly exceeded* that of the CuBTTri powder alone in experiments with no added GSH (Figure 3.6), disproving our original hypothesis. In 3 h, based on the amount of NO recovered, the reaction with CuBTTri powder was only 30% complete, whereas the composite film yielded full recovery of NO in 2.0 ± 0.1 h (Table 3.1). The CuBTTri powder result was not surprising given that kinetic studies conducted by our group on an aqueous system containing 2.0 mM GSNO and 2.7 mg CuBTTri resulted in just 10% loss of GSNO over 16 h. The increased rate of NO generation observed herein for the CuBTTri powder versus prior work is explained by the greater mass of MOF in the reaction and small CuBTTri particle size from the combination of hand grinding and rapid stirring. The improved rate of NO generation for the composite was counter to our original hypothesis, where we expected the polymer matrix to slow the reaction either by blocking access to some number of the CuBTTri active sites or by diffusion limitations.

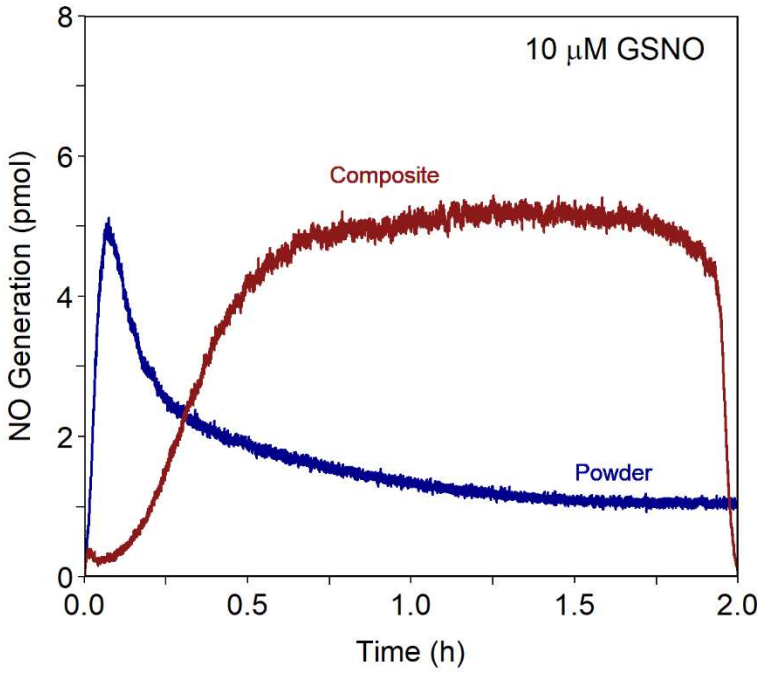

Figure 3.6. Representative NO generation profiles for CuBTTri powder versus composite catalyzed NO generation with no added GSH. The composite outperforms the powder in terms of total NO generated in 2 h. Additionally, the powder results are in good agreement with our previous reports where the powder alone is a poor NO generation catalyst. While the powder initially generates NO at a greater rate than the composite, it falls off quickly (~15 min) and is overtaken by the composite, which sustains a higher rate of NO generation for ~1.5 h. Added GSH is *not necessary* to observe complete NO recovery for the composite in 2 h. The shapes of the two profiles are different, which indicates that there may be a different limiting step for each material (we hypothesize that the composite reaction is limited by diffusion of GSNO/GSH into the polymer). Experimental conditions: 25 °C, shielded from light, N_2 bubbling in ultrapure water.

Another interesting feature of the data in Figure 3.6 is the difference in the shape of the NO generation curves for the CuBTTri powder and composite. The powder NO generation appears overall 1st order, which is in good agreement with previous findings on the powder systems showing that the reaction is 1st order in GSNO. However, the composite NO generation appears overall 0th order, and we propose that the turnover limiting step for the composite material with no GSH added is GSNO diffusion first into the polymer matrix and then to the

CuBTTri particles/active sites. Additionally, the initial rate of NO generation for the powder is higher than for the composite, but eventually the composite reaches a greater steady state NO flux than the powder, which results in significantly greater NO release. Our hypothesis to explain this phenomenon is shown in Figure 3.7. Briefly stated, our hypothesis is that due to the concentration gradient present (at t = 0, there is no GSNO present in the polymer while [GSNO] = 10 μM in solution) GSNO diffuses into the polymer and then reaches CuBTTri particles. The initial GSNO diffusion is represented by the first portion of the composite trace in Figure 2, where the rate of NO generation is increasing. Once a more equal concentration gradient has been reached, the rate of NO generation remains relatively constant, as the GSNO oxidized by the dispersed CuBTTri particles is replaced by fresh equivalents of GSNO that are effectively "trapped" within the polymer. We hypothesized that the rate of NO generation for the composite is slower than the powder because the [GSH] present in the system is so low (the only GSH present is a leftover impurity from the GSNO synthesis) that the rate of GSH diffusion into the polymer is slow because the concentration gradient is much lower than for that of GSNO. This reasoning is based upon the hypothesis that the composite and powder CuBTTri catalysts operate for GSNO to NO conversion by the same mechanism, and that GSH is necessary for both catalysts. We tested this hypothesis with our next set of experiments.

We added stoichiometric levels of GSH to the reaction system based on the previous work showing that CuBTTri powder catalyzed GSNO to NO conversion is 1st order in [GSH]. We found that the addition of 10 mM GSH to the CuBTTri powder system significantly increased the amount of NO generated within 2 h, and complete NO recovery was achieved over 1.4 ± 0.2 h (Figure 3). The rate of NO generation by the CuBTTri-polymer composite material increased by *at least* 5-fold upon the addition of GSH, and complete NO recovery was achieved

in ~20 min. With added GSH, NO generation by the composite material remained significantly faster than the CuBTTri powder, completing the reaction in one-quarter of the time. Additionally, the NO generation profile for the composite material transitioned from a diffusion-limited, apparent 0^{th} order reaction to an apparent 1^{st} order reaction with the addition of GSH, while the CuBTTri powder NO generation profile remained a 1^{st} order process regardless of GSH concentration. These results support our hypothesis that GSH is acting in an identical fashion for both the composite and powder catalysts, and that both materials catalyze GSNO to NO conversion by an identical mechanism.

Figure 3.7. Diagram illustrating our hypothesis explaining why the composite outperforms the powder with no added GSH. The composite may be initially slower because there is such low [GSH] in Figure 1 data that the rate of diffusion of GSH into the composite is slow compared to GSNO because of the lower concentration gradient. Alternatively, GSNO may be slowly converted into GSH inside the composite thereby turning on the reaction. The fast diffusion of GSNO into the polymer is driven by the high concentration gradient between the solution and the film, and a diffusion-controlled reaction is supported by the shape of the composite curve in Fig. 3.6. The rate of NO generation for the composite without added GSH reaches a steady-state flux for ~1.5 h, which indicates that the overall process is 0^{th} order (i.e., the rate does not change as product is generated/substrate is consumed). We propose that the mechanism of GSNO to NO conversion is the same for both composite and powder in Fig. 3.6, but the slow step for the composite system is GSH diffusion/GSH generation while for the powder it is a step within the catalytic cycle (i.e., an elementary step/chemical reaction).

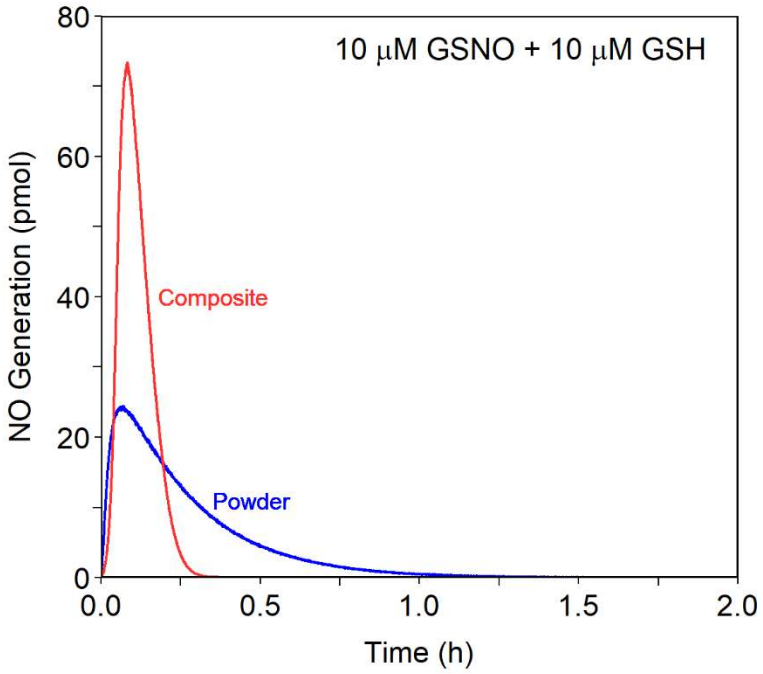

Figure 3.8. Representative NO generation profiles for CuBTTri powder versus composite catalyzed NO generation with added GSH. The composite outperforms the powder again, and the rate of NO generation increases for both materials with added GSH. This finding is in good agreement\ with our previously reported results that the reaction is 1st order in [GSH]. The NO generation profile has changed for the composite from apparent 0th order in Figure 2 to apparent 1st order here. We hypothesize that the composite now outperforms the powder because it is no longer limited by GSH diffusion into the composite. These data support our prior hypothesis that delivering GSH into the polymer, either by diffusion or generation, was the limiting step for the composite data in Fig. 3.6. However, the composite appears to still retain the advantage of "trapping" GSNO near the catalytically active MOF particles for NO release followed by the "shuttling in" of the next GSNO equivalent. These data further support that both materials operate by the same reaction mechanism, but the composite carries the advantage of the confinement effects on GSNO. Experimental conditions: 25 °C, shielded from light, N_2 bubbling in ultrapure water.

Table 3.1. Summary of results from Figures 3.6 and 3.8.

CuBTTri Composition[a]	[GSH] (μM)	Reaction Time[d] (h)	NO Yield (%)
Powder[b]	0	3.0[e]	30 ± 10
	10.0	1.4 ± 0.2	93 ± 6
Composite[c]	0	2.0 ± 0.1	97 ± 6
	10.0	0.35 ± 0.04	97 ± 3

[a]CuBTTri hand ground and stirred rapidly for 1 h or until fully suspended in solvent.
[b]CuBTTri powder added to reaction cell at 0.9-1.0 mg.
[c]Composite film swelled with water for exactly 5 min prior to NOA experiment.
[d]Data reported as mean ± SD (n = 3).
[e]Experiment stopped after NO release returned to baseline or after 3.0 h.

3.5 Conclusions

Taken together, this work has broad implications for the industrial or commercial implementation of catalytic MOFs, as most applications require immobilizing the powder MOF in a processable scaffold to be incorporated into a device or system. Dispersing the MOF in a polymer matrix is a convenient, versatile, and cost-effective method in which various parameters (e.g., polymer identity, polymer concentration, MOF loading) can be readily tuned for a particular application. The findings in this work indicate that the behavior and performance of a catalytic MOF can change when embedded in a polymer matrix, so direct comparisons between the powder MOF and composite material should be conducted to quantify any impact on catalysis. But excitingly, this work has shown that MOF composite materials can have superior performance compared to the powder alone, in addition to the benefits gained from the versatility of the composite polymer. Dispersing CuBTTri in a polymer matrix *significantly improved* its catalytic performance for GSNO to NO conversion, showing that the MOF composite material

catalyzed the reaction faster than the powder MOF *with and without added GSH*. Adding a stoichiometric amount of GSH enhanced the rate of NO generation for both compositions and altered the observed kinetics of the composite material. This work highlights that there are beneficial implications for medical devices achieved by embedding CuBTTri in a polymer.

CHAPTER 3

REFERENCES

(1) Kang, Y. S.; Lu, Y.; Chen, K.; Zhao, Y.; Wang, P.; Sun, W. Y. Metal–Organic Frameworks with Catalytic Centers: From Synthesis to Catalytic Application. *Coord. Chem. Rev.* **2019**, *378*, 262–280.

(2) Jiao, L.; Wang, Y.; Jiang, H. L.; Xu, Q. Metal–Organic Frameworks as Platforms for Catalytic Applications. *Advanced Materials.* **2018**, *30*, 1703663.

(3) Zang, Y.; Roberts, T. R.; Batchinsky, A. I.; Reynolds, M. M. Metal-Organic Framework Polymer Coating Inhibits Staphylococcus Aureus Attachment on Medical Circulation Tubing under Static and Dynamic Flow Conditions. *ACS Appl. Bio Mater.* **2020**, *3* (6), 3535–3543.

(4) Harding, J. L.; Metz, J. M.; Reynolds, M. M. A Tunable, Stable, and Bioactive MOF Catalyst for Generating a Localized Therapeutic from Endogenous Sources. *Adv. Funct. Mater.* **2014**, *24* (47), 7503–7509.

(5) Tuttle, R. R.; Daly, R. E.; Rithner, C. D.; Reynolds, M. M. Monitoring a MOF Catalyzed Reaction Directly in Blood Plasma. *ACS Appl. Mater. Interfaces* **2021**, *13* (44), 52006–52013.

(6) Neufeld, M. J.; Ware, B. R.; Lutzke, A.; Khetani, S. R.; Reynolds, M. M. Water-Stable Metal-Organic Framework/Polymer Composites Compatible with Human Hepatocytes. *ACS Appl. Mater. Interfaces* **2016**, *8* (30), 19343–19352.

(7) Bogdan, C. Nitric Oxide and the Immune Response. *Nat. Immunol.* **2001**, *2* (10), 907–916.

(8) Moncada, S.; Higgs, E. A. The Discovery of Nitric Oxide and Its Role in Vascular *Biology. Br. J. Pharmacol.* **2006**, *147*, S193–S201.

(9) Tuttle, R. R.; Rubin, H. N.; Rithner, C. D.; Finke, R. G.; Reynolds, M. M. Copper Ion vs Copper Metal–Organic Framework Catalyzed NO Release from Bioavailable S-Nitrosoglutathione En Route to Biomedical Applications: Direct 1H NMR Monitoring in Water Allowing Identification of the Distinct, True Reaction Stoichiometries and Thio. *J. Inorg. Biochem.* **2019**, *199* (July), 110760.

(10) Kalaj, M.; Bentz, K. C.; Ayala, S.; Palomba, J. M.; Barcus, K. S.; Katayama, Y.; Cohen, S. M. MOF-Polymer Hybrid Materials: From Simple Composites to Tailored Architectures. *Chem. Rev.* **2020**, *120* (16), 8267–8302.

(11) Hart, T. W. SOME OBSERVATIONS CONCERNING THE S-NITROSO AND S-PHENYLSULPHONYL DERIVATIVES OF L-CYSTEINE AND GLUTATHIONE. *Tetrahedron Lett.* **1985**, *26* (16), 2013–2016.

(12) Parent, M.; Dahboul, F.; Schneider, R.; Clarot, I.; Maincent, P.; Leroy, P.; Boudier, A. A Complete Physicochemical Identity Card of S-Nitrosoglutathione. *Curr. Pharm. Anal.* **2013**, *9*, 31–42.

(13) Demessence, A.; Alessandro, D. M. D.; Foo, M. L.; Long, J. R. Strong CO2 Binding in a Water-Stable, Triazolate-Bridged Metal−Organic Framework Functionalized with Ethylenediamine. *J. Am. Chem. Soc.* **2009**, *131* (25), 8784–8786.

(14) Tuttle, R. R.; Folkman, S. J.; Rubin, H. N.; Finke, R. G.; Reynolds, M. M. Copper Metal-Organic Framework Surface Catalysis: Catalyst Poisoning, IR Spectroscopic, and Kinetic Evidence Addressing the Nature and Number of the Catalytically Active Sites En Route to Improved Applications. *ACS Appl. Mater. Interfaces* **2020**, *12* (35), 39043–39055.

(15) Neufeld, M. J.; Lutzke, A.; Jones, W. M.; Reynolds, M. M. Nitric Oxide Generation from Endogenous Substrates Using Metal-Organic Frameworks: Inclusion within Poly(Vinyl Alcohol) Membranes to Investigate Reactivity and Therapeutic Potential. *ACS Appl. Mater. Interfaces* **2017**, *9* (41), 35628–35641.

CHAPTER 4

SYSTEMATIC EXPLORATION OF COPPER(II) BENZENE-1,3,5-TRIS(1*H*-*1*,2,3-TRIAZOY-5-YL)/POLYURETHANE COMPOSITE PARAMETERS FOR NITRIC OXIDE-GENERATING MEDICAL DEVICE COATINGS[2]

4.1 Overview

In Chapter 3, it was discovered that embedding the metal–organic framework (MOF) CuBTTri (Cu(II) benzene-1,3,5-tris(1*H*-1,2,3-triazoy-5-yl)) *enhances* the rate of NO generation from biologically-relevant concentrations of *S*-nitrosoglutathione (GSNO) compared to the MOF powder alone. In this chapter, three key parameters of composite materials—MOF preparation/particle size, MOF loading, and polymer concentration—are evaluated using composite films comprised of CuBTTri and the medical-grade hydrophilic polyurethane, Tecophilic SP-80A-150. This chapter explores the research questions: 1) How tunable are catalytic MOF composite materials? 2) How do MOF particle size, MOF loading, and polymer concentration impact GSNO to NO catalysis for these composite materials? 3) What is the optimal MOF/polymer formulation to be applied as the outer semipermeable membrane on a blood-contacting glucose biosensor?

4.2 Introduction

Metal–organic frameworks (MOFs) are crystalline coordination polymers consisting of metal centers connected by organic linkers.[1] The tunable, highly ordered, and porous nature of these materials makes them favorable for a variety of applications from gas storage to catalysis.[2-

[2] This chapter was reproduced in part from:
Melvin, A.C.; Reynolds M.M. Systematic Exploration of a Catalytic Metal-Organic Framework (MOF)/Polyurethane Composite for Medical Device Applications: Effects of MOF Particle Size, MOF Loading, and Polymer Concentration on Composite Material Activity. *Front. Phys.* **2022**, *10* (880841), 1-9. https://doi.org/10.3389/fphy.2022.880841.

[8] MOFs have been employed as heterogeneous catalysts extensively in recent years due to their distinctive physical properties including rational design/tunability, structural diversity, and coordinatively unsaturated metal sites.[6]

As MOF applications continue to expand, hybrid MOF/polymer composite materials (also referred to as mixed-matrix membranes, MMMs) have attracted attention as an effective way to incorporate the solid-state material on devices for commercial or industrial applications by merging the functionalities of MOFs with the flexibility and processability of polymers.[9-12] Various synthetic methods such as polymer grafting to or from MOFs, polymerizing within MOFs, and polymer templating MOFs have been employed to fabricate these hybrid materials; though the most widely-used conventional method involves dispersing solid MOF particles in a polymer solution.[12-17] This method is attractive for its relative ease, accessibility, and tunability, and has been demonstrated for a range of MOF and polymer combinations.[13,18-20] But poor interactions between the two phases can result in agglomerations of MOF particles during the fabrication or evaporation process.[13] Reducing MOF particle size, altering MOF particle morphology, priming the MOF particles with the polymer solution, and slowing the evaporation rate of the solvent are a few strategies to improve the uniformity of these films. For catalytic MOFs, composites provide the benefit of increased catalyst stability and recoverability, but must retain its desired catalytic properties.[9,18,21] Compared to the powder MOF system, the catalytic performance of the polymer-embedded systems has been shown to range from moderately reduced[22] to sustained[18] to moderately enhanced.[23]

A water stable copper-azolate MOF CuBTTri, $H_3[(Cu_4Cl)_3(BTTri)_8]$ (H_3BTTri = 1,3,5-tris(1*H*-1,2,3-triazol-5-yl)benzene), maintains its crystallinity and catalytic activity for a desirable biomedical reaction after incorporation in polymers such as chitosan, poly(vinyl

alcohol), and CarboSil-2080A.[24-26] CuBTTri catalyzes the oxidation of bioavailable *S*-nitrosoglutathione (GSNO) to generate nitric oxide (NO), a critical biomolecule involved in range of physiological processes in the cardiovascular, immune, and nervous systems.[27-29] Designing CuBTTri/polymer composite materials for blood-contacting medical devices such as catheters, extracorporeal circuits, and sensors has been an active area of research because surface-localized generation of NO in the range of natural endothelial NO flux has been shown to prevent thrombus formation on artificial surfaces.[29-34] Herein, we incorporate CuBTTri into a hydrophilic polyurethane and evaluate the impacts of MOF particle size, MOF loading, and polymer concentration on NO generation to gain insights into the tunability of these composite materials for the design of biocompatible coatings. Ultimately, this work aims to advance the rational design of catalytic MOF composite materials for medical device applications.

4.3 Materials and Methods

4.3.1 Materials

Glutathione, reduced (GSH; 98%) was purchased from AMRESCO (Solon, OH). Sodium nitrite (99.999%), trimethylsilyl azide (94%), 1,3,5-triethynylbenzene (98%), copper(I) iodide (98%), and copper(II) chloride dihydrate (99+%) were purchased from Alfa Aesar (Ward Hill, MA). Tecophilic polyurethane (PU; SP-80A-150) was purchased from Lubrizol (Wickliffe, Ohio). All chemicals were used without further purification. Cell strainers (1 μm) were purchased from pluriSelect (Leipzig, Germany). Ultra-high purity (UHP) nitrogen (N_2), oxygen (O_2), and nitric oxide (NO, 43.6 ppm NO, balance N_2) gases were purchased from Airgas (Denver, CO). Ultrapure water (18.2 MΩ·cm) was supplied by a Millipore Milli-Q IQ water purification system (EMD Millipore, Billerica, MA).

4.3.2 S-*Nitrosoglutathione (GSNO) Synthesis*

Synthesis was adapted from a previously-reported method by Hart et al.[38] Briefly, cold glutathione (1.53 g, 5 mmol) was added to ultrapure water (18.2 MΩ·cm; 8 mL), 2 M hydrochloric acid (2.5 mL), and stirred for 10 minutes in an ice bath. Sodium nitrite (0.345 g, 5 mmol) was added to the solution and the reaction was allowed to proceed over ice for 40 minutes. The precipitate was filtered from the solution, rinsed with cold ultrapure water and acetone, and dried. Solid GSNO was stored at −20 °C and shielded from light. ^{1}H NMR (400 MHz, D_2O): 4.68-4.61(dd, 1H, J = 7.14, 5.44 Hz), 4.15-4.02 (br m, 2H), 3.96 (s, 2H), 3.94 (t, 1H, J = 6.59 Hz), 2.46 (t, 2H, J = 7.56 Hz), 2.14 (q, 2H, J = 7.17 Hz).[39]

*4.3.3 Cu(II) Benzene-1,3,5-tris(1*H*-1,2,3-triazoy-5-yl) (CuBTTri) Synthesis*

The ligand 1,3,5-tris(1*H*-1,2,3-triazol-5-yl)benzene (H_3BTTri) and MOF $H_3[(Cu_4Cl)_3(BTTri)_8{\cdot}(H_2O)_{12}]{\cdot}72H2O$ (CuBTTri) were synthesized by a simplified method previously reported by Demessence et al.[40] DMF (90 mL) and methanol (10 mL) were added to a flask containing copper(I) iodide (0.505 g, 2.60 mmol) and 1,3,5-triethynylbenzene (2.65 g, 17.6 mmol) and stirred under nitrogen. Trimethylsilyl azide (9.16 g, 79.5 mmol) was added to the flask and stirred at 100 °C for 36 h under nitrogen. The hot mixture was filtered. The filtrate was concentrated to approximately 10 mL then ultrapure water (≥30 mL) was added to produce a pale green precipitate. The solid was washed with ultrapure water and diethyl ether and dried under vacuum. H_3BTTri (0.225 g, 0.937 mmol) was dissolved in DMF (40 mL). Copper(II) chloride dihydrate (0.383 g, 2.25 mmol) was added to the solution then heated at 100 °C for 72 h. CuBTTri, the resulting purple precipitate, was filtered and washed with DMF and ultrapure water. Ultrapure water (≥15 mL) was added to a Pyrex bottle containing CuBTTri and heated at 100 °C for 24 h. The solid was filtered and washed with ultrapure water. The washing process

was repeated a total of 3 times.

4.3.4 CuBTTri Particle Preparation

CuBTTri powder was processed using three different methods prior to inclusion within a polymer to compare the effect of various preparation methods and MOF particle sizes (Fig. 4.1 for SEM images). A) Raw particles: CuBTTri solid used as prepared by the synthesis with no further treatment. B) Ground particles: CuBTTri samples were hand-ground for 5 minutes. C) Filtered particles: CuBTTri samples were first hand-ground as described above. Small amounts (1-5 mg) of the ground CuBTTri powder were suspended in ultrapure water (approx. 1 L) through a combination of rapid stirring and sonication. The solution was filtered through a 1 μm cell strainer and the water evaporated from the filtrate. The resulting CuBTTri powder was used to prepare the composites. Statistical evaluation determined that the three particle size ranges (n = 150 particles of each preparation method) were significantly different (raw vs. ground, $p = 1.4\times10^{-5}$; raw vs. filtered, $p = 1.3\times10^{-10}$; ground vs. filtered, $p = 2.7\times10^{-6}$).

4.3.5 Composite Material Fabrication

All CuBTTri samples were stirred rapidly (1200 rpm) in 3 mL THF in a 20 mL vial for at least 1 h, or until no CuBTTri clumps were visible (see Table 4.1 for composite preparation.) The polymer PU was dissolved in 7 mL THF overnight in a separate 20 mL vial. CuBTTri solution was added to PU solution and stirred for 15 min, or until visually homogenous. CuBTTri/PU solution was poured into a 4.8 cm diameter polytetrafluoroethylene (PTFE) mold. The PTFE mold was covered with glass cover and left to dry overnight. Films were dried for 15 min under vacuum then punched into 1.2 cm diameter films details for analysis (see Fig. 4.2 for images of the composites.)

Table 4.1. MOF Composites[a]

MOF Prep.	[MOF] (wt.%)	[PU][b] (w/v%)	MOF (g)	PU (g)	Water Uptake[c] (%)
Raw	5	3	0.0150	0.3000	131 ± 6
Filtered	5	3	0.0150	0.3000	118 ± 1
Ground	1	1	0.0010	0.1000	150 ± 40
Ground	1	3	0.0030	0.3000	116 ± 9
Ground	1	5	0.0050	0.5000	130 ± 10
Ground	5	1	0.0050	0.1000	151 ± 5
Ground	5	3	0.0150	0.3000	120 ± 10
Ground	5	5	0.0250	0.5000	114 ± 6
Ground	10	1	0.0100	0.1000	150 ± 10
Ground	10	3	0.0300	0.3000	113 ± 3
Ground	10	5	0.0500	0.5000	107 ± 3
--	0	3	--	0.3000	131 ± 4

[a]Composites prepared as 4.8 cm films punched into 1.2 cm diameter films (n = 3) for analysis.
[b]Film thickness = 44 ± 5 μm, 85 ± 2 μm, 120 ± 20 μm for 1, 3, and 5% PU, respectively.
[c]Data reported as mean ± SD (n = 3).

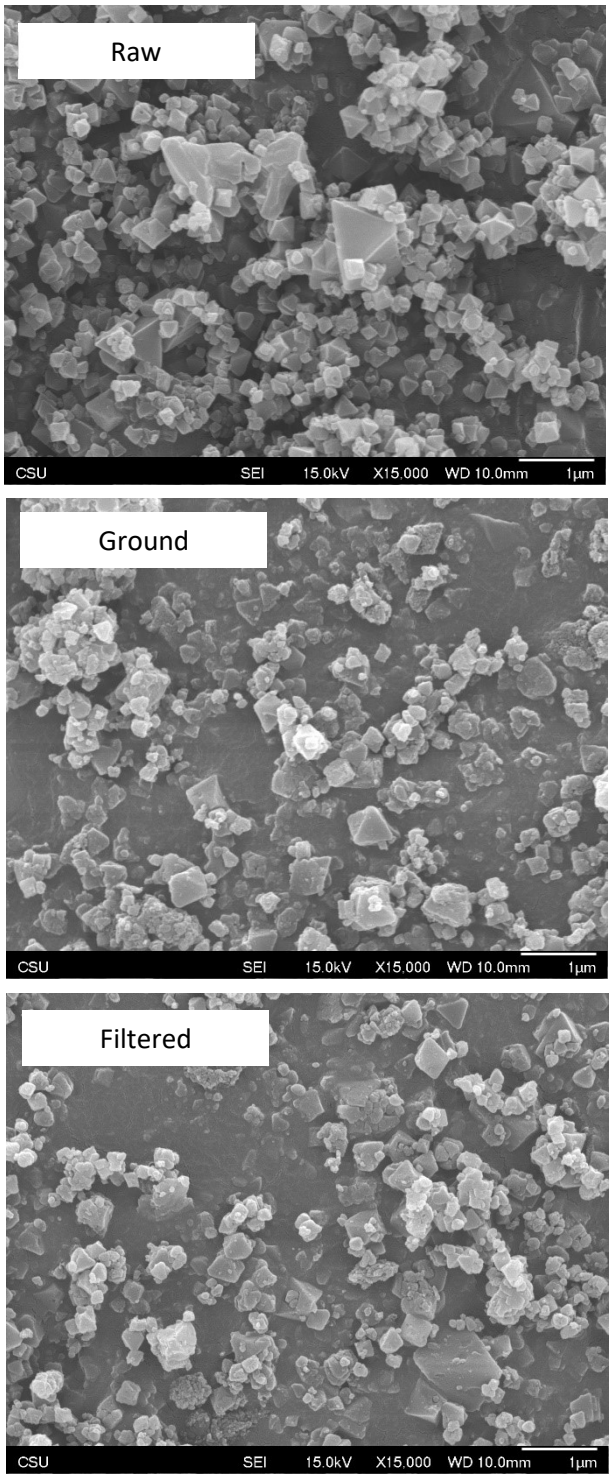

Figure 4.1. SEM images (15 kV, 15,000X) of MOF particles from three preparation methods. Top: raw, 0.4 ± 0.2 µm diameter; Middle: ground, 0.3 ± 0.1 µm; Bottom: filtered, 0.2 ± 0.1 µm diameter.

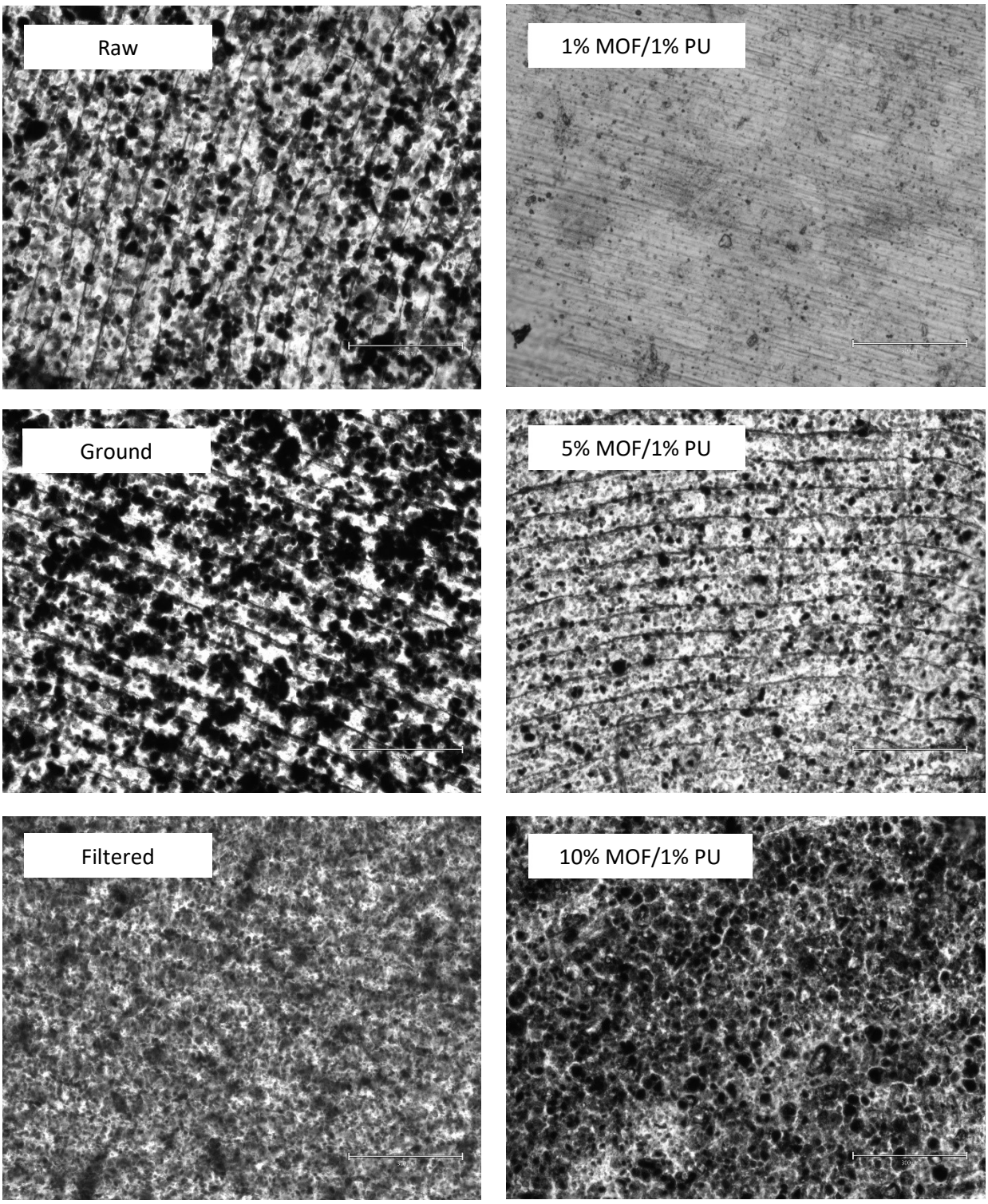

Figure 4.2A. Optical microscope images (10X) of MOF composites. Left: 5% MOF/3% PU films with different MOF processing methods. Right: 1% PU films at 1% (top), 5% (middle), and 10% (bottom) MOF loading.

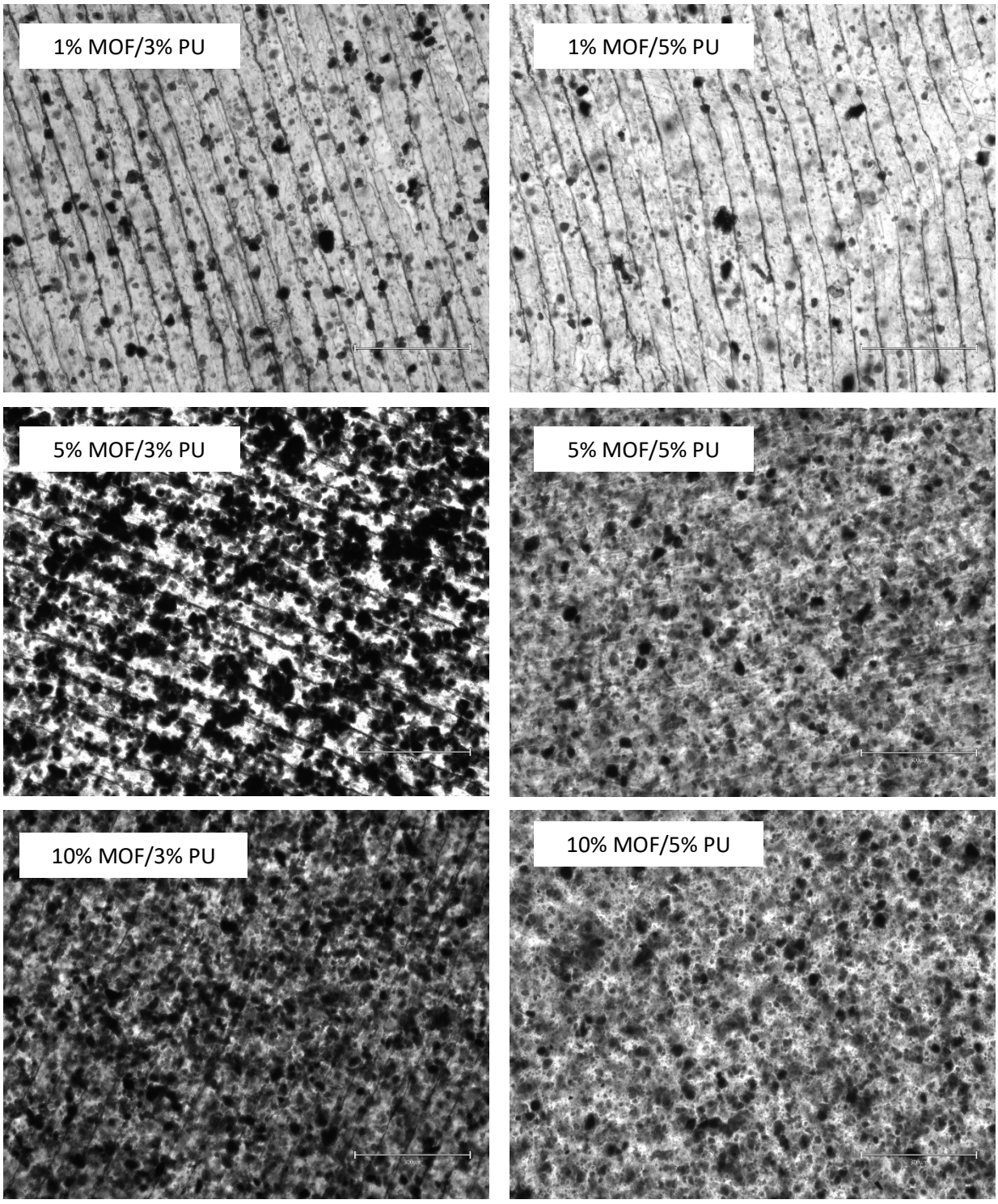

Figure 4.2B. Optical microscope images 10X) of MOF composites. Left: 3% PU films at 1% (top), 5% (middle), and 10% (bottom) MOF loading. Right: 5% PU films at 1% (top), 5% (middle), and 10% (bottom) MOF loading.

4.3.6 General Characterization

Powder X-ray diffraction (PXRD) patterns collected using Bruker D8 Discover DaVinci (Bruker, Billerica, MA, U.S.A.) diffractometer with CuKα radiation from 5-50 2theta at 0.2 s/step. Scanning electron microscopy (SEM) images collected using JEOL 6500 field emission SEM (Peabody, MA, U.S.A) at 15 kV accelerating voltage at 15,000X with 20 nm gold sputter coating to measure MOF particle diameter (n = 150). Optical microscopy images collected using an Invitrogen EVOS M5000 microscope (Waltham, MA, U.S.A.) with 10X objective.

4.3.7 Water Uptake Measurements

The weight of 1.2 cm diameter composite films was measured before (W_i) and after (W_f) each NOA experiment using an Ohaus DV215CD analytical balance (Pine Brook, NJ). Excess water was blotted before weighing. Percent water uptake was calculated using the equation:

$$\left(\frac{W_f - W_i}{W_i}\right) \times 100\%$$

4.3.8 Nitric Oxide Generation Measurements

Chemiluminescence-based Nitric Oxide Analyzers (NOA 280i, GE Analytical and Zysense, Colorado, U.S.A) were used to measure NO generation from the MOF composites. A two-point calibration was performed using zero air (<1 ppb NO) and nitric oxide calibrant gas (43.6 ppm NO). The 1.2 cm composite films were fully swelled prior to NO release experiments by soaking in water for exactly 5 minutes. NO concentration (ppb) was recorded as a function of time after injecting GSNO into a glass reaction cell containing the submersed film to make the desired final concentration of GSNO (1.0×10^{-5} M). The measurements were made at 25 °C with constant N_2 bubbling and shielded from light at an interval of 1 s. All the samples generated similar NO release profiles with four distinct phases (Fig. 4.3 for visual depiction): a short

induction period after GSNO injection, increasing linear rate of NO generation, steady-state NO flux, and a sharp return to baseline when GSNO has been consumed.

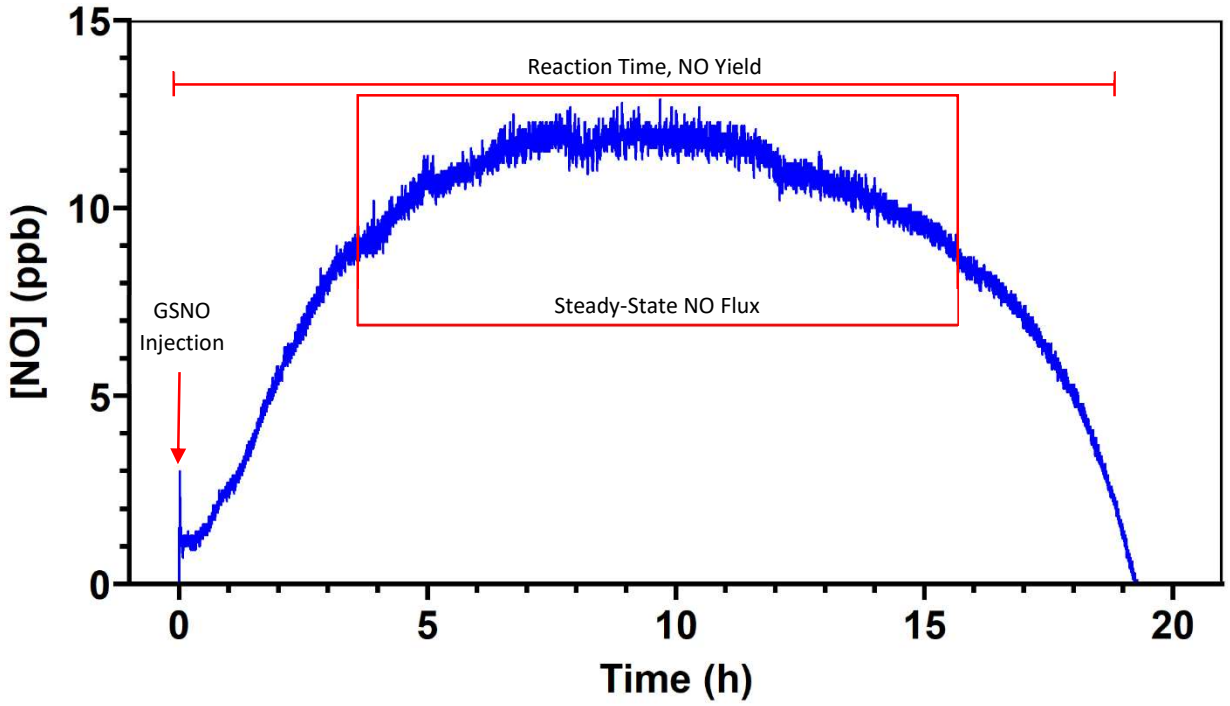

Figure 4.3. Example representation of NO generation from a composite film with labels to show how each statistic is quantified.

4.3.9 Data Reporting and Analysis

Four metrics were used to compare NO generation by the composite films collected by the NOA. A) Reaction time: Measured from GSNO injection until NO release returns to instrument baseline. B) NO yield: Using an instrument-specific calibration constant (mol s^{-1} ppb^{-1}) and the measurement interval (s), NO concentration (ppb) was converted to moles NO. Moles GSNO was calculated from the known concentration and volume of GSNO added to the reaction cell then converted to moles NO. NO yield was calculated using the equation:

$$\left(\frac{NO\ (mol)_{NOA}}{NO\ (mol)_{GSNO}}\right) \times 100\%$$

C) NO flux: Moles NO was converted to NO flux (nmol min^{-1} cm^{-2}) using the surface area of the film. The average flux was calculated for each replicate measurement over the time period in which NO generation was at a steady-state. Refer to Figure 4.3 for visual representation of each statistic. Data is reported as the mean ± standard deviation (SD) of n = 3 replicate experiments. Statistical significance was determined using one-way ANOVA with post hoc Tukey HSD at a 95% confidence interval.

4.4 Results and Discussion

The goal of this study was to examine how varying the parameters MOF particle preparation, MOF loading, and polymer concentration impact the ability of a polymer-embedded catalytic MOF to generate NO. Aside from the identity of the MOF and polymer, these are three of the key ways MOF composite fabrication can be tuned to alter performance, yet a systematic study of the effects of these parameters has yet to be conducted. Of note, in all cases the composite films were able to absorb more than 100% of their weight in water despite incorporation of the MOF, indicating that the polymer retained its desired physical properties (Table 4.1), and all the films except one generated NO yields over 90% indicating that the formulations are effective NO generating materials.

4.4.1 The Effects of MOF Preparation Methods and Particle Size on NO Generation

Prior to incorporation into composite materials, MOFs are often ground, ball-milled, or sonicated to alter the particle morphology and/or reduce the particle size of the MOF crystals for specific applications.[13,35] In 2020, our group discovered that CuBTTri-catalyzed generation of NO from GSNO occurs at unsaturated exterior surface copper sites on CuBTTri particles rather than within the pores.[36] In support of that observation, they also reported that large MOF particles (~1 mm diameter) exhibited markedly slower rates of catalysis compared with particles

less than 2 μm in diameter, and the initial rate of GSNO oxidation increased two-fold when the particle size is reduced from approximately 1.5 μm to less than 1 μm in diameter. It was unknown prior to the current work if this direct correlation between particle size and catalytic rate will remain for CuBTTri embedded within a polymer matrix. To explore this question, three sets of CuBTTri particles were prepared with different levels of processing, raw, as-synthesized particles (abbr. "raw", 0.4 ± 0.2 μm diameter), hand-ground particles (abbr. "ground", 0.3 ± 0.1 μm diameter), and particles that were ground, sonicated, and collected via filtration through a 1 μm filter (abbr. "filtered", 0.2 ± 0.1 μm diameter) (see Fig. 4.1 for SEM images of the MOF particles). These particles were incorporated into composite materials comprised of 5 wt.% CuBTTri/3 w/v% PU (see Fig. 4.2 for magnified images of the prepared films). PXRD analysis confirmed that MOF crystallinity was retained after using these processing methods (see Fig. 4.4 for PXRD patterns) and NOA analyses confirmed that that the smaller CuBTTri powder particles simply suspended in water catalyzed the reaction faster than the larger particles (filtered > ground > raw, see Table 4.2). It is important to note that these simple controls differed from the standard conditions herein in that they contained an equivalent of reduced glutathione (GSH), but nevertheless serve as a useful control to reproduce the previous particle size versus NO generation rate observed by our group.

The results of the NO generation analysis (see Table 4.3 and Fig. 4.5) show that the simple process of hand grinding the raw CuBTTri particles increased the average NO flux by 120% ($p = 0.000086$) and decreased the total reaction time by more than half ($p = 0.0015$). This result was unsurprising, as grinding shears the MOF particles and breaks up aggregates, increasing the number of exterior surface copper sites available for GSNO to NO oxidation catalysis as predicted by the preceding study from our group.[35] Curiously, we found that further

processing the particles by sonication and filtration inhibited the ability of CuBTTri to catalyze the generation of NO within a polymer matrix. In fact, the average flux is not statistically different ($p = 0.71$) than that of the PU control film with no MOF. Further experiments will be needed to parse the complexities of this observation; regardless, reducing the MOF particle size does not always elicit an increased rate of NO generation when fabricated into a composite material.

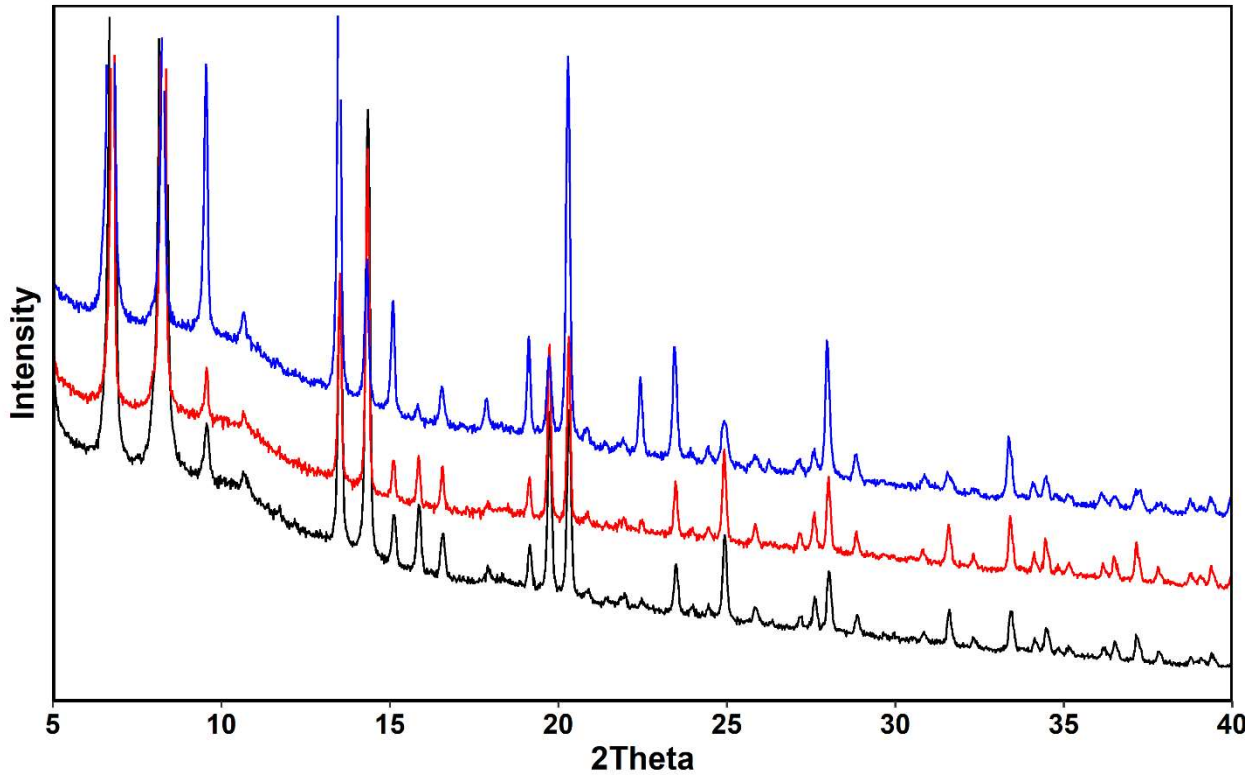

Figure 4.4. PXRD of raw (black, bottom), ground (red, middle), and filtered (blue, top) MOF particles. Sloping baseline due to residual adsorbed water.

Table 4.2. CuBTTri powder comparing three MOF preparation techniques.

	MOF Preparation[b]	Particle Size (μm)	Reaction Time[c] (h)	NO Yield (%)
CuBTTri Powder[a]	Raw	0.4 ± 0.2	1.8 ± 0.8	92 ± 2
	Ground	0.3 ± 0.1	1.4 ± 0.2	93 ± 6
	Filtered	0.2 ± 0.1	1.2 ± 0.1	96 ± 6

[a]CuBTTri powder added at 0.9-1.0 mg, the estimated amount in one 1.2 cm diameter 5 wt.% CuBTTri/3 w/v% PU film.
[b]CuBTTri powder processing identical to the CuBTTri in the composite materials, except that they were stirred rapidly for 1 h in the water used for the NOA experiments rather than THF used to prepare the composites.
[c]Experiments conducted using the NOA in ultrapure water with constant N_2 bubbling at 25 °C shielded from light with constant N_2 bubbling with 10×10^{-6} M GSNO and 10×10^{-6} M GSH. Data reported as mean ± SD (n = 3).

Table 4.3. Composites comparing three MOF preparation techniques.

	MOF Preparation	Reaction Time[b,c] (h)	NO Flux (nmol/cm²·min)	NO Yield (%)
Composites[a]	Raw	4.5 ± 0.6	0.059 ± 0.008	99 ± 4
	Ground	2.0 ± 0.1	0.13 ± 0.01	97 ± 6
	Filtered	1.0[d]	0.003 ± 0.004	0.6 ± 0.4
Control	N/A	1.0	0.002 ± 0.001	0.2 ± 0.1

[a]1.2 cm diameter films prepared with 5 wt.% MOF and 3 w/v% PU.
[b]Experiments conducted using the NOA in ultrapure water with constant N_2 bubbling at 25 °C shielded from light with constant N_2 bubbling with 10×10^{-6} M GSNO.
[c]Data reported as mean ± SD (n = 3).
[d]Experiments stopped at 1 h if no NO release occurred.

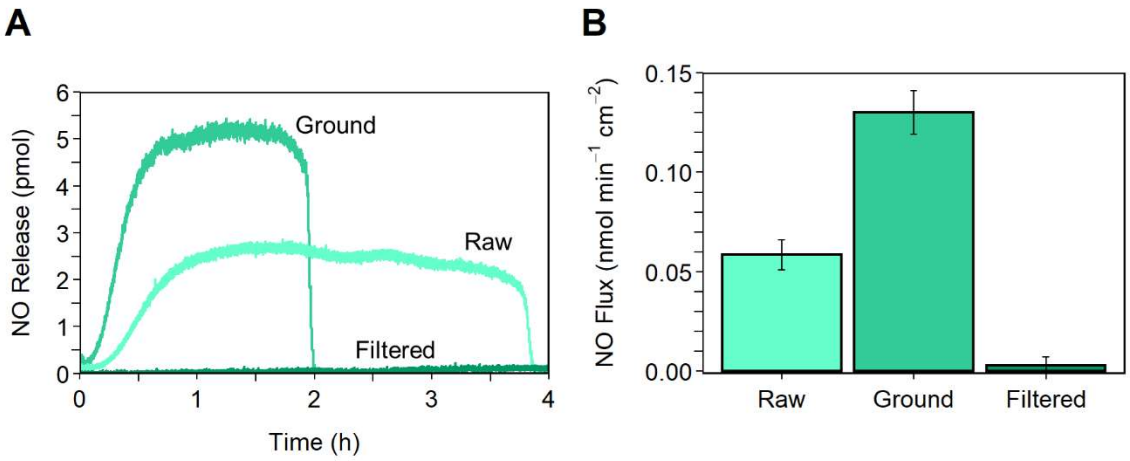

Figure 4.5. NO generation as a function of MOF particle preparation. (A) Representative NO release profiles and (B) average NO flux comparing the raw, ground, and filtered MOF particles. Experiments conducted using the NOA in ultrapure water with constant N_2 bubbling at 25 °C shielded from light with 10×10^{-6} M GSNO. Composites (1.2 cm diameter) comprised of 5 wt.% MOF and 3 w/v% PU. Data reported as mean ± SD (n = 3).

4.4.2 The Effects of MOF Loading and Polymer Concentration on NO Generation

Based on the previous results, ground CuBTTri particles were selected for the remainder of the experiments because they exhibited the greatest activity for NO generation in composite materials. CuBTTri concentrations of 1, 5, and 10 wt.% in the composite were tested to evaluate the relative impact of MOF loading on NO generation. This low MOF concentration range was selected to preserve the mechanical properties of the polymer in which the MOF is being incorporated.[37,38] The polymer used in this study, Tecophilic SP-80A-150, is a medical grade hydrophilic polyether-based aliphatic thermoplastic polyurethane. Polyurethanes are frequently used in implantable medical devices such as catheters and glucose biosensors due to their demonstrated biocompatibility (i.e., inertness within biological systems), biostability, inherent resistance to cell adhesion, and their excellent mechanical properties such as tensile and tear strength and abrasion resistance.[39-43] This particular polyurethane was selected for its ability to absorb water up to 150% of its dry weight. Water absorption has two major benefits for blood-

contacting applications. First, hydrophilic polymers tend to foul less than their hydrophobic counterparts due to the presence of a hydration layer formed through hydrogen bonding at the polymer-fluid interface.[44] Second, based on previous research we hypothesize that the ability of the polymer to absorb water will enhance the interaction between GSNO and embedded CuBTTri particles by facilitating GSNO diffusion into the composite material.[21,25] PU concentrations of 1, 3, 5% (w/v) were selected as a practical range for applying to medical device surfaces by commonly used deposition methods such as dip-coating and spin-coating based on the observed viscosity of the PU solutions.[45-47] MOF composites formulated in each possible combination of MOF loading and PU concentration were analyzed to evaluate their on the NO generation potential of MOF composites. The results are presented in Table 4.4 and Figures 4.6 and 4.7.

Table 4.4. Composite films comparing MOF loading and polymer concentration.

[MOF][a] (wt.%)	**[PU] (w/v%)**	**Reaction Time[b,c] (h)**	**NO Flux (nmol/cm²·min)**	**NO Yield (%)**
1	1	7.1 ± 0.2	0.046 ± 0.003	106 ± 10
1	3	4.2 ± 0.5	0.060 ± 0.008	94 ± 6
1	5	2.8 ± 0.3	0.10 ± 0.02	98 ± 7
5	1	3.6 ± 0.3	0.079 ± 0.002	98 ± 2
5	3	2.0 ± 0.1	0.13 ± 0.01	97 ± 6
5	5	2.3 ± 0.3	0.12 ± 0.02	95 ± 1
10	1	3.1 ± 0.3	0.086 ± 0.006	93 ± 2
10	3	2.1 ± 0.1	0.136 ± 0.008	94 ± 3
10	5	1.6 ± 0.3	0.20 ± 0.02	103 ± 6
0	3	1.0[d]	0.002 ± 0.001	0.2 ± 0.1

[a]MOF particles were ground.
[b]Experiments conducted using the NOA in ultrapure water with constant N_2 bubbling at 25 °C shielded from light with 10×10^{-6} M GSNO.
[c]Data reported as mean ± SD (n = 3).
[d]Experiments stopped at 1 h if no NO release occurred.

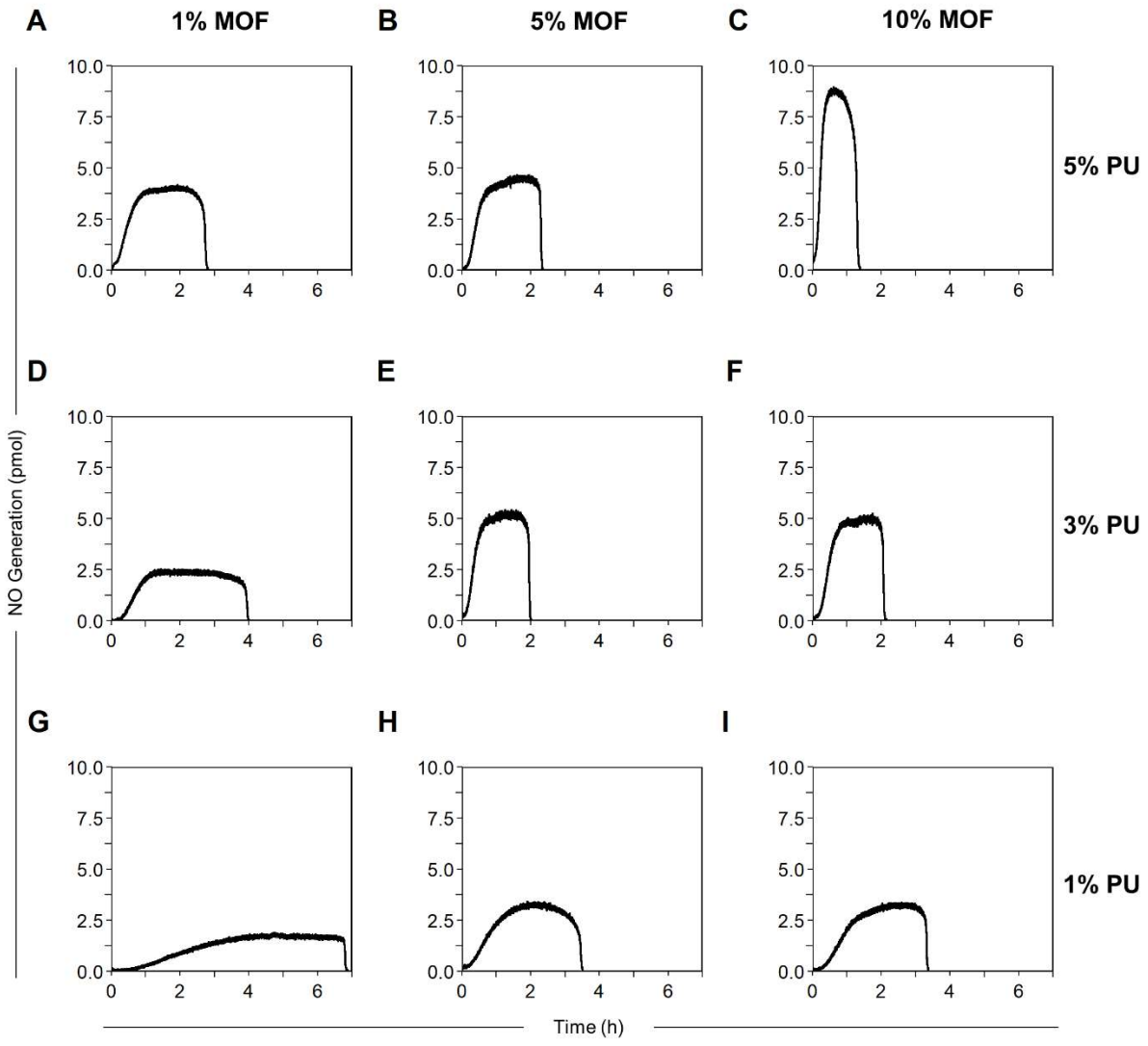

Figure 4.6. Representative NO release profiles as a function of MOF loading and PU concentration. Composite fabricated with: (A) 1 wt.% MOF, 5 w/v% PU, (B) 5 wt.% MOF, 5 w/v% PU, (C) 10 wt.% MOF, 5 w/v% PU, (D) 1 wt.% MOF, 3 w/v% PU, (E) 5 wt.% MOF, 3 w/v% MOF, (F) 10 wt.% MOF, 3 w/v% MOF, (G) 1 wt.% MOF, 1 w/v% PU, (H) 5 wt.% MOF, 1 w/v% PU, (I) 10 wt.% MOF, 1 w/v% PU. Experiments conducted using the NOA in ultrapure water with constant N_2 bubbling at 25 °C shielded from light with 10×10^{-6} M GSNO. Composites (1.2 cm diameter) fabricated with ground MOF.

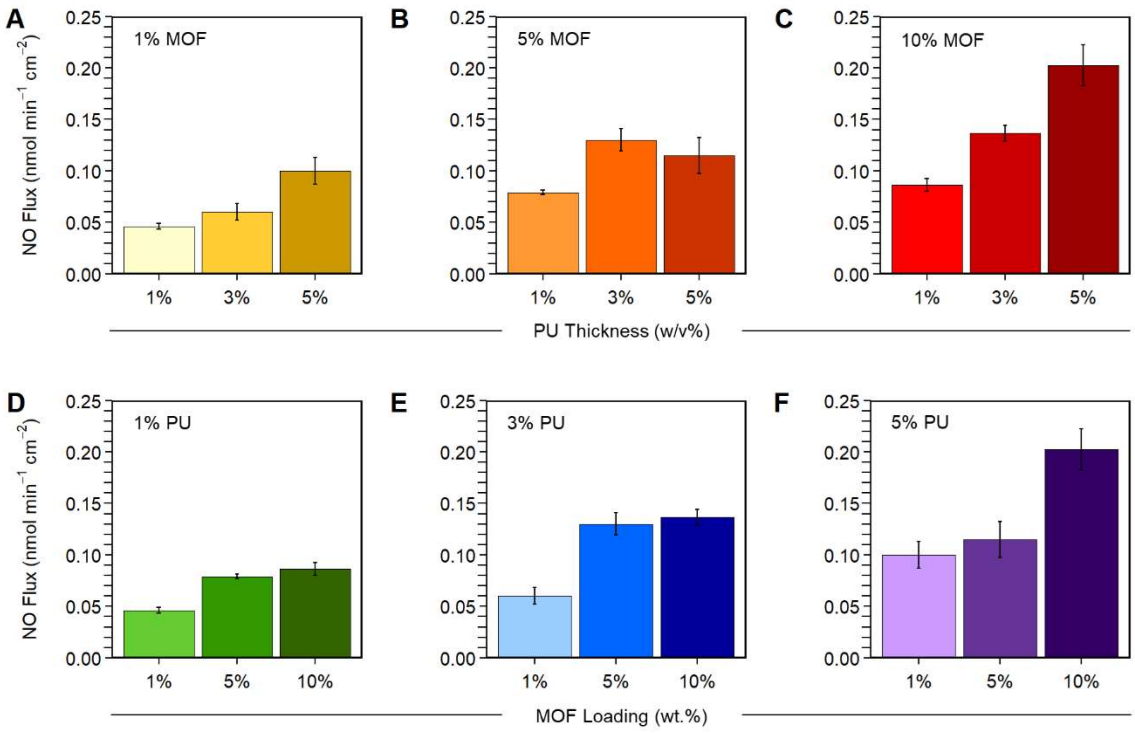

Figure 4.7. Top: Varying PU concentration at different MOF loadings. (A) 1 wt.% MOF, (B) 5 wt.% MOF, (C) 10 wt.% MOF at 1, 3, and 5 w/v% PU. Bottom: Varying MOF loading at different PU concentrations. (D) 1 w/v% PU, (E) 3 w/v% PU, (F) 5 w/v% PU at 1, 5, and 10 wt.% MOF. Experiments conducted using the NOA in ultrapure water with constant N_2 bubbling at 25 °C shielded from light with 10×10^{-6} M GSNO. Composites (1.2 cm diameter) fabricated with ground MOF. Data reported as mean ± SD (n = 3).

4.4.3 Varying Polymer Concentration at A Constant MOF Loading

At 1% MOF loading, we observed a trend in which each increase in PU concentration at constant MOF loading resulted in statistically significant effects on NO flux and reaction time. Increasing the PU concentration from 1% to 3% increased NO flux by 130% ($p = 0.045$) and decreased the reaction time by 41% ($p = 0.00063$) (Fig. 4.6G, D; Fig. 4.7A). Further increasing PU concentration from 3% to 5% increased NO flux by 130% ($p = 0.012$) and decreased the reaction time by 34% ($p = 0.011$) (Fig. 4.6D, A; Fig. 4.7A).

At 5% MOF loading, we observed that increasing from 1% to 3% PU had significant effects on NO flux (61% increase, $p = 0.0045$) and reaction time (43% decrease, $p = 0.0010$)

(Fig. 4.6H, E; Fig. 4.7B), but increasing from 3% to 5% PU had no impact on performance (Fig. 4.6E, B; Fig. 4.7B).

At 10% MOF loading, we observed that each increase in PU concentration resulted in significant increases in NO flux at constant MOF loading. From 1% to 3% PU NO flux increased 60% ($p = 0.0071$), and from 3% to 5% PU increased 50% ($p = 0.0018$) (Fig. 4.6I, F, C; Fig. 4.7C). We also observed significant reductions in reaction time (33% decrease, $p = 0.0041$) increasing PU concentration from 1% to 3%, which was not observed increasing from 3% to 5% PU.

In light of these results, we were curious if decreases in PU concentration for composites fabricated with the smaller filtered MOF particles from Section 4.4.1 would increase NO generation the same way increases in PU concentration tended to increase NO generation for composites with the relatively larger ground MOF particles. We explored this question by reducing the PU concentration from the original 3% PU composite that did not generate NO to 1% PU with the filtered MOF particles at equivalent 5% MOF loadings. The 1% PU composite generated an NO flux of 0.014 ± 0.008 nmol cm^{-2} min^{-1} over 17 ± 5 h reaction time, an approximately 4-fold increase in NO flux compared to the original 3% PU composite (albeit not statistically significantly, $p = 0.11$). These results seem to indicate that the effectiveness of a MOF composite material is dependent on selecting an appropriate polymer concentration for a particular MOF particle size (i.e., smaller MOF particles require lower polymer concentrations to exhibit greater NO generation), though further exploration is required to make a definitive statement.

To summarize, at low MOF loadings each increase in PU concentration resulted in substantial, statistically significant increases in NO flux and decreases in total reaction time. At

high MOF loadings, increasing PU concentration produced moderate, statistically significant increases in NO flux with less impact on total reaction time.

4.4.4 Varying MOF Loading at A Constant Polymer Concentration

At 1% PU concentration, we observed that increasing MOF loading from 1% to 5% significantly increased NO flux by 58% ($p = 0.00016$) and cut the total reaction time in half ($p = 0.000015$) (Fig 4.6G, H; Fig. 4.7D), but NO generation was not affected increasing MOF loading from 5% to 10%.

At 3% PU concentration, we saw a similar results to those at 1% PU. Increasing MOF loading from 1% to 5% increased NO flux by 150% ($p = 0.00019$) and decreased the total reaction time by 50% ($p = 0.00020$), while increasing MOF loading from 5% to 10% did not result in any significant effects on NO generation (Fig. 4.6D, E, F; Fig. 4.7E).

At 5% PU concentration, we observed the opposite trend as the previous two PU concentrations. Increasing MOF loading from 1% to 5% did not impact NO generation, while increasing from 5% to 10% increased NO flux by 170% ($p = 0.0018$) and decreased the reaction time by 32% ($p = 0.039$) (Fig. 4.6A, B, C; Fig. 4.7F).

Overall, increasing MOF loading at a constant PU concentration did not predictably increase NO generation, but generally NO flux was lower at low PU concentrations and greater at high PU concentrations.

4.4.5 Analysis of Relationship Between MOF Loading and PU Concentration on NO Generation

Taken together, we saw that composite films with high MOF loadings and high polymer concentrations had greater rates of NO generation than those with low MOF loadings and low polymer concentrations. Increases in PU concentration more consistently increased NO generation compared to MOF loading; but notably, increases in either PU concentration or MOF

loading never decreased rates of NO generation. There were only four instances in which there was no increase in NO generation observed after increasing either MOF loading or PU concentration that are worth exploring.

The first instance in which no metrics were affected by increasing PU concentration was from 3% to 5% at 5% MOF loading. This result is in contrast to increasing the PU concentration from 1% to 3% at the same MOF loading in which a significant increase in NO flux occurred. Interestingly, we noted that a significant decrease ($p = 0.014$) in water uptake occurred increasing 1% to 3% PU, but no change from 3% to 5% PU. In examining water uptake for all experiments, a general pattern emerged where the greater the water uptake, the lower the NO flux; and we observed that the film with the greatest NO flux (10% CuBTTri/5% PU) had the lowest water uptake of all the composite films. We also found that changes in MOF loading at a constant PU concentration did not statistically impact water uptake, revealing that the concentration of the polymer is the major determinant for water uptake with CuBTTri/PU composites. The finding that water uptake is inversely proportional to NO generation is contrary to our initial thinking that greater rates of NO generation would be observed with greater swelling. This hypothesis was based on previous work by Neufeld et al. which found that the hydrophilic composite 10 wt.% CuBTTri/poly(vinyl alcohol) (203 ± 3% water uptake) generated NO while its hydrophobic counterpart 10 wt.% CuBTTri/Tecoflex SG-80A (2.0 ± 0.3% water uptake), did not.[25] Based on the results from our experiments, we concluded that there is an undetermined optimal level of water absorptivity unique to the composite polymer that enhances rates of NO generation.

The second two instances were observed under related sets of circumstances: when increasing MOF loading from 5% to 10% at both 1% and 3% PU concentrations. In contrast, the

analogous increase at 5% PU resulted in the greatest NO flux among all experiments. As we noted previously, composite materials with the same PU concentration have similar measured water absorptivity, so there must be an alternative factor contributing to the observed phenomenon. Based on the available data, we hypothesize that at 10% MOF loading crowding within the composite at lower PU concentrations reduces the number of MOF catalyst sites accessible to GSNO resulting in no appreciable increase in rate of NO generation (see Fig. 4.8A). Rather than evenly dispersed small, high exterior surface area MOF particles, crowding results in agglomerations or layers of MOF that more closely resemble larger, lower exterior surface area particles. The optical microscope images of these composites (Fig. 4.2) provide some evidence for this hypothesis. The images of 10% MOF composites at 1% and 3% PU have more MOF clustering and less free polymer space compared to the 10% MOF/5% PU film. This data shows that there is a limit to the effectiveness of increasing MOF loading to increase rate of NO generation without also increasing polymer concentration.

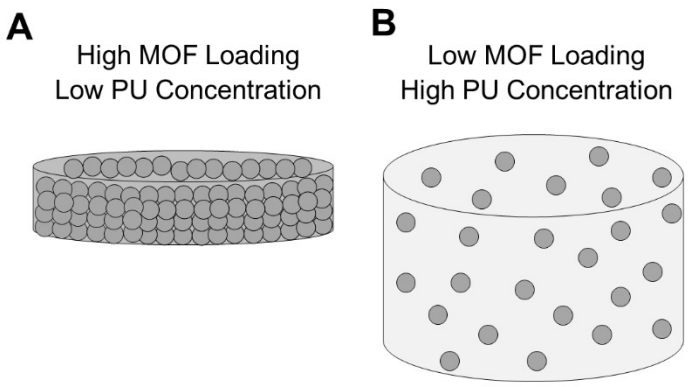

Figure 4.8. Hypothesized models of MOF composite NO generation. (A) High MOF loading, low PU concentration composites experience crowding in which MOF agglomerations or layers reduce total MOF surface area available for catalysis. (B) Low MOF loading, high PU concentration composites reduce analyte diffusion deep into center of film limiting number of accessible MOF particles for catalysis.

The fourth instance, increasing MOF loading from 1% to 5% at 5% PU, is an exception to the previous three instances. It is the only circumstance in which neither NO flux nor reaction

time was enhanced by increasing the MOF loading from 1% to 5% but is affected by further increases from 5% to 10%. We propose that, in the same way MOF composites with high MOF loadings and low PU concentrations experience MOF crowding, MOF composites with low MOF loadings and high PU concentrations have inaccessible MOF particles deep in the core of the film (see Fig. 4.8B). In this view of the composite material, the MOF is evenly dispersed throughout the width and depth of the film and GSNO diffusion past exterior MOF particles to the center is minimal. This reasoning also extends to the filtered MOF composite films and provides an explanation for their limited NO generation capacity.

4.5 Conclusions

This work provides insights for the rational design of catalytic MOF composites for medical device applications, highlighting the tunability of MOFs and MOF composites toward application-specific implementations. It also illustrates that while fundamental studies on a MOF catalyst in solution are important, the findings from those studies may not apply to the system in which the catalyst will be implemented. We found that MOF particle preparation, MOF loading, and PU concentration have major impacts on NO generation from MOF composite materials. In general, hand grinding the MOF prior to fabrication, higher MOF loading, and greater PU concentration increase rates of NO generation. Other important considerations include the water absorptivity of the composite material and MOF loading relative to PU concentration. These findings provide useful data for selecting the formulation to apply as an outer polymer membrane to enhance the blood compatibility of implantable glucose biosensors.

CHAPTER 4

REFERENCES

(1) Kang, Y. S.; Lu, Y.; Chen, K.; Zhao, Y.; Wang, P.; Sun, W. Y. Metal–Organic Frameworks with Catalytic Centers: From Synthesis to Catalytic Application. *Coord. Chem. Rev.* **2019**, 378, 262–280.

(2) Altintas, C.; Altundal, O. F.; Keskin, S.; Yildirim, R. Machine Learning Meets with Metal Organic Frameworks for Gas Storage and Separation. *J. Chem. Inf. Model.* **2021**, *61* (5), 2131–2146.

(3) Abuzalat, O.; Tantawy, H.; Abdlaty, R.; Elfiky, M.; Baraka, A. Advances of the Highly Efficient and Stable Visible Light Active Photocatalyst Zr(Iv)-Phthalate Coordination Polymer for the Degradation of Organic Contaminants in Water. *Dalt. Trans.* **2021**, *50* (24), 8600–8611.

(4) Metal-Organic Frameworks: Applications in Separations and Catalysis; Garcia, H., Navalon, S., Eds.; *Wiley-VCH*, **2018**.

(5) Kang, Y.-S.; Lu, Y.; Chen, K.; Zhao, Y.; Wang, P.; Sun, W.-Y. Metal–Organic Frameworks with Catalytic Centers: From Synthesis to Catalytic Application. *Coord. Chem. Rev.* **2019**, *378*, 262–280.

(6) Bavykina, A.; Kolobov, N.; Khan, I. S.; Bau, J. A.; Ramirez, A.; Gascon, J. Metal-Organic Frameworks in Heterogeneous Catalysis: Recent Progress, New Trends, and Future Perspectives. *Chem. Rev.* **2020**, *120* (16), 8468–8535.

(7) Xu, C.; Fang, R.; Luque, R.; Chen, L.; Li, Y. Functional Metal–Organic Frameworks for Catalytic Applications. *Coord. Chem. Rev.* **2019**, *388*, 268–292.

(8) Kirlikovali, K. O.; Chen, Z.; Wang, X.; Mian, M. R.; Alayoglu, S.; Islamoglu, T.; Farha, O. K. Investigating the Influence of Hexanuclear Clusters in Isostructural Metal-Organic Frameworks on Toxic Gas Adsorption. *ACS Appl. Mater. Interfaces* **2022**, *14* (2), 3048–3056.

(9) Stock, N.; Biswas, S. Synthesis of Metal-Organic Frameworks (MOFs): Routes to Various MOF Topologies, Morphologies, and Composites. *Chem. Rev.* **2012**, *112* (2), 933–969.

(10) Wang, Z.; Liu, L.; Li, Z.; Goyal, N.; Du, T.; He, J.; Li, G. K. Shaping of Metal-Organic Frameworks: A Review. *Energy and Fuels* **2022**, *36*, 2927–2944.

(11) Ma, Q.; Zhang, T.; Wang, B. Shaping of Metal-Organic Frameworks, a Critical Step toward Industrial Applications. *Matter* **2022**, *5* (4), 1070–1091.

(12) Kalaj, M.; Bentz, K. C.; Ayala, S.; Palomba, J. M.; Barcus, K. S.; Katayama, Y.; Cohen, S. M. MOF-Polymer Hybrid Materials: From Simple Composites to Tailored Architectures. *Chem. Rev.* **2020**, *120* (16), 8267–8302.

(13) Kitao, T.; Zhang, Y.; Kitagawa, S.; Wang, B.; Uemura, T. Hybridization of MOFs and Polymers. *Chem. Soc. Rev.* **2017**, *46* (11), 3108–3133.

(14) Husna, A.; Hossain, I.; Jeong, I.; Kim, T.-H. Mixed Matrix Membranes for Efficient CO2 Separation Using an Engineered UiO-66 MOF in a Pebax Polymer. *Polymers* **2022**, *14* (4), 655.

(15) Zhang, W.; Li, B.; Duan, W.; Yao, X.; Lu, X.; Li, S.; Tian, Y.; Li, D. Confined: In Situ Polymerization in a Nanoscale Porphyrinic Metal-Organic Framework for Fluorescence Imaging-Guided Synergistic Phototherapy. *Inorg. Chem. Front.* **2022**, *9* (4), 670–677.

(16) Kobayashi, Y.; Honjo, K.; Kitagawa, S.; Uemura, T. Preparation of Porous Polysaccharides Templated by Coordination Polymer with Three-Dimensional Nanochannels. *ACS Appl. Mater. Interfaces* **2017**, *9* (13), 11373–11379.

(17) Zahir, M. H.; Helal, A.; Hakeem, A. S. Hybrid PolyMOF Materials Prepared by Combining an Organic Polymer with a MOF and Their Application for Solar Thermal Energy Storage. *Energy and Fuels* **2021**, *35* (12), 10199–10209.

(18) Jiang, Y.; Sun, J.; Yang, X.; Shen, J.; Fu, Y.; Fan, Y.; Xu, J.; Wang, L. Cd-MOF@PVDF Mixed-Matrix Membrane with Good Catalytic Activity and Recyclability for the Production of Benzimidazole and Amino Acid Derivatives. *Inorg. Chem.* **2021**, *60* (3), 2087–2096.

(19) Gao, K.; Guo, X.; Zheng, B.; Wang, J.; Wang, L. Investigation of Interface Compatibility in Stiff Polymer/Metal–Organic Frameworks. Mater. Today Chem. 2021, 20, 100458.

(20) Palomba, J. M.; Wirth, D. M.; Kim, J. Y.; Kalaj, M.; Clarke, E. M.; Peterson, G. W.; Pokorski, J. K.; Cohen, S. M. Strong, Ductile MOF-Poly(Urethane Urea) Composites. *Chem. Mater*. **2021**, *33* (9), 3164–3171.

(21) Denny, M. S.; Kalaj, M.; Bentz, K. C.; Cohen, S. M. Multicomponent Metal-Organic Framework Membranes for Advanced Functional Composites. *Chem. Sci.* **2018**, *9* (47), 8842–8849.

(22) Sorribas, S.; Kudasheva, A.; Almendro, E.; Zornoza, B.; de la Iglesia, Ó.; Téllez, C.; Coronas, J. Pervaporation and Membrane Reactor Performance of Polyimide Based Mixed Matrix Membranes Containing MOF HKUST-1. *Chem. Eng. Sci.* **2015**, *124*, 37–44.

(23) McCarthy, D. L.; Liu, J.; Dwyer, D. B.; Troiano, J. L.; Boyer, S. M.; Decoste, J. B.; Bernier, W. E.; Jones, W. E. Electrospun Metal-Organic Framework Polymer Composites for the Catalytic Degradation of Methyl Paraoxon. *New J. Chem.* **2017**, *41* (17), 8748–8753.

(24) J. Neufeld, M.; Lutzke, A.; B. Tapia, J.; M. Reynolds, M. Metal–Organic Framework/Chitosan Hybrid Materials Promote Nitric Oxide Release from S-Nitrosoglutathione in Aqueous Solution. *ACS Appl. Mater. Interfaces* **2017**, *9* (6), 5139–5148.

(25) Neufeld, M. J.; Lutzke, A.; Jones, W. M.; Reynolds, M. M. Nitric Oxide Generation from Endogenous Substrates Using Metal-Organic Frameworks: Inclusion within Poly(Vinyl Alcohol) Membranes to Investigate Reactivity and Therapeutic Potential. *ACS Appl. Mater. Interfaces* **2017**, *9* (41), 35628–35641.

(26) Garren, M.; Maffe, P.; Melvin, A.; Griffin, L.; Wilson, S.; Douglass, M.; Reynolds, M.; Handa, H. Surface-Catalyzed Nitric Oxide Release via a Metal Organic Framework Enhances Antibacterial Surface Effects. *ACS Appl. Mater. Interfaces* **2021**, *13*, 56931–56943.

(27) Tuttle, R. R.; Rubin, H. N.; Rithner, C. D.; Finke, R. G.; Reynolds, M. M. Copper Ion vs Copper Metal–Organic Framework Catalyzed NO Release from Bioavailable S-Nitrosoglutathione En Route to Biomedical Applications: Direct 1H NMR Monitoring in Water Allowing Identification of the Distinct, True Reaction Stoichiometries and Thio. *J. Inorg. Biochem.* **2019**, *199* (July), 110760.

(28) Harding, J. L.; Metz, J. M.; Reynolds, M. M. A Tunable, Stable, and Bioactive MOF Catalyst for Generating a Localized Therapeutic from Endogenous Sources. *Adv. Funct. Mater.* **2014**, *24* (47), 7503–7509.

(29) Moncada, S.; Higgs, E. A. The Discovery of Nitric Oxide and Its Role in Vascular Biology. Br. *J. Pharmacol.* **2006**, *147*, S193–S201.

(30) Carpenter, A. W.; Schoenfisch, M. H. Nitric Oxide Release Part II. Therapeutic Applications. *Chem. Soc. Rev.* **2012**, *41* (10), 3742–3752.

(31) Wo, Y.; Brisbois, E. J.; Bartlett, R. H.; Meyerhoff, M. E. Recent Advances in Thromboresistant and Antimicrobial Polymers for Biomedical Applications: Just Say Yes to Nitric Oxide (NO). *Biomater. Sci.* **2016**, *4* (8), 1161–1183.

(32) Vaughn, M. W.; Kuo, L.; Liao, J. C. Estimation of Nitric Oxide Production and Reaction Rates in Tissue by Use of a Mathematical Model. *Am. J. Physiol.* **1998**, *274* (6), H2163–H2176.

(33) Radomski, M. W.; Palmer, R. M. J.; Moncada, S. The Role of Nitric Oxide and CGMP in Platelet Adhesion to Vascular Endothelium. *Biochem. Biophys. Res. Commun.* **1987**, *148* (3), 1482–1489.

(34) Cha, K. H.; Wang, X.; Meyerhoff, M. E. Nitric Oxide Release for Improving Performance of Implantable Chemical Sensors – A Review. *Appl. Mater. Today* **2017**, *9*, 589–597.

(35) Tuttle, R. R.; Folkman, S. J.; Rubin, H. N.; Finke, R. G.; Reynolds, M. M. Copper Metal-Organic Framework Surface Catalysis: Catalyst Poisoning, IR Spectroscopic, and Kinetic Evidence Addressing the Nature and Number of the Catalytically Active Sites En Route to Improved Applications. ACS Appl. Mater. *Interfaces* **2020**, *12* (35), 39043–39055.

(36) Sastri, V. R. Engineering Thermoplastics: Acrylics, Polycarbonates, Polyurethanes, Polyacetals, Polyesters, and Polyamides. *In Plastics in Medical Devices*; **2014**; pp 121–172.

(37) Harding, J. L.; Reynolds, M. M. Combating Medical Device Fouling. *Trends Biotechnol.* **2014**, *32* (3), 140–146.

(38) Hart, T. W. SOME OBSERVATIONS CONCERNING THE S-NITROSO AND S-PHENYLSULPHONYL DERIVATIVES OF L-CYSTEINE AND GLUTATHIONE. *Tetrahedron Lett.* **1985**, *26* (16), 2013–2016.

(39) Parent, M.; Dahboul, F.; Schneider, R.; Clarot, I.; Maincent, P.; Leroy, P.; Boudier, A. A Complete Physicochemical Identity Card of *S*-Nitrosoglutathione. *Curr. Pharm. Anal.* **2013**, *9*, 31–42.

(40) Demessence, A.; Alessandro, D. M. D.; Foo, M. L.; Long, J. R. Strong CO2 Binding in a Water-Stable, Triazolate-Bridged Metal−Organic Framework Functionalized with Ethylenediamine. *J. Am. Chem. Soc.* **2009**, *131* (25), 8784–8786.

CHAPTER 5

NITRIC OXIDE-GENERATING COPPER(II) BENZENE-1,3,5-TRIS(1*H*-1,2,3-TRIAZOY-5-YL)/POLYURETHANE COMPOSITE MATERIAL FOR ANTI-FOULING GLUCOSE BIOSENSOR COATINGS

5.1 Overview

Herein, we apply the findings from the previous chapters to fabricate an anti-fouling polymer membrane for a blood-contacting enzymatic glucose biosensor. In brief, robust analytical methods for were developed, the effects of embedding a MOF in a polymer were analyzed, and a systematic examination of relevant composite material parameters on NO generation was conducted for the polyurethane-embedded CuBTTri (Cu(II) benzene-1,3,5-tris(1*H*-1,2,3-triazoy-5-yl)) generation of nitric oxide from *S*-nitrosoglutathione (GSNO). This chapter addresses the research questions: 1) Which composite formulation is optimal for a biosensor semipermeable outer membrane? 2) Does the presence of CuBTTri in the outer membrane impact enzyme function? 3) Does the presence of CuBTTri in the outer polymer membrane of the sensor impact amperometric detection of hydrogen peroxide?

5.2 Introduction

The prevalence of diabetes worldwide has increased substantially from 108 million individuals in 1980 to over 400 million individuals in 2014.[1] Many individuals suffering from diabetes require insulin injections to maintain blood glucose levels in order to survive. For this reason, they must have a sensitive and reliable method to monitor their glucose. Implantable devices have attracted attention as the preferred method for monitoring glucose for two major reasons. It does not require users to obtain drops of blood for testing by “finger-pricking” and it

continuously monitors changes in glucose levels, allowing individuals to evaluate trends and detect critical changes in glucose levels, particularly for those who are critically-ill.[2]

Considerable research has been dedicated to the development of reliable indwelling devices; however, biocompatibility with the surrounding biological environment remains an obstacle.[3] Biofouling, in which inflammation or thrombosis occur at the site of the implant, reduce the accuracy and longevity of the sensor, ultimately resulting in device failure.[4,5] Researchers have approached the problem of biocompatibility at the device surface by implementing various strategies which can be broadly categorized in two ways: altering the membrane material or releasing a localized therapeutic. Examples of the former include zwitterionic,[6] porous,[7,8] or nanopatterned coating materials,[9,10] and examples of the latter include releasing tyrosine kinase inhibitors,[11,12] dexamethasone,[13-15] or nitric oxide.[16-18]

This research utilizes the release of nitric oxide (NO) as a locally-generated therapeutic for the enhanced thrombogenicity of a blood-contacting glucose biosensor. NO is involved in a range of biological processes such as the immune response to infection, wound repair, and cancer biology, as well as exhibiting antithrombic, antiproliferative, and anti-inflammatory effects in the vascular system.[19-20] The production of NO at biologically-relevant levels on the surface of implantable chemical sensors has been shown to be effective towards enhancing biocompatibility without impacting the analytical performance of the device.[16,21-24] NO can be generated from both exogenous (e.g. diazeniumdiolates) and endogenous (e.g. *S*-nitrosothiols) sources.[19] Use of exogeneous NO sources in biomaterials has been effective at reducing biofouling, but is a limited and uncontrolled source of NO release.[25,26] The therapeutic concentration of NO falls within a narrow range (0.1-10 nM), outside of which it is cytotoxic (>100 nM), highlighting the need for precise control over the rate of NO release. Conversely, exploitation of endogenous NO sources

by the introduction of catalysts on the device surface provides a theoretically infinite source of localized NO generation which can be tuned by catalyst loading. Herein, we present a novel application of CuBTTri in the glucose biosensor outer polymer membrane to generate NO from *S*-nitrosoglutathione as an antifouling agent for enhanced the biocompatibility.

5.3 Materials and Methods

5.3.1 Materials

Silver wire (Ag, 99.9%, 0.5 mm), and glutaraldehyde (25% aqueous solution) were purchased from Alfa Aesar (Ward Hill, MA). 2-(N-Morpholino)ethanesulfonic acid (MES) was purchased from HOPAXFC. Glucose oxidase (type VII, from *Aspergillus niger*), Nafion® (5 wt % in water and 1-propanol), potassium chloride, cellulose acetate (39.8 wt % acetyl), d-(+)-glucose, bovine serum albumin (BSA), and potassium ferricyanide ($K_3FE(CN)_6$, < 10 μm) was purchased from Sigma-Aldrich (St. Louis, MO). Iron(III) chloride 6-hydrate ($FeCl_3$) was purchased from Mallinckrodt Pharmaceuticals (St. Louis, MO). PBS tablets (10 mM) were purchased from VWR. PFA-coated platinum/iridium wire (PTFE-coated Pt/Ir, 25.4 μm diameter) was purchased from A-M Systems (Sequim, WA). Ultrapure water (18.2 MΩ·cm) was supplied by a Millipore Milli-Q IQ Water Purification System (EMD Millipore, Billerica, MA).

5.3.2 Composite Film Fabrication

Refer to Chapter 5 for Cu(II) benzene-1,3,5-tris(1H-1,2,3-triazoy-5-yl) (CuBTTri) synthesis and 5 wt.% CuBTTri/3 w/v% SP-80A-150 Tecophilic polyurethane composite material characterization. Briefly, polyurethane (0.3 g) was dissolved in 7 mL THF in a 20 mL vial overnight . CuBTTri (15 mg) was rapidly stirred in 3 mL THF in a separate 20 mL vial until no aggregates were visible. The CuBTTri solution was poured into the polyurethane solution and stirred for 15 min to combine.

5.3.3 Glucose Biosensor Design and Electrode Surface Functionalization

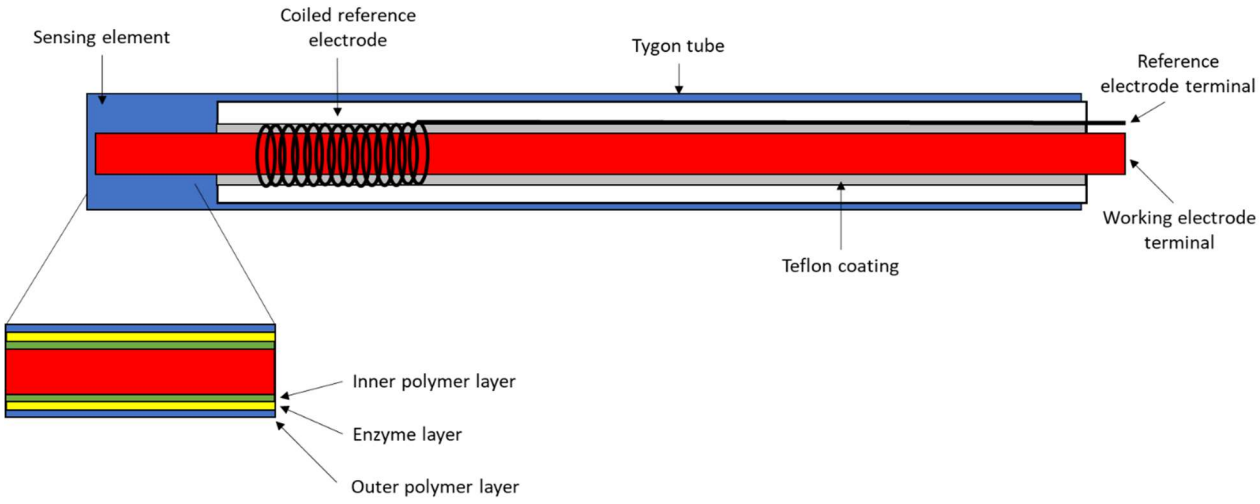

Figure 5.1. Schematic of a typical needle-type enzymatic glucose biosensor.

The needle-type electrochemical glucose biosensor design that this work is based on has been reported previously (Figure 5.1).[27,28] The silver wire (15 cm) was wrapped tightly around a PVC support (5 cm, 5 mm I.D.) 5 mm from the end, leaving a 5 cm straight section extending out to the opposite end of the PVC support for electrical contact. The coiled portion of the silver wire was dipped in a solution of 1 M $FeCl_3$ in 1 M HCl for 2 min to deposit AgCl as the reference electrode. The Ag/AgCl electrode was rinsed with water and placed in 1 M KCl until use. PFA-coated Pt/Ir wire (10 cm) was fed through a separate PVC support (7 cm, 1 mm I.D.) with 3 mm protruding from one end of the support. Both ends of the Pt-Ir wire were stripped of the PFA coating, one for electrical contact and one for depositing the sensing elements. The wire was secured to the PVC support with epoxy resin and the tip of the 3 mm portion of the wire was capped with epoxy resin leaving a 2 mm portion of wire exposed. The inner polymer membrane was fabricated by depositing 1 µL drops of alternating layers of 5 wt.% cellulose acetate in 1:1 acetone and ethanol and 5% Nafion® on the wire. A 1 µL drop of the enzyme layer consisting of a solution of bovine serum albumin (50 mg/mL) and glucose oxidase (20 mg/mL) in 0.1 M PBS

was deposited onto the sensing cavity of the Pt-Ir wire then crosslinked with 2% glutaraldehyde. The outer polymer membrane was deposited by dip-coating the Pt-Ir wire in 3% polyurethane (control) or 5 wt.% CuBTTri/3% polyurethane coating solution. The sensor was dried then soaked in 10 mM PBS until use.

5.3.4 Ultraviolet-Visible Spectroscopy (UV-Vis) Analysis

UV-Vis spectroscopy was used to assess if the presence of CuBTTri impacted the function of the glucose oxidase (GOx) enzyme with a method adapted from Dai et al.[29] To determine the linear concentration range of this method 50 µL 1.5 mM $FeCl_3$, 50 µL 1.5 mM $K_3Fe(CN)_6$, and 5 µL 1.1 mg mL^{-1} GOx in 50 mM MES buffer (pH 3) were added to 33 wells of a 96 well plate. Then 5 µL aliquots of glucose at initial concentrations of 0.0215, 0.043, 0.0859, 0.172, 0.688, 1.38, 2.75, 5.50, 11.0, 22.0, 44.0 mM (n = 3) were reacted with the solution for 10 min then the absorbance was measured at 706 nm using a BioTek Synergy 2 multi-mode microplate reader (Winooski, VT, USA) (LOD = 0.039; LOQ = 0.047, linear range = 0.000977–1.00 mM glucose, sensitivity = 0.40 Abs/mM). To assess if the presence of CuBTTri affects enzyme activity, a small section of a CuBTTri composite film (~5 mm diameter) was added to a solution containing 50 µL 1.5 mM $FeCl_3$, 50 µL 1.5 mM $K_3Fe(CN)_6$, 5 µL 1.1 mg mL^{-1} GOx, and 5 µL 0.172, 0.688, or 2.75 mM glucose in 50 mM MES buffer (pH 3). The film was removed and the absorbance of the solution was measured at 706 nm.

5.3.5 Electrochemical Measurements

Current-time (i-t) amperometric measurements were conducted at +0.7 V in 15 mM PBS with 10 µM GSNO at 38 °C with constant stirring and shielded from light. Aliquots of 3% hydrogen peroxide are added to the solution at regular intervals to assess the impact of simultaneous NO generation with hydrogen peroxide oxidation.

5.3.6 Data Reporting and Analysis

Data is reported as the mean ± standard deviation (SD) of n = 3 replicate experiments. Statistical significance was determined using a two-tailed student's t-test or one-way ANOVA with post hoc Tukey HSD at a 95% confidence interval.

5.4 Results and Discussion

5.4.1 Composite Formulation Selection

In Chapter 4 relevant CuBTTri composite film parameters were examined. Mid-size ground MOF particles embedded within a polymer generated NO at greater rates than larger unprocessed particles and smaller highly processed particles. The ground MOF particles were incorporated into films with varying MOF loading (1, 5, 10 wt.%) and polyurethane concentration (1, 3, 5 w/v%). To select the optimal formulation for applying to a glucose biosensor as the outer polymer membrane, we need to consider the physical characteristics in addition to the NO generation capacity of the films. All nine formulations generated NO fluxes within the biological endothelial NO flux range (0.05–4.0 nmol cm^{-2} min^{-1}) necessary to reduce thrombosis formation on the artificial device surface. The highest NO flux was generated by the film with the highest MOF loading and polyurethane concentration, 10 wt.% MOF/5% PU, at 0.20 ± 0.02 nmol cm^{-2} min^{-1}. This flux was generated in experiments with a GSNO concentration on the high end of endogenous RSNO concentrations (nM–μM) but does not reach the high end of the natural endothelial flux range (4.0 nmol cm^{-2} min^{-1}). For this reason, we will initially narrow the selection to the formulations that generated the highest NO flux levels: 5% MOF/3% PU (0.13 ± 0.01 nmol cm^{-2} min^{-1}), 5% MOF/5% PU (0.12 ± 0.02 nmol cm^{-2} min^{-1}), 10% MOF/3% PU (0.136 ± 0.008 nmol cm^{-2} min^{-1}), and 10% MOF/5% PU (0.20 ± 0.02 nmol cm^{-2} min^{-1}) (Figure 5.2). Three of the four formulations (5% MOF/3% PU, 5% MOF/5% PU, and

10% MOF/3% PU) are not statistically different from each other, highlighting that other selection criteria must be considered. The selected formulations are comprised of 5 or 10 wt.% CuBTTri and 3 or 5 w/v% polyurethane. The physical characteristics of the formulation must meet certain standards to be an effective glucose sensor outer membrane. The primary functions of the membrane are to protect the sensor components under biological conditions and optimize glucose mass transfer to the electrode relative to oxygen.[27] Polyurethanes are often used as the semipermeable membrane for implantable glucose sensors due to their stability and oxygen permeability.[27,30,31] For a specific polyurethane formulation, glucose permeability is largely controlled by the thickness of the membrane—membranes that are too thin will increase the glucose to oxygen ratio and membranes that are too thick will reduce glucose diffusion, both resulting in diminished linearity and sensitivity. Both the 3% and 5% PU concentrations are conducive to the dip-coating or loop-coating methods frequently employed to coat the glucose sensor. But due to the notable increase in viscosity of the coating solution when increasing from 3% to 5% PU, the 5% formulations present a risk of fabricating a membrane that is too thick; whereas the 3% formulation benefits from the ability to add another layer if glucose permeability is too high with a single coating. For these reasons, we will further narrow our membrane selection to the two 3% PU formulations (5% MOF/3% PU and 10% MOF/3% PU).

The chemical and physical characteristics of the two remaining formulations are nearly identical aside from the MOF content. Selecting the formulation with the lower (5%) MOF content is the clear choice for two reasons. First, there is no benefit to increasing the MOF concentration if there is no increase in NO generation capacity. Second, greater additive concentrations in polymers increase the risk of delamination during implantation or removal of

the device due to the combined influence of the MOF and polymer on the physical properties of the coating (i.e., higher MOF loading imparts greater MOF character to the composite material).

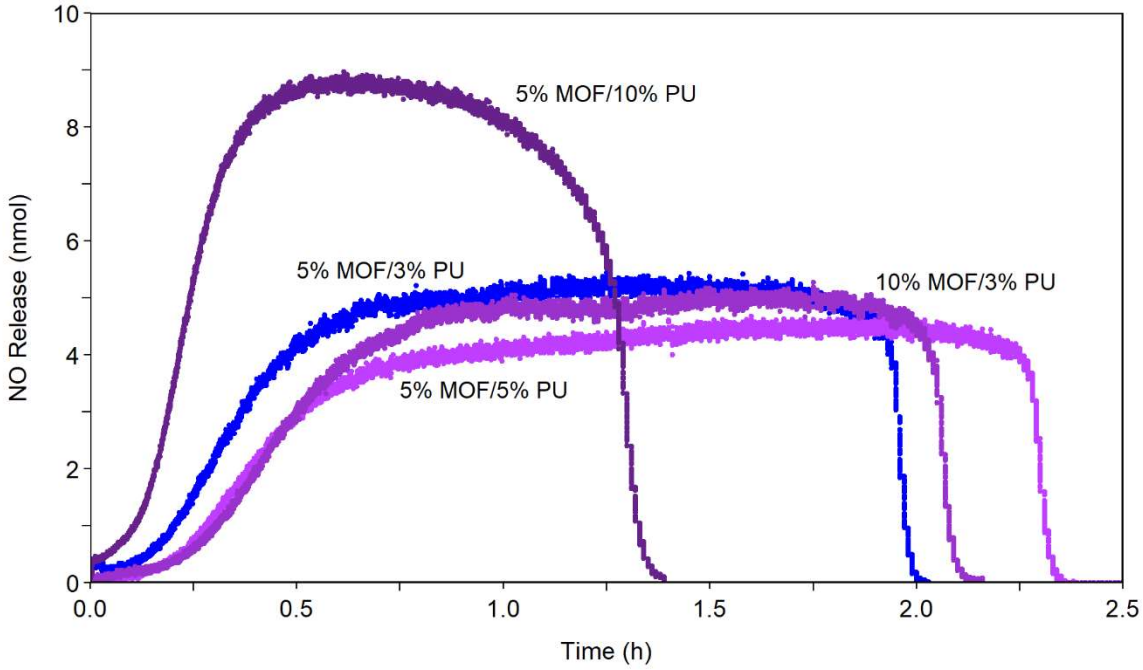

Figure 5.2. Representative NO generation profiles from the four formulations that generated the highest NO flux: 5% MOF/10% PU (dark purple), 5% MOF/3% PU (blue), 10% MOF/3% PU (medium purple), 5% MOF/5% PU (light purple). Experiments conducted using the NOA in ultrapure water with constant N_2 bubbling at 25 °C shielded from light with 10×10^{-6} M GSNO. Composites (1.2 cm diameter) fabricated with hand ground MOF particles.

The 5 wt.% CuBTTri/3 w/v% polyurethane composite formulation was selected for further testing. To ensure that this material would generate NO with varying GSNO concentrations mimicking endogenous conditions, the composite film was tested against GSNO concentrations an order of magnitude lower and higher than the original 10 μM concentration (Figure 5.3). We found that, at 100 μM GSNO, the flux was 24x greater than at 10 μM (3.0 ± 0.9 vs. 0.13 ± 0.01 01 nmol cm^{-2} min^{-1}). This result aligns well with the hypothesized GSNO concentration gradient model explored in Chapter 3. Based on that model we would expect a

greater driving force from the initial concentration gradient that exists between the hydrophilic polymer and the bulk reaction solution compared to the lower GSNO concentration, resulting in increased NO flux. Interestingly, at an order of magnitude lower, 1 μM GSNO, NO generation was not statistically different (0.15 ± 0.02 vs. 0.13 ± 0.01 nmol cm^{-2} min^{-1}) than at 10 μM. Further research is needed to parse this observation, but regardless, we found that the composite is capable of generating biologically-relevant levels of NO from GSNO concentrations over three orders of magnitude, an important consideration for real-world applications of this material.

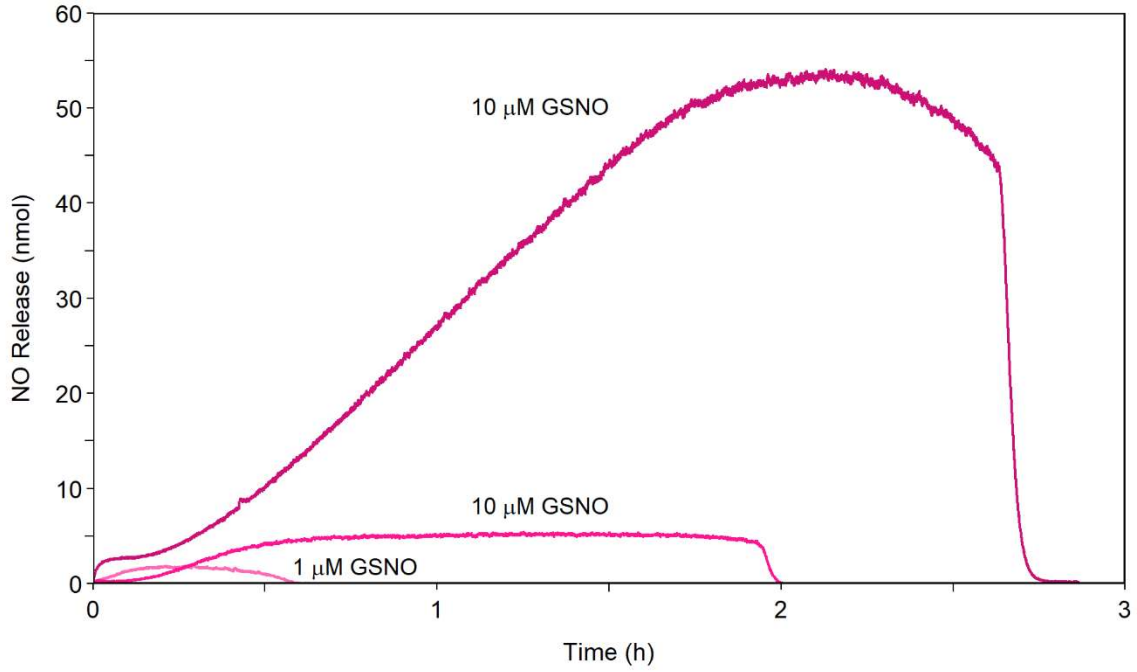

Figure 5.3. 5 wt.% CuBTTri/3 w/v% polyurethane film at 1, 10, and 100 μM GSNO.

5.4.2 Enzyme Compatibility with CuBTTri-Embedded Composite Material

After selecting the optimal composite formulation, it was important to determine if the presence of CuBTTri impacted the enzymatic oxidation of glucose. The method for this assessment was based on a colorimetric glucose sensor design by Dai.[29] The mechanism for

analysis is based on the formation and detection of prussian blue nanoparticles (PBNPs) at 706 nm. In an acidic medium PBNPs can be formed from ferric chloride ($FeCl_3$) and potassium ferricyanide ($K_3Fe(CN)_6$) in the presence of a oxidizing agent (e.g., hydrogen peroxide) to generate potassium ferrous ferricyanide ($KFe[Fe(CN)_6]$) nanoparticles (λ_{max} = 706 nm). In this system, two concurrent pathways are hypothesized to generate PBNPs (Figure 5.4). The first pathway is analogous to the mechanism used to measure glucose in first-generation glucose biosensors: the enzyme-mediated oxidation of glucose and oxygen generates hydrogen peroxide which reduces Fe^{3+} to Fe^{2+} to react with $K_3Fe(CN)_6$ to generate $KFe[Fe(CN)_6]$ nanoparticles. The second pathway is analogous to the mechanism to measure glucose in second-generation glucose biosensors: the reduced form of glucose oxidase oxidizes Fe^{3+} in $K_3Fe(CN)_6$ which reacts with Fe^{3+} to generate $KFe[Fe(CN)_6]$ nanoparticles. A calibration curve was generated (Figure 5.5) and the technique was found the have a wide linear range over three orders of magnitude (0.000977–1.00 mM glucose) and good sensitivity to changes in glucose concentration (0.40 Abs/mM). To examine the impact of CuBTTri on glucose oxidase activity, a small sample of a CuBTTri composite film was submerged in the reaction solution and removed just prior to analysis. The results are presented in Table 5.1. We see that the absorbances for the two higher glucose concentrations, 0.0313 and 0.125 mM, with and without the composite film were not statistically significant. The lower concentration (0.00781 mM glucose) had a statistically significant change in absorbance, experiencing an *increase* in absorbance. When comparing the three sets of data, we see the absorbances for all of the film-containing solutions was higher (even if not significantly) than the control. I think that the experimental design of these tests is the cause of this discrepancy, rather than an indication of *enhanced* enzyme activity and PBNP formation. The composite films were not pre-soaked prior to the experiment, and it was previously

determined that they absorb water to their full capacity (100-150% by weight) within 5 minutes of being in an aqueous environment. These experiments were conducted over the course of 10 minutes, which is enough time for them to absorb some volume of the solution. Considering the total solution volume was 110 µL and that the PBNPs are solid particles that sink to the bottom of the well, it is reasonable to hypothesize that the volume of solution absorbed by the composite films over the course of the experiment is enough to cause an apparent increase in absorbance, especially at very low glucose concentrations where PBNP formation is much lower. With these facts in mind, it is reasonable to conclude that the presence of CuBTTri in the film did not impact the performance of the enzyme, though additional experiments with pre-soaked films are needed for complete confidence in this result.

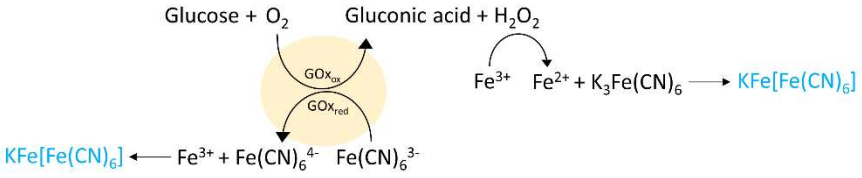

Figure 5.4. Proposed dual mechanism of prussian blue nanoparticle (PBNP) formation by glucose oxidase for spectrophotometric detection at 706 nm.

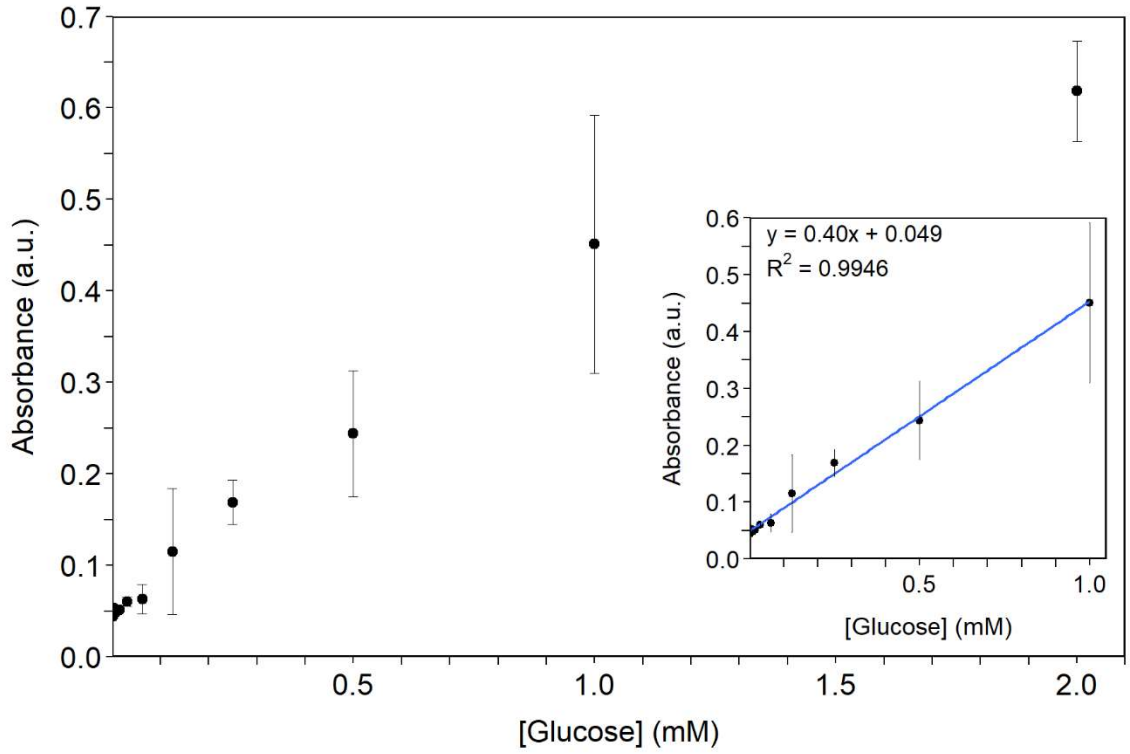

Figure 5.5. Blank-corrected absorbance measurements at 706 nm of solutions containing 0.68 mM $FeCl_3$, 0.68 mM $K_3Fe(CN)_6$, 0.050 mg mL^{-1} GOx, and 0.000977, 0.00195, 0.00391, 0.00781, 0.0156, 0.0313, 0.0625, 0.125, 0.250, 0.500, 1.00, and 2.00 mM glucose in 50 mM MES buffer (pH 3) after 10 minutes. LOD = 0.039; LOQ = 0.047, linear range = 0.000977–1.00 mM glucose, sensitivity = 0.40 Abs/mM.

Table 5.1. Performance of GOx enzyme in the presence of CuBTTri composite.

System[a]	Absorbance[b] (a.u.)	Statistical Significance
0.125 mM Glucose	0.12 ± 0.07	$p > 0.05$
0.125 mM Glucose + CuBTTri Composite	0.13 ± 0.01	
0.0313 mM Glucose	0.060 ± 0.005	$p > 0.05$
0.0313 mM Glucose + CuB TTri Composite	0.082 ± 0.008	
0.00781 mM Glucose	0.048 ± 0.003	$p < 0.05$
0.00781 mM Glucose + CuBTTri Composite	0.071 ± 0.003	

[a]Solutions contained 0.68 mM $FeCl_3$, 0.68 mM $K_3Fe(CN)_6$, 0.050 mg mL^{-1} GOx in 50 mM MES buffer (pH 3). Reaction proceeded for 15 min.
[b]Measured at 706 nm (n = 3).

5.4.3 Amperometric Detection

Ongoing research is evaluating the performance of needle-type sensors coated with a polyurethane membrane compared to the CuBTTri composite membrane for the detection of hydrogen peroxide in the presence of GSNO and the detection of hydrogen peroxide generated by the enzymatic reaction with glucose. In a first set of experiments, amperometric detection of hydrogen peroxide was quantified for control and MOF-coated sensors (Fig. 5.6). Both sensors (n = 3) displayed good linearity (R^2 = 0.9797 and 0.9953) over a wide glucose concentration range (1-6 mM). These results, in combination with the spectroscopy data, suggest that the presence of CuBTTri will not impede sensor function. Ongoing research involves testing the sensors with glucose over clinically-relevant ranges (1-20 mM).

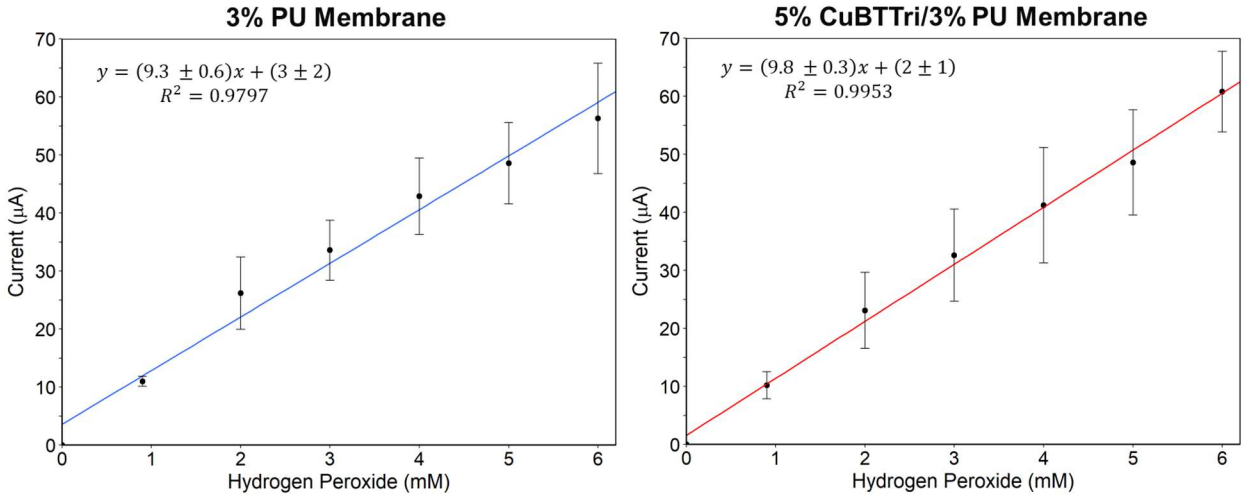

Figure 5.6. Calibration curves for needle-type glucose sensors with A) 3% PU (control) and B) 5% CuBTTri/3% PU outer polymer membranes.

5.5 Conclusions

In summary, the optimal CuBTTri/polyurethane composite material was selected to be implemented as the outer polymer membrane of an implantable enzymatic glucose biosensor.

We showed that this film is capable of generating NO from glucose concentrations over three orders of magnitude at the rate of biological endothelial levels needed to prevent thrombus formation. We demonstrated that the presence of a CuBTTri composite film did not inhibit the ability glucose oxidase function through a colorimetric reaction of the formation of PBNPs. We demonstrated the application of this film on an electrochemical glucose biosensor for the detection of hydrogen peroxide. Taken together, these data are promising for the application of MOF-based outer polymer membranes in the development of more biocompatible blood-contacting glucose sensors.

CHAPTER 5

REFERENCES

(1) World Health Organization. Global Report on Diabetes; Geneva, Switzerland, **2016**.

(2) Chen, C.; Zhao, X.-L.; Li, Z.-H.; Zhu, Z.-G.; Qian, S.-H.; Flewitt, A. Current and Emerging Technology for Continuous Glucose Monitoring. *Sensors* **2017**, *17* (1), 182.

(3) Rong, G.; Corrie, S. R.; Clark, H. A. In Vivo Biosensing: Progress and Perspectives. *ACS Sensors* **2017**, *2* (3), 327–338.

(4) Harding, J. L.; Reynolds, M. M. Combating Medical Device Fouling. *Trends Biotechnol.* **2014**, *32* (3), 140–146.

(5) Soto, R. J.; Hall, J. R.; Brown, M. D.; Taylor, J. B.; Schoenfisch, M. H. In Vivo Chemical Sensors: Role of Biocompatibility on Performance and Utility. *Anal. Chem.* **2017**, *89* (1), 276–299.

(6) Zhang, L.; Cao, Z.; Bai, T.; Carr, L.; Ella-Menye, J. R.; Irvin, C.; Ratner, B. D.; Jiang, S. Zwitterionic Hydrogels Implanted in Mice Resist the Foreign-Body Reaction. Nat. *Biotechnol.* **2013**, *31* (6), 553–556.

(7) Koschwanez, H. E.; Reichert, W. M.; Klitzman, B. Intravital Microscopy Evaluation of Angiogenesis and Its Effects on Glucose Sensor Performance. *J. Biomed. Mater. Res. Part A* **2010**, *93* (4), 1348–1357.

(8) Koschwanez, H. E.; Yap, F. Y.; Klitzman, B.; Reichert, W. M. In Vitro and in Vivo Characterization of Porous Poly-L-Lactic Acid Coatings for Subcutaneously Implanted Glucose Sensors. J. Biomed. *Mater. Res. Part A* **2008**, *87* (3), 792–807.

(9) Agarwal, S.; Wendorff, J. H.; Greiner, A. Use of Electrospinning Technique for Biomedical Applications. *Polymer* **2008**, *49* (26), 5603–5621.

(10) Wang, N.; Burugapalli, K.; Song, W.; Halls, J.; Moussy, F.; Ray, A.; Zheng, Y. Electrospun Fibro-Porous Polyurethane Coatings for Implantable Glucose Biosensors. *Biomaterials* **2013**, *34* (4), 888–901.

(11) Avula, M.; Jones, D.; Rao, A. N.; McClain, D.; McGill, L. D.; Grainger, D. W.; Solzbacher, F. Local Release of Masitinib Alters in Vivo Implantable Continuous Glucose Sensor Performance. *Biosens. Bioelectron.* **2016**, *77*, 149–156.

(12) Avula, M. N.; Rao, A. N.; McGill, L. D.; Grainger, D. W.; Solzbacher, F. Foreign Body Response to Subcutaneous Biomaterial Implants in a Mast Cell-Deficient Kitw-Sh Murine Model. *Acta Biomater.* **2014**, *10* (5), 1856–1863.

(13) Ward, W. K.; Hansen, J. C.; Massoud, R. G.; Engle, J. M.; Takeno, M. M.; Hauch, K. D. Controlled Release of Dexamethasone from Subcutaneouslyimplanted Biosensors in Pigs: Localized Anti-Inflammatory Benefit without Systemic Effects. *J. Biomed. Mater. Res. Part A* **2010**, *94* (1), 280–287.

(14) Vallejo-Heligon, S. G.; Brown, N. L.; Reichert, W. M.; Klitzman, B. Porous, Dexamethasone-Loaded Polyurethane Coatings Extend Performance Window of Implantable Glucose Sensors in Vivo. *Acta Biomater.* **2016**, *30*, 106–115.

(15) Klueh, U.; Kaur, M.; Montrose, D. C.; Kreutzer, D. L. Infammation and Glucose Sensors: Use of Dexamethasone to Extend Glucose Sensor Function and Life Span in Vivo. *J. Diabetes Sci. Technol.* **2007**, *1* (4), 496–504.

(16) Gifford, R.; Batchelor, M. M.; Lee, Y.; Gokulrangan, G.; Meyerhoff, M. E.; Wilson, G. S. Mediation of in Vivo Glucose Sensor Inflammatory Response via Nitric Oxide Release. *J. Biomed. Mater. Res. Part A* **2005**, *75* (4), 755–766.

(17) Hetrick, E. M.; Prichard, H. L.; Klitzman, B.; Schoenfisch, M. H. Reduced Foreign Body Response at Nitric Oxide-Releasing Subcutaneous Implants. *Biomaterials* **2007**, *28* (31), 4571–4580.

(18) Soto, R. J.; Privett, B. J.; Schoenfisch, M. H. In Vivo Analytical Performance of Nitric Oxide-Releasing Glucose Biosensors. *Anal. Chem.* **2014**, *86* (14), 7141–7149.

(19) Riccio, D. A.; Schoenfisch, M. H. Nitric Oxide Release Part I. Macromolecular Scaffolds. *Chem. Soc. Rev.* **2012**, *41* (10), 3731–3741.

(20) Walford, G.; Loscalzo, J. Nitric Oxide in Vascular Biology. *J. Thromb. Haemost.* **2003**, *1* (10), 2112–2118.

(21) Cha, K. H.; Wang, X.; Meyerhoff, M. E. Nitric Oxide Release for Improving Performance of Implantable Chemical Sensors – A Review. *Appl. Mater. Today* **2017**, *9*, 589–597.

(22) Frost, M.; Meyerhoff, M. E. In Vivo Chemical Sensors: Tackling Biocompatibility. *Anal. Chem.* **2006**, *78* (21), 7370–7377.

(23) Wo, Y.; Brisbois, E. J.; Bartlett, R. H.; Meyerhoff, M. E. Recent Advances in Thromboresistant and Antimicrobial Polymers for Biomedical Applications: Just Say Yes to Nitric Oxide (NO). *Biomater. Sci.* **2016**, *4* (8), 1161–1183.

(24) Yan, Q.; Major, T. C.; Bartlett, R. H.; Meyerhoff, M. E. Intravascular Glucose/Lactate Sensors Prepared with Nitric Oxide Releasing Poly(Lactide-Co-Glycolide)-Based

Coatings for Enhanced Biocompatibility. *Biosens. Bioelectron.* **2011**, *26* (11), 4276–4282.

(25) Wu, Y.; Meyerhoff, M. E. Nitric Oxide-Releasing/Generating Polymers for the Development of Implantable Chemical Sensors with Enhanced Biocompatibility. *Talanta* **2008**, *75* (3), 642–650.

(26) Puiu, S. C.; Zhou, Z.; White, C. C.; Neubauer, L. J.; Zhang, Z.; Lange, L. E.; Mansfield, J. A.; Meyerhoff, M. E.; Reynolds, M. M. Metal Ion-Mediated Nitric Oxide Generation from Polyurethanes via Covalently Linked Copper(II)-Cyclen Moieties. *J. Biomed. Mater. Res. Part B Appl. Biomater.* **2009**, *91B* (1), 203–212.

(27) Bindra, D. S.; Zhang, Y.; Wilson, G. S.; Sternberg, R.; Thévenot, D. R.; Moatti, D.; Reach, G. Design and in Vitro Studies of a Needle-Type Glucose Sensor for Subcutaneous Monitoring. *Anal. Chem.* **1991**, *63* (17), 1692–1696.

(28) Zhang, Y.; Hu, Y.; Wilson, G. S.; Moatti-Sirat, D.; Poitout, V.; Reach, G. Elimination of the Acetaminophen Interference in an Implantable Glucose Sensor. *Anal. Chem.* **1994**, *66* (7), 1183–1188.

(29) Dai, H.; Li, Y.; Zhang, Q.; Fu, Y.; Li, Y. A Colorimetric Biosensor Based on Enzyme-Catalysis-Induced Production of Inorganic Nanoparticles for Sensitive Detection of Glucose in White Grape Wine. *RSC Adv.* **2018**, *8* (59), 33960–33967.

(30) Davis, F. J.; Mitchell, G. R. Polyurethane Based Materials with Applications in Medical Devices. *In Bio-Materials and Prototyping Applications in Medicine*; **2008**; pp 27–48.

(31) Kulkarni, T.; Slaughter, G. Application of Semipermeable Membranes in Glucose Biosensing. *Membranes* **2016**, *6* (4).

CHAPTER 6

THE EFFECTS OF COPPER AND TWENTY OTHER TRANSITION AND POST-TRANSITION METAL IONS ON NITRIC OXIDE GENERATION FROM *S*-NITROSOGLUTATHIONE[3]

6.1 Overview

Though metal ion-promoted NO release from RSNOs is promising strategy for the development of NO-generating materials, the majority of studies focus on copper, and few have surveyed the ability of other common metal ions to produce this effect. Using NO-selective chemiluminescence-based detection, NO generation from GSNO by twenty transition and post-transition metal ions was evaluated to identify potential alternative metal ions for the fabrication of biocompatible medical device materials. This chapter addresses the research question: Are there other metal ions capable of generating NO from endogenous sources?

6.2 Introduction

S-Nitrosothiols (RSNOs) occur naturally in human biochemistry, with apparent blood concentrations typically reported to fall within the nM to μM range.[1] Endogenous RSNOs are generally derived from *S*-nitrosation of cysteine residues in proteins such as *S*-nitrosoalbumin or low-molecular weight peptides such as *S*-nitrosoglutathione (GSNO). While the physiological production and function of RSNOs remains the subject of discussion, these unique compounds have attracted considerable interest from a pharmacological perspective as sources of the diatomic radical nitric oxide (NO). NO bioactivity is currently recognized to include

[3] This chapter was reproduced in part from:
Lutzke, A.; Melvin, A. C.; Neufeld, M. J.; Allison, C. L.; Reynolds, M. M. Nitric Oxide Generation from S-Nitrosoglutathione: New Activity of Indium and a Survey of Metal Ion Effects. *Nitric Oxide - Biol. Chem.* **2019**, *84* (October 2018), 16–21.Copyright 2019 Elsevier Inc. https://doi.org/10.1016/j.niox.2019.01.005.

vasodilation, maintenance of the anticoagulative properties of the vasculature, neurotransmission, wound-healing, and the immune response.[2,3] RSNOs are typically observed to possess limited solution-phase stability and decompose to form NO and disulfide through thermal, photolytic, and metal ion-promoted pathways.[4] The most striking example of the latter pathway is observed in the case of Cu^{+}, which has been demonstrated to readily catalyze RSNO decomposition.[5] Similarly, Fe^{2+} has been found to induce the NO-forming decomposition of RSNOs in a limited manner.[6] The ability of RSNOs to produce NO in this fashion has led the biomaterials community to routinely propose the use of various metal or metal ion-based biointerfacial materials to generate therapeutic NO directly from endogenous sources, primarily through contact with blood.[7-20] Despite considerable interest in the use of metals or metal ions to trigger NO formation from RSNOs, few studies have specifically surveyed the ability of common transition and post-transition metal ions to produce this effect. Prior reports often confined their analysis to a limited range of period 4 d-block metals (*e.g.*, Cr, Mn, Fe, Co, Ni, Cu, Zn) and utilized techniques such as UV-Vis absorption spectroscopy that monitor RSNO decomposition rather than NO formation.[2,4,11] In this study, NO-selective chemiluminescence-based detection was used to evaluate the effect of various metal ions on GSNO, a model RSNO with well-characterized chemical behavior.

6.3 Materials and Methods

6.3.1 Materials

Cobalt(II) chloride hexahydrate (>98%), lead(II) nitrate (≥99.0%), and nickel(II) nitrate hexahydrate (99%) were purchased from Acros Organics (Morris Plains, NJ, USA). Chromium(III) chloride hexahydrate (98%), indium(I) chloride (99.995%), indium(III) chloride (99.999%), indium(I) iodide (99.998%), indium powder (-325 mesh, 99.999%), mercury(II)

acetate (98%), silver(I) nitrate (99.995%), tin(II) chloride dihydrate (98%), vanadium(III) chloride (99%), and zirconium dichloride oxide hydrate (99.9%) were purchased from Alfa Aesar (Ward Hill, MA, USA). Copper(II) chloride dihydrate (99%) was purchased from EMD Chemicals (Gibbstown, NJ, USA). Iron(III) chloride hexahydrate (≥97%) was purchased from Mallinckrodt (St. Louis, MO, USA). Iron(II) chloride tetrahydrate (>99%), manganese(II) chloride tetrahydrate (>99%), and zinc(II) chloride (>97%) were purchased from Fisher Scientific (Waltham, MA, USA). *N*-Acetyl-D-penicillamine (≥ 99.0%), aluminum nitrate nonahydrate (≥98%), gold(III) chloride trihydrate (≥49.0% Au), hafnium(IV) chloride tetrahydrofuran complex (98%), indium(II) chloride (99.9%), neocuproine (≥98%), scandium(III) triflate (99%), sodium nitrite (99.5%), sodium tetrachloropalladate(II) (98%), and sodium tetrachloroplatinate(II) hydrate (≤49.8% Pt) were purchased from Sigma-Aldrich (St. Louis, MO, USA). Nalgene surfactant-free cellulose acetate syringe filters (0.2 μm) were obtained from Thermo Scientific (Waltham, MA, USA). Reduced glutathione was purchased from VWR (Radnor, PA, USA). All chemicals were used as received. Hygroscopic compounds were stored in a dessicator. Ultra-high-purity (UHP) nitrogen (N_2) and oxygen (O_2) gases were purchased from Airgas (Denver, CO, USA). Nitric oxide (NO; 43.6 ppm NO, balance N_2) calibration gas was supplied by Air Liquide (Houston, TX, USA). Deionized water (18.2 MΩ·cm) was supplied by a Millipore Direct-Q water purification system (EMD Millipore, Billerica, MA).

6.3.2 General Analytical Techniques

Nuclear magnetic resonance (NMR) spectra were acquired using a Bruker Avance Neo 400 NMR spectrometer (Billerica, MA, USA). Ultraviolet-visible (UV-Vis) spectroscopy was performed using a Nicolet Evolution 300 spectrophotometer (Thermo Electron Corp., Madison,

WI, USA) and quartz cuvettes. Mass spectra were acquired using an Agilent 6224 time-of-flight mass spectrometer (TOF-MS) equipped with a dual electrospray ion source in negative ion mode.

6.3.3 Measurement of Nitric Oxide (NO) Production

Nitric oxide (NO) release from *S*-nitrosoglutathione (GSNO) was quantified using chemiluminescence-based Sievers NO analyzers (NOA 280i) (Zysense, Weddington, NC, USA). The instruments were operated using UHP N_2 gas to transport NO from a custom external measurement vessel (200 mL min^{-1} flow rate) to the internal reaction cell (4-7 Torr, -12.0 °C) for quantification by chemiluminescent reaction with ozone (produced internally from O_2 gas supplied at 5.8-6.2 psig). Prior to use, the instruments were calibrated using UHP N_2 (0 ppm NO) and 43.6 ppm NO/N_2. During NO production experiments, data was recorded as a function of time (s) in ppb/ppm values that were subsequently converted to moles of NO using instrument-specific calibration constants (mol NO ppb^{-1} s^{-1}). These calibration constants were obtained from the reduction of known quantities of sodium nitrite to NO by potassium iodide in dilute sulfuric acid, and were verified by the NO-forming decomposition of known quantities of GSNO in the presence of copper(II) chloride. In standard experiments, soluble compounds were dissolved in Millipore water (18.2 MΩ·cm) and transferred to the external measurement vessel, where N_2 was bubbled through the solution to remove dissolved O_2. GSNO (dissolved in Millipore water) was then added to the vessel to produce an initial concentration of 2.50×10^{-4} M GSNO (1.25×10^{-6} mol RSNO) and 2.50×10^{-5} M of the soluble compound (1.25×10^{-7} mol overall) in a total solution volume of 5.00 mL. Real-time production of NO was then recorded at measurement intervals of 1 s for either 0.5 or 1.0 h. Continuous bubbling of N_2 was used to ensure the rapid displacement of NO from the solution. In cases where the element or compound was insoluble, 1

$\times 10^{-5}$ mol of the substance was added to the measurement vessel as a solid and suspended in a total solution volume of 5.00 mL of Millipore water containing 2.50×10^{-4} M GSNO (1.25×10^{-6} mol GSNO). Select experiments were repeated at a lower GSNO concentration of 2.50×10^{-5} M, following an otherwise identical protocol. Reactions were unbuffered to avoid effects from buffer solutes, and the pH was generally governed by the presence of GSNO at 2.50×10^{-4} M (*ca.* pH 4) or 2.50×10^{-5} (*ca*. pH 5) concentrations. Between experiments, all glassware was treated with a saturated aqueous solution of EDTA-Na_2 and extensively washed with Millipore water.

6.3.4 S-*Nitrosoglutathione (GSNO) Synthesis*

In a typical synthesis, the compound was prepared following an adaptation of the method reported by Hart.[12] Glutathione (GSH; 1.53 g, 5 mmol) was suspended in 4 mL of Millipore water and dissolved by the addition of 2.5 mL of 2 M hydrochloric acid. This mixture was subsequently cooled to 0 °C using an ice bath. Separately, sodium nitrite (0.345 g, 5 mmol) was dissolved in 4 mL of Millipore water and added to the stirring solution of GSH. The mixture rapidly developed a red-pink color that was accompanied by the formation of a pink precipitate, and was stirred in the absence of light for 40 min. After this period, 10 mL of acetone was added to the reaction to promote further precipitation of GSNO. The mixture was allowed to stir for 10 min, then the precipitate was isolated by vacuum filtration. The precipitate was washed with 3 × 5 mL of ice-cold Millipore water, 3 × 10 mL of acetone, and 3 × 10 mL of diethyl ether. The precipitate was placed under vacuum for several hours to remove residual solvent and yielded GSNO (1.28 g, 76%) as a fine pink powder. ^{1}H NMR (400 MHz, D_2O): δ 4.64 (t, cysteinyl -CH-, 1H), 4.17-3.90 (m, cysteinyl -CH_2-, 2H), 3.92 (s, glycinyl -CH_2-, 2H), 3.76 (t, glutamyl -CH-,

1H), 2.41 (t, glutamyl -CH_2CO-, 2H), 2.16-2.00 ppm (m, glutamyl -CH_2-, 2H). UV-Vis (H_2O): λ 335 (RSNO π → π*), 545 nm (RSNO n → π*) (Fig. 6.1 and 6.2).

Figure 6.1. ^{1}H NMR spectrum of GSNO. Spectrum acquired in D_2O at 25 °C.

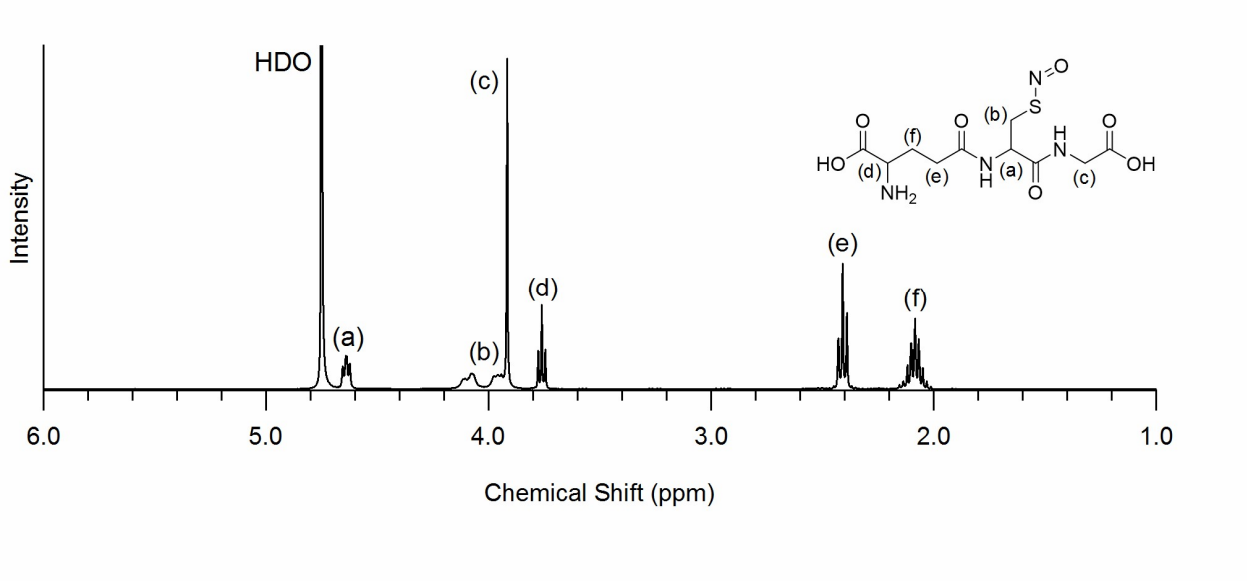

Figure 6.2. UV-Vis spectrum of GSNO (1.5×10^{-3} M). Spectrum acquired in water.

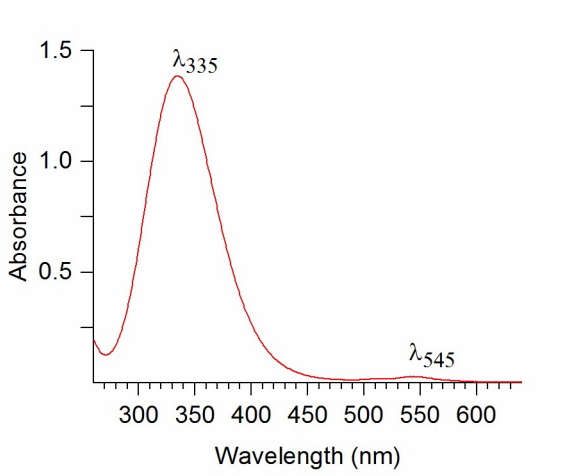

Figure 6.3. ^{1}H NMR spectrum of *S*-nitroso-*N*-acetylpenicillamine (SNAP). Spectrum acquired in CD_3OD at 25 °C.

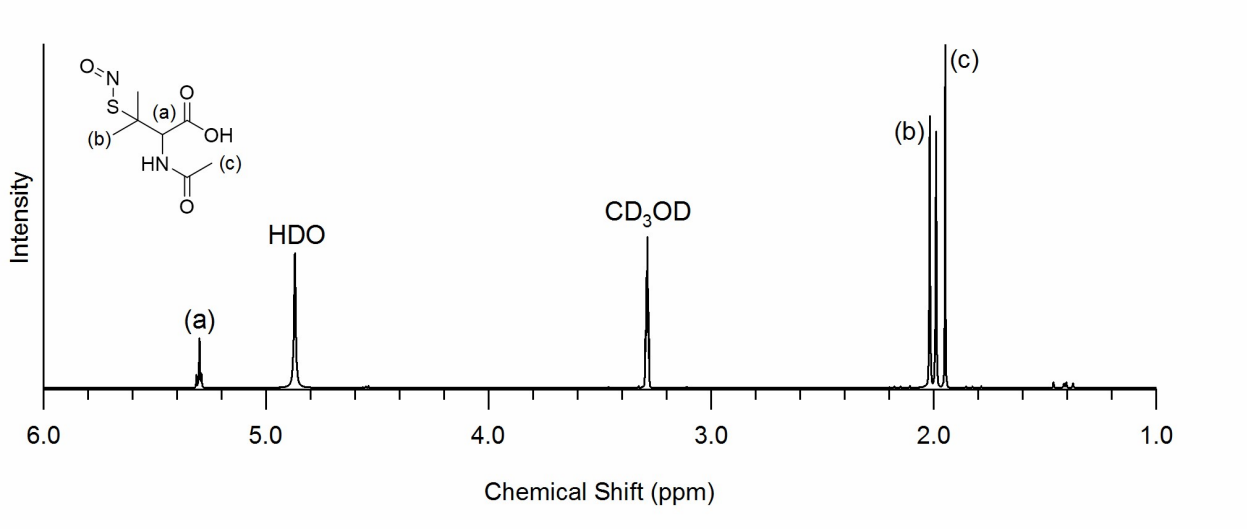

Figure 6.4. UV-Vis spectrum of *S*-nitroso-*N*-acetylpenicillamine (SNAP; 1.5×10^{-3} M.). Spectrum acquired in water.

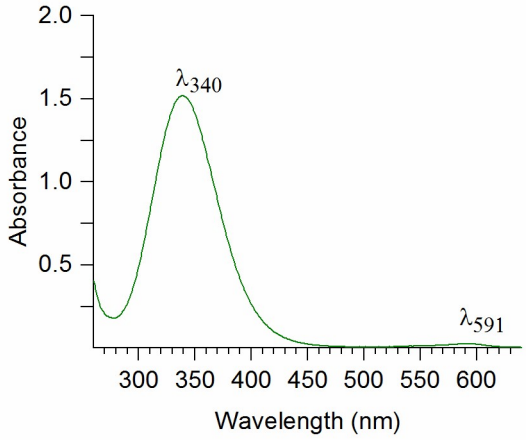

6.3.5 S-Nitroso-N-acetylpenicillamine (SNAP) Synthesis

In a typical synthesis, the compound was prepared following an adaptation of the protocol given by Field *et al.*[13] *N*-Acetyl-D-penicillamine (NAP; 0.956 g, 5 mmol) was suspended in an ice-cold solution of 1 M hydrochloric acid (10 mL) and methanol (10 mL). Separately, sodium nitrite (0.690 g, 10 mmol) was dissolved in 5 mL of Millipore water and added to the solution of NAP. The mixture developed a green color and was stirred for 35 min in

the absence of light. After this period, the green precipitate was isolated by vacuum filtration and washed with 3 × 10 mL of ice-cold water. The solid was placed under vacuum for several hours to remove residual solvent and yielded SNAP (0.625 g, 57%) as a fine green powder. ^{1}H NMR (400 MHz, CD_3OD): δ 5.30 (m, -CH-, 1H), 2.02 and 1.99 (s, $-CH_3$, 6H), 1.95 ppm (s, $-COCH_3$, 3H). UV-Vis (H_2O): λ 340 (RSNO π → π*), 591 nm (RSNO n → π*) (Fig. 6.3 and 6.4).

6.3.6 Data Reporting and Analysis

Data reported as mean ± standard deviation of a minimum of three replicate experiments. The ability of tested metals to promote elevated NO release from *S*-nitrosothiol substrates (GSNO or SNAP) was determined by comparison of total NO release (mol) over the measurement period (0.5-1.0 h) with the baseline NO release of GSNO or SNAP in the absence of metal ions, using the two-tailed Student's t-test ($p < 0.05$).

6.4 Results and Discussion

Previous studies concerning the ability of metal ions to interact with RSNOs have utilized varying substrates and analytical approaches that have occasionally resulted in conflicting reports (Fig. 6.5). The use of a uniform experimental approach offers the clear benefit of permitting direct comparisons of relative metal ion activity under a specific set of measurement conditions. In this work, we sought to directly measure the metal-promoted release of gaseous NO from an aqueous 25 or 250 μM RSNO solution using NO-selective chemiluminescence-based detection. This technique requires anaerobic conditions to avoid consumption of NO prior to detection, which also prevents rapid oxidation of sensitive metal species by O_2. GSNO

Figure 6.5. Periodic table illustrating elements (whether in metallic, ionic, or covalently-bound forms) specifically associated with direct *S*-nitrosothiol decomposition. Elements highlighted in blue are generally understood to not exhibit any ability to accelerate *S*-nitrosothiol decomposition.[4] Elements highlighted in yellow are known to interact with *S*-nitrosothiols in a unique manner, as in the case of complex formation with ruthenium,[14] osmium,[15] or iridium[16]

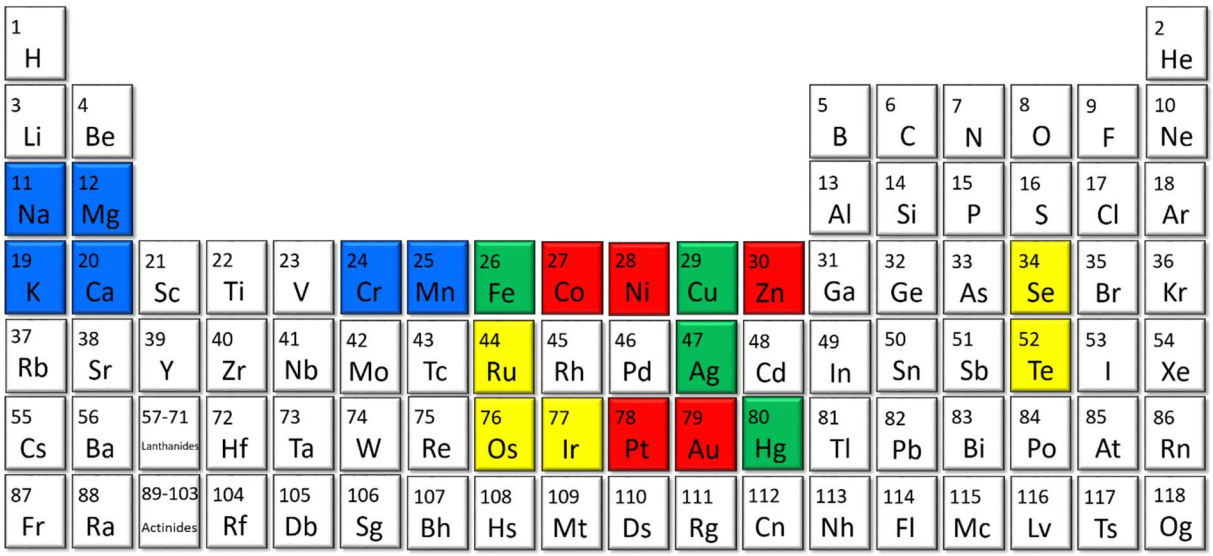

compounds or chalcogenide exchange with organoselenium[17] or organotellurium[18] species. Elements highlighted in green are generally understood to promote *S*-nitrosothiol decomposition through either the formation of NO (*e.g.*, copper and ferrous ions),[14] or by hydrolysis to nitrous acid.[19] Elements highlighted in red are the subject of conflicting reports[4,20,21] or few examples of their use have been published.[22,23]

represented a logical choice of RSNO substrate due to its biological relevance, well-characterized chemical behavior, and stability. We found that the real-time measurement of NO formation over 0.5 h was sufficient to identify cases in which the addition of particular metal compounds resulted in elevated NO production relative to control experiments. Selected experiments were continued for 1 h to permit examination of NO release over a longer duration. All metal ions were evaluated at a GSNO concentration of 250 μM, and those species that promoted substantial NO production in the absence of previously hypothesized nitrous acid (HNO_2)-forming activity were further tested at 25 μM. The results of this survey are summarized in Table 6.1 as cumulative NO production, and are compared with the typical quantity of NO released from GSNO at 25 °C in the absence of light. To interpret the potential for other trace metals to influence the experimental results, ICP-AES was used to determine the concentration of possible contaminants. Due to the potency of Cu species in liberating NO from GSNO, the

presence of this metal as a trace contaminant in other experiments is given particular attention in tabular form and presented in Table 6.2. We observed that the addition of 25 μM Cu^{2+} to a 250 μM anaerobic solution of GSNO predictably induces a greater than 100-fold increase in the total quantity of NO released over the 1 h measurement period. As described elsewhere, the reaction is believed to involve reduction of Cu^{2+} to Cu^{+} by trace thiol, and it is this reduced metal species that initiates catalytic decomposition of the RSNO through a mechanism that has yet to be fully elucidated.[5] At a lower GSNO concentration of 25 μM, the efficiency of the reaction is significantly improved, resulting in both a greater 1 h NO yield (48% compared with 7.4%), and a higher cumulative NO recovery (120 ± 5 nmol compared with 92.4 ± 2.2 nmol) (Fig. 6.6). This outcome can be explained by a decrease in the ratio of dissolved Cu to substrate at the higher GSNO concentration, as well as binding of Cu^{+}/Cu^{2+} by GSNO or disulfide that leads to inhibition of catalytic activity.[24,25] Other processes such as autocatalysis and radical recombination are also hypothesized to influence RSNO decomposition in a concentration-dependent manner.[26] The susceptibility of GSNO solutions to decomposition after the addition of Cu^{2+} is decreased under aerobic conditions, where oxidation of catalytically-active Cu^{+} inhibits the reaction.[5] In contrast with prior reports from Williams *et al.* that describe Fe^{3+} as inert with respect to RSNO decomposition, we find that both Fe^{2+} (Fig. 6.7) and Fe^{3+} detectably elevated the rate of NO production from GSNO under deoxygenated conditions. These effects were far less dramatic than in the case of Cu, and the apparent activity of Fe^{3+} may simply arise from reduction to Fe^{2+} by trace thiol in a manner analogous to Cu^{2+}/Cu^{+}.[6] Among d- and p-block

Table 6.1 Metal-promoted nitric oxide release from *S*-nitrosoglutathione

Compound[a]	Time (h)	NO (nmol)[b] 250 μM	NO (nmol)[b,d] 25 μM
None (control)	0.5	0.57 ± 0.14	*nt*
None (control)	1.0	0.81 ± 0.11	0.16 ± 0.15
$Al(NO_3)_3$	0.5	0.78 ± 0.06	*nt*
$CrCl_3$	0.5	0.57 ± 0.10	*nt*
$CoCl_2$	0.5	1.43 ± 0.19[c]	*nt*
$CuCl_2$	1.0	92.4 ± 2.2[c]	120 ± 5
$AuCl_3$	1.0	15.2 ± 0.2[c]	3.67 ± 0.69
$HfCl_4$	1.0	3.40 ± 0.30[c]	*nt*
In (metallic)	0.5	0.73 ± 0.07	*nt*
InCl	1.0	57.9 ± 6.7[c]	18.1 ± 0.7
$InCl_2$	1.0	26.1 ± 3.0[c]	15.1 ± 3.3
$InCl_3$	0.5	0.63 ± 0.07	*nt*
InI	1.0	15.7 ± 0.7[c]	28.9 ± 4.5
$FeCl_2$	1.0	4.61 ± 0.28[c]	0.87 ± 0.11
$FeCl_3$	0.5	1.58 ± 0.11[c]	*nt*
$Pb(NO_3)_2$	0.5	0.59 ± 0.04	*nt*
$MnCl_2$	0.5	0.99 ± 0.07[c]	*nt*
$Hg(CH_3CO_2)_2$	1.0	6.52 ± 0.12[c]	*nt*
$Ni(NO_3)_2$	0.5	0.82 ± 0.06[c]	*nt*
$Sc(SO_3CF_3)_3$	0.5	0.70 ± 0.10	*nt*
$AgNO_3$	0.5	1.12 ± 0.05[c]	*nt*
Na_2PdCl_4	1.0	19.8 ± 1.2[c]	6.40 ± 0.18
Na_2PtCl_4	1.0	14.0 ± 0.6[c]	4.18 ± 0.38
$SnCl_2$	1.0	4.39 ± 0.27[c]	*nt*
VCl_3	1.0	20.6 ± 0.3[c]	*nt*
$ZnCl_2$	0.5	0.75 ± 0.04	*nt*
$ZrOCl_2$	1.0	6.48 ± 0.12[c]	0.78 ± 0.04

[e] Soluble compounds dissolved at a concentration of 25 μM. Insoluble compounds added as solids (10 μmol).

[f] Cumulative NO release over the indicated time. Data reported as mean ± SD of $n \geq 3$ replicate measurements.

[g] Cumulative NO release significantly different ($p < 0.05$) from control experiment by two-tailed Student's t-test.

[h] Metal ions not tested at 25 μM GSNO labeled *nt* for clarity.

Table 6.2. Copper concentration of solutions following NO release experiments

Experiment	Copper concentration (mg L^{-1})[a]
25 μM S-nitrosothiol concentration	
GSNO control	< LoD
SNAP control	< LoD
Copper(II) chloride	0.786 ± 0.043
Gold(III) chloride	< LoD
Indium(I) chloride (GSNO)	< LoD
Indium(I) chloride (SNAP)	0.012 ± 0.001
Indium(I) chloride (10 min in water)	< LoD
Indium(II) chloride	< LoD
Indium(I) iodide	0.013 ± 0.009
Iron(II) chloride	< LoD
Sodium tetrachloropalladate(II)	0.028 ± 0.011
Sodium tetrachloroplatinate(II)	< LoD
Tin(II) chloride	< LoD
Zirconyl(IV) chloride	< LoD
250 μM S-nitrosothiol concentration	
GSNO control	0.093 ± 0.001
Aluminum(III) nitrate	< LoD
Chromium(III) chloride	< LoD
Cobalt(II) chloride	< LoD
Copper(II) chloride	1.730 ± 0.020
Gold(III) chloride	< LoD
Hafnium(IV) chloride	< LoD
Indium(0)	< LoD
Indium(I) chloride	< LoD
Indium(II) chloride	< LoD
Indium(III) chloride	< LoD
Indium(I) iodide	< LoD
Iron(II) chloride	< LoD
Iron(III) chloride	< LoD
Lead(II) nitrate	< LoD
Manganese(II) chloride	< LoD
Nickel(II) nitrate	< LoD
Scandium(III) triflate	< LoD
Silver(I) nitrate	< LoD
Sodium tetrachloropalladate(II)	< LoD
Sodium tetrachloroplatinate(II)	< LoD
Tin(II) chloride	< LoD
Vanadium(III) chloride	0.024 ± 0.014
Zinc(II) chloride	< LoD
Zirconyl(IV) chloride	< LoD

[a]After each experiment, solutions of the metal compound and *S*-nitrosothiol were analyzed by ICP-AES to determine the copper concentration (10 ppb LoD). Tabulated data is reported as the mean ± standard deviation

metals, only Cu and Fe ions are widely accepted to directly produce NO *via* decomposition of RSNOs. Krężel *et al.* reported that Ni^{2+} also decomposes GSNO in a concentration-dependent manner.[21] McCarthy *et al.* identified similar behavior in the case of Ni^{2+}, and expanded this activity to Co^{2+} and Zn^{2+}, although the outcome with these examples contradicted previous publications and has remained largely uncorroborated.[20] Our results support the inactivity of Cr^{3+} and Zn^{2+}, although a subtle increase in NO formation from GSNO was detected in the presence of both Co^{2+} and Ni^{2+}. A similarly marginal increase in NO production was observed after the addition of Mn^{2+}, which has been frequently characterized as inactive by Williams and others. Interestingly, it was also observed by Krężel *et al.* that equimolar Zn^{2+} (and to a lesser extent, Cd^{2+}) was able to *decrease* the rate of GSNO decomposition, which was hypothesized to result from binding of trace thiol that is otherwise a participant in the decomposition pathway.[21] We found that the addition of Al^{3+}, Pb^{2+}, or Sc^{3+} does not result in statistically significant acceleration of the NO-forming decomposition of GSNO, while Hf^{4+}, Sn^{2+}, and Zr^{4+} produce effects of a magnitude similar to or greater than the activity of Fe^{2+}. The apparent activity of V^{3+} is perhaps explained by the presence of trace Cu, which is detected by ICP-AES at a concentration of 10^{-7} M. However, GSNO itself contains a detectable quantity of trace Cu that is greater than the contribution from VCl_3 and insufficient to induce significant decomposition. Alternatively, the known ability of V^{3+} to reduce NO_2^- to NO may indicate that HNO_2 liberated by RSNO hydrolysis is the source of the detected NO.[27] In general, our data support observations from Ewing and Janero, who found that V^{3+} forms NO from multiple RSNOs.[28] The ability of noble metals to interact with RSNOs has been the subject of several earlier studies. For example, Jia *et al*. described the use of Au^0 nanoparticles to induce NO formation from *S*-nitroso-*N*-acetylpenicillamine (SNAP).[23] We observed that Au^{3+}, Pd^{2+}, and Pt^{2+} induce NO formation from

GSNO, contrasting with at least one prior report that found no effect in the case of Pt^{2+} and SNAP.[20] The reaction of Hg^{2+} with RSNOs facilitates their rapid hydrolysis to nitrous acid (HNO_2), a process that forms the basis of the Saville assay.[29] It has been observed by Swift and Williams that Ag^+ is similarly able to promote the HNO_2^- forming hydrolysis of RSNOs, albeit at a reduced rate.[19] While we observed minor activity with both Hg^{2+} and Ag^+, the detection of NO is likely to be a consequence of HNO_2 formation and subsequent decomposition to NO.[30]

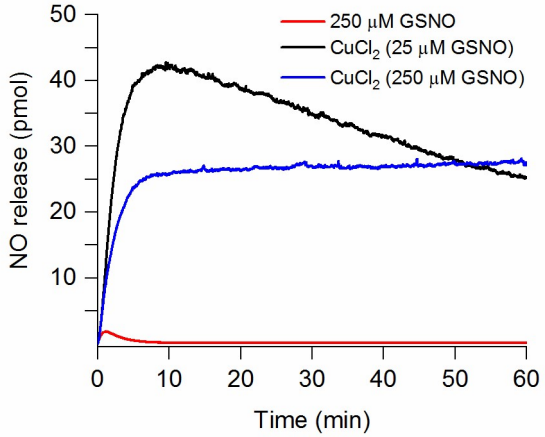

Figure 6.6. Nitric oxide production from 25 µM *S*-nitrosoglutathione (GSNO) in the presence of $CuCl_2$ (black) and 250 µM GSNO in the presence of $CuCl_2$ (blue). Baseline NO release from 250 µM GSNO (red) is provided for comparison. Plotted data are the average of n ≥ 3 replicate experiments.

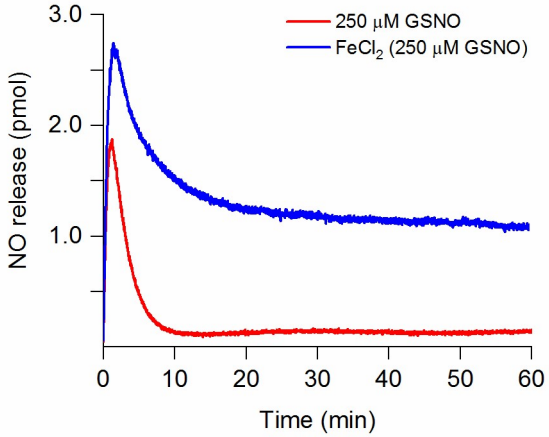

Figure 6.7. Nitric oxide production from 250 µM *S*-nitrosoglutathione (GSNO) in the presence of $FeCl_2$ (blue). Baseline NO release from 250 µM GSNO (red) is provided for comparison. Plotted data are the average of n ≥ 3 replicate experiments.

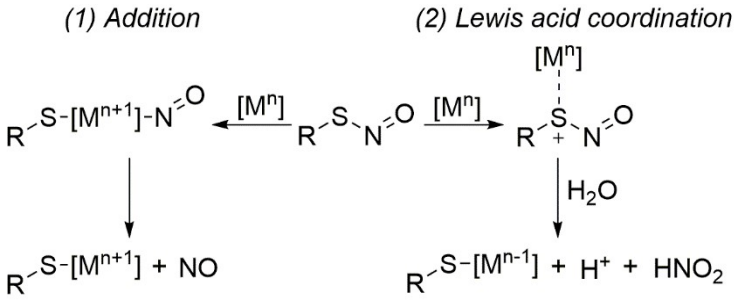

Figure 6.8. Speculative metal-promoted decomposition pathways of *S*-nitrosoglutathione. In the first pathway, the addition of a metal to the S-N bond precedes the production of NO in a manner similar to the behavior of certain copper[26], osmium, or ruthenium complexes.[27] In the second pathway, coordination of a Lewis acidic metal facilitates hydrolysis to HNO_2, which can subsequently decompose to form detectable NO in the absence of O_2.[21]

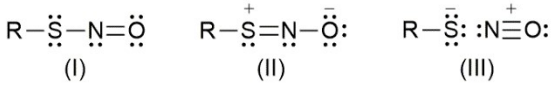

Figure 6.9. Hypothesized resonance structures of *S*-nitrosothiols.

No clear pattern emerges from the data that permits prediction of active metals, especially given the probability that multiple mechanistic pathways lead to the formation of NO (Fig. 6.8). Regardless of whether NO formation occurs directly or through decomposition of HNO_2, it may be reasonable to hypothesize that the activity of many thiophilic metals is indicative of a conserved elementary step: coordination of sulfur to the metal species. The physical and chemical properties of RSNOs have frequently been rationalized through a model that proposes three distinct resonance structures (Fig. 6.9).[31] In this model, coordination of the sulfur atom to a Lewis acid is anticipated to disfavor structure II, which weakens the S-N bond and renders it susceptible to hydrolytic cleavage (e.g., Hg^{2+} in the Saville assay). The thiophilicity of a given metal species may contribute to the likelihood of this outcome. In contrast, coordination by nitrogen and oxygen can stabilize RSNOs.[16,31] Thiophilicity may remain an important factor in

the addition or coordination of RSNOs to metal centers, as in the case of certain copper[32] complexes, as well as ruthenium and osmium metalloporphyrins.[14] In the latter examples, initial coordination of sulfur to the metal center is proposed to precede formal addition. While the formation of these complexes is not uniformly productive with respect to NO, RSNO decomposition by Cu^{+} has been hypothesized to proceed through cyclic metal chelates or addition complexes that involve similar sulfur-metal interactions.[4,32] The notion that favorable sulfur-metal coordination is a critical step in the formation of NO or HNO_2 is apparently contradicted by the activity of strongly oxophilic Lewis acids like Hf^{4+}, V^{3+}, and Zr^{4+}.[33] Moreover, this principle correctly predicts the behavior of certain p-block metals (Sn^{2+}) but not others (Pb^{2+}). It is clear that additional factors beyond thiophilicity alone influence the ability of metal ions to promote NO or HNO_2 formation from GSNO.

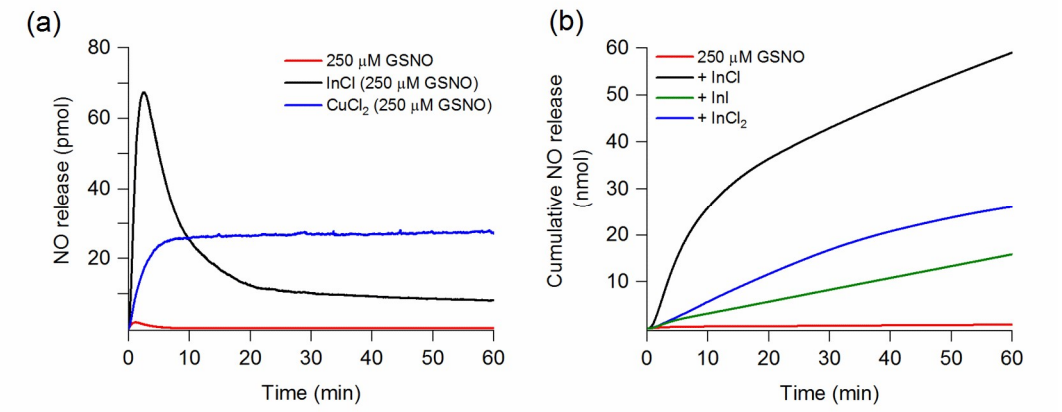

Figure 6.10. (a) Nitric oxide production from 250 µM S-nitrosoglutathione (GSNO) in the presence of InCl (black) or $CuCl_2$ (blue) at 25 °C . Baseline NO release from GSNO (red) is provided for comparison. (b) Cumulative nitric oxide release from 250 µM S-nitrosoglutathione (GSNO) in the presence of InCl (black), InI (green), and $InCl_2$ (blue). Traces for metallic indium and $InCl_3$ are indistinguishable from GSNO alone and are not shown. Plotted data are the average of $n \geq 3$ replicate experiments.

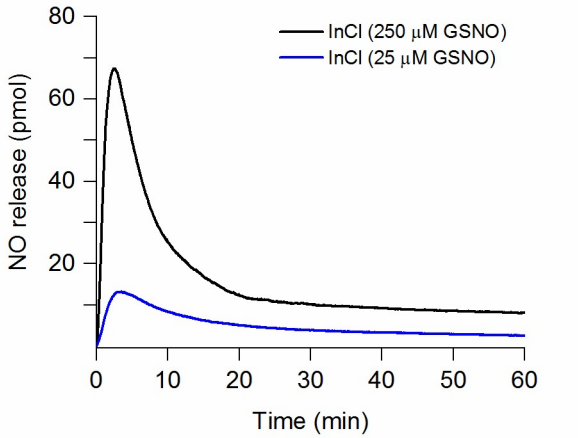

Figure 6.11. Nitric oxide production from 25 μM *S*-nitrosoglutathione (GSNO) in the presence of InCl (blue) and 250 μM GSNO in the presence of InCl (black). Plotted data are the average of $n \geq 3$ replicate experiments.

Curiously, many species that could reasonably be expected to induce the NO-forming decomposition of RSNOs have yet to be investigated. For instance, exploration of the effect of In on RSNOs may be justified by certain chemical similarities between In^+ and Cu^+, which are *superficially* related by the "Knight's Move" pattern described by Laing.[34,35] Inspired by this admittedly tenuous connection, we performed experiments in which 25 or 250 μM GSNO in water was exposed to solid InCl (10 μmol), resulting in the production of NO as determined by chemiluminescence-based detection (Fig. 6.10a, Fig. 6.11). With larger quantities of InCl (≥40 μmol), we found that it was possible to variably recover as much as 50% of theoretical NO (based on the initial amount of GSNO). In these cases, another addition of InCl late in the reaction was not found to produce a significant increase in the rate of NO production or yield. The putative mixed-valence dihalide $InCl_2$ was similarly able to promote NO release from GSNO, presumably through contribution of In^+ rather than activity from a discrete In^{2+} oxidation state (Fig. 6.10b). It is notable that compounds of In^+ exhibit limited aqueous stability and rapidly disproportionate to In^0 and In^{3+}, resulting in the formation of secondary species that

could conceivably be responsible for the decomposition of GSNO.[36] In our study, this disproportionation resulted in the development of grey-white In^0 from the previously yellow InCl sample and the release of In ions into solution at a near-mM concentration. In subsequent experiments, we failed to observe significant NO production from GSNO in the presence of either In^0 or In^{3+} (added as metallic powder or water-soluble $InCl_3$), which was taken as an indication that these oxidation states do not independently contribute to the activity of InCl. The NO-forming reaction was temporarily slowed (but not fully arrested) by metal ion chelators, including EDTA- Na_2 and Cu^+-selective neocuproine. However, the formation of a distinct neocuproine-Cu^+ complex (λ_{max} *ca.* 450 nm)[5] was not observed using UV-Vis spectroscopy, nor was the presence of dissolved Cu detected by ICP-AES. Spectroscopic changes occurred exclusively below 400 nm and overlapped with absorbance bands from neocuproine itself. Moreover, the reaction was never observed to result in quantitative recovery of theoretical NO, as is typically possible in Cu-catalyzed decomposition of RSNOs. Efficiency of the reaction was improved by 38% (25.0 ± 3.2 nmol cumulative NO release) after immersion of InCl in water for 10 min prior to addition of GSNO (25 μM final concentration) (Fig. 6.12). Even after immersion in water for 3 days prior to addition of the GSNO substrate, InCl maintained significant activity. Immersion of InCl in water for 10 min followed by passage of the solution through a sub-micron filter produced a clear filtrate that remained capable of initiating NO formation from GSNO. Permitting the filtrate to stand for 1 day prior to addition of the substrate substantially reduced the NO-forming activity, and it was arrested altogether by EDTA-Na_2. In general, these observations are consistent with a homogeneous active species (most likely In^+) that has a limited lifetime in water before inactivation, rather than a heterogeneous process that is localized to the insoluble solid. Based on the improved reaction efficiency after 10 min of immersion in

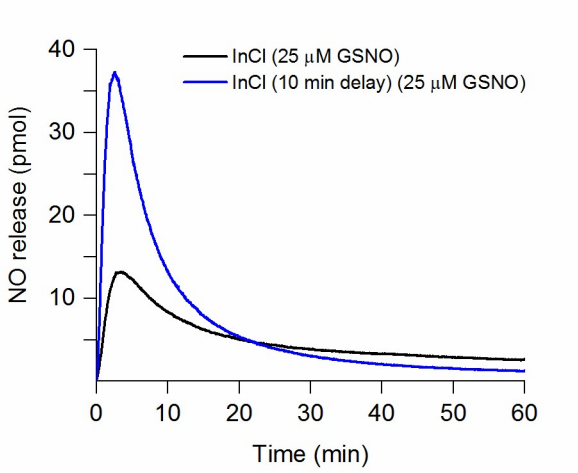

Figure 6.12. Nitric oxide production from 25 μM S-nitrosoglutathione (GSNO) in the presence of InCl under typical experimental conditions (black) and after immersion in water for 10 min prior to the addition of GSNO (blue). Plotted data are the average of n ≥ 3 replicate experiments.

water prior to substrate addition, it may be reasonable to surmise that this period is associated with some degree of accumulation of the active species in solution. To evaluate the ability of an additional In^+ halide species to promote NO release from GSNO, the effect of InI was examined following an identical measurement protocol. We observed that the ability of In^+ to initiate the NO-forming decomposition of GSNO was also exhibited in the monoiodide form, which produced NO at a steady rate over the 1 h measurement period. This behavior contrasts with the apparent exponential decay kinetics observed for the release of NO from GSNO in the presence of InCl, and is attributable to the distinct morphology of InCl powder compared to InI beads, which may result in differences in the availability of the hypothesized In^+ active species. When 25 μM SNAP was used in place of GSNO, InCl was similarly able to induce production of NO (34.1 ± 2.5 nmol), indicating that the scope of the reaction includes both primary (GSNO) and tertiary (SNAP) RSNO substrates.

Regardless of the In^+ source, NO is undoubtedly formed as a product of its interaction with RSNOs, yet it remains unclear if this occurs through direct generation of NO (as in the case

of Cu^{+}) or through formation of HNO_2 that subsequently decomposes to NO. In either event, the yield of NO is neither quantitative nor significantly improved by a subsequent addition of InCl. This may suggest a complex overall reaction in which NO is not produced stoichiometrically from the RSNO substrate, perhaps supporting the intermediacy of HNO_2 or formation of other nitrogen oxide species. However, the comparatively poor Lewis acidity[36] of In^{+} (particularly in comparison to inactive In^{3+}) indicates that HNO_2-forming hydrolysis is an unlikely pathway. Moreover, Lewis acid-promoted formation of HNO_2 presumably requires sufficient metal thiophilicity (*e.g.*, Hg^{2+}) to trap thiolate and prevent reversal of the reaction. As an alternative hypothesis, NO production following oxidative addition of In^{+} to the S-N bond may proceed in a manner analogous to the activity of certain Cu^{+} complexes.[32] A mechanism of this type is generally more consistent with the known behavior of low-valent In, and various semi-stable In^{+}/In^{3+} thiolates have been electrochemically prepared that could serve as intermediates.[37] When characterized by ^{1}H NMR, the organic product of the InCl/GSNO reaction was unambiguously derived from the general tripeptide structure of glutathione, but was distinct from both oxidized and reduced glutathione (Fig. 6.13-6.15). A control experiment performed without the addition of InCl resulted in significant retention of GSNO, as well as clear formation of the disulfide (Fig. 3.16). In contrast, GSNO was no longer present following reaction with InCl. The significant downfield shift of the glutamyl α-proton (*ca.* 1 ppm) in the organic product supports reaction of the amine group (perhaps simply through protonation), yet a shift of this magnitude could not be independently achieved by dissolution of oxidized or reduced glutathione in 1 M DCl/D_2O. Mass spectrometry failed to identify a distinguishable organic product during reaction with InCl (Fig. 6.17 and 6.18).

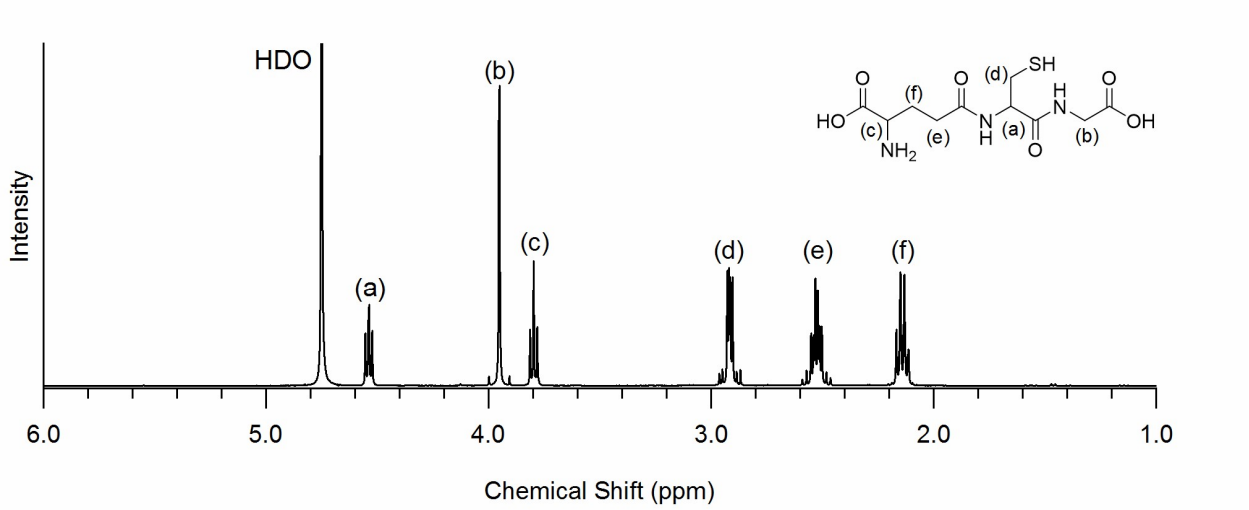

Figure 6.13. ^{1}H NMR spectrum of reduced glutathione (GSH). Spectrum acquired in D_2O at 25 °C.

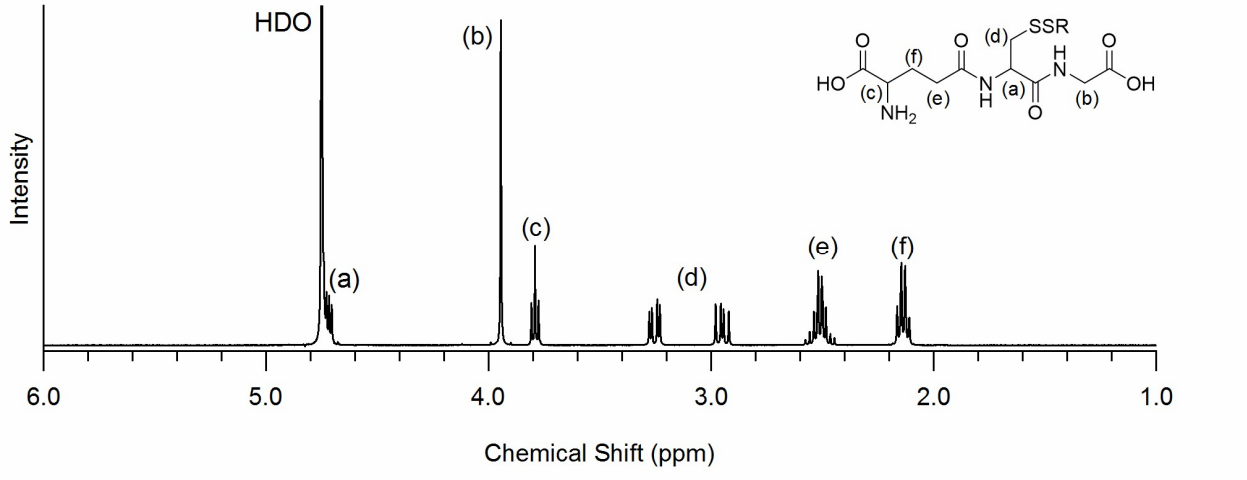

Figure 6.14. ^{1}H NMR spectrum of oxidized glutathione (GSSG). Spectrum acquired in D_2O at 25 °C.

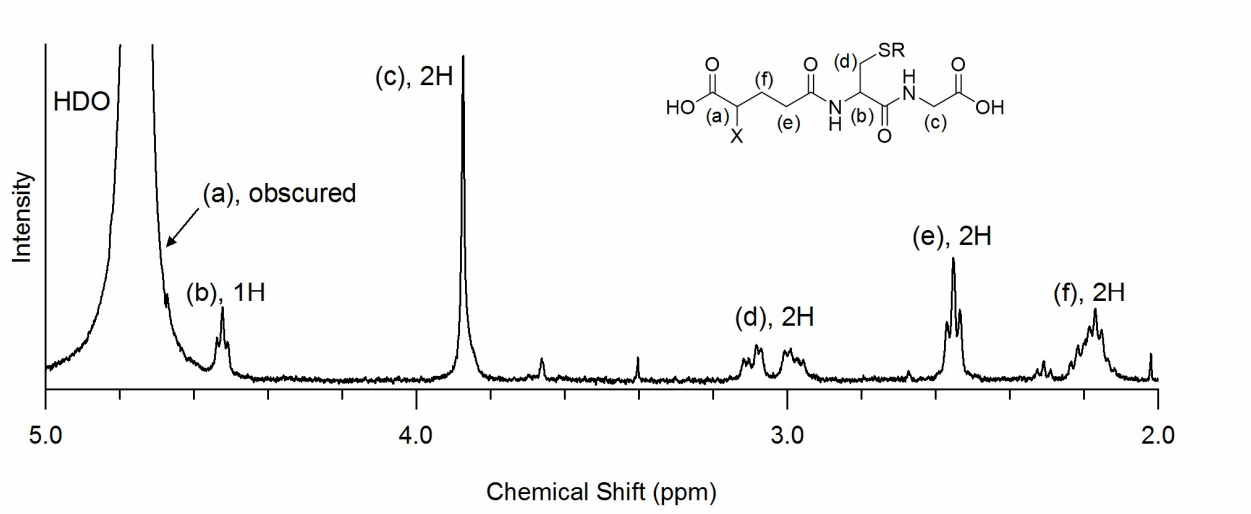

Figure 6.15. Analysis of indium-mediated decomposition products by ^{1}H NMR: the spectrum of GSNO decomposed under N_2 purge in the presence of indium(I) chloride. Spectrum acquired in D_2O at 25 °C.

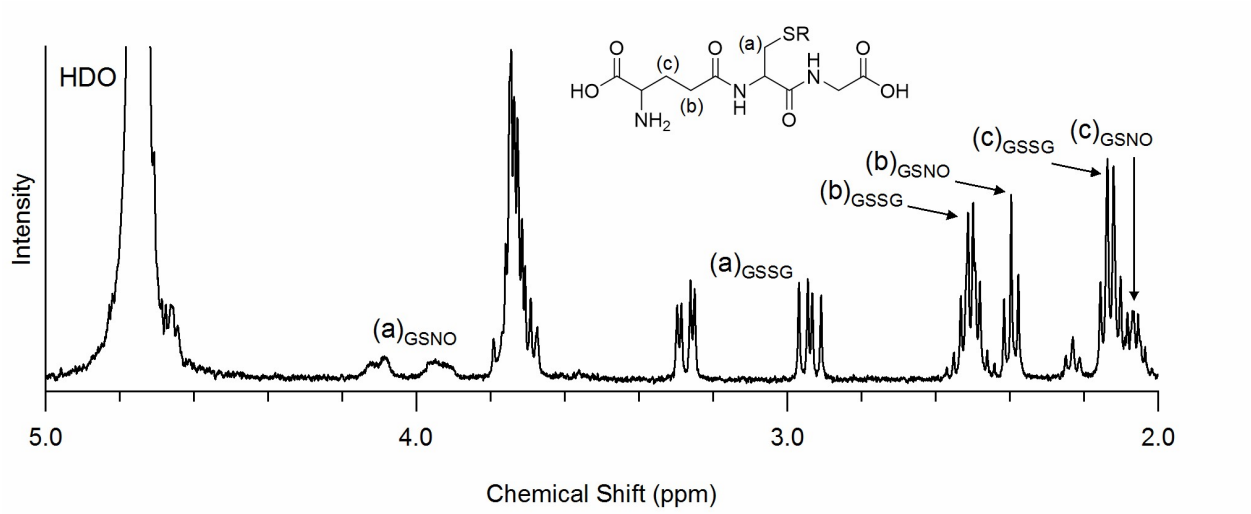

Figure 6.16. The spectrum of GSNO decomposed under N_2 purge in the *absence* of indium(I) chloride. This spectrum depicts the anticipated formation of GSSG from GSNO, and both compounds are distinguishable by chemical shift. Spectrum acquired in D_2O at 25 °C.

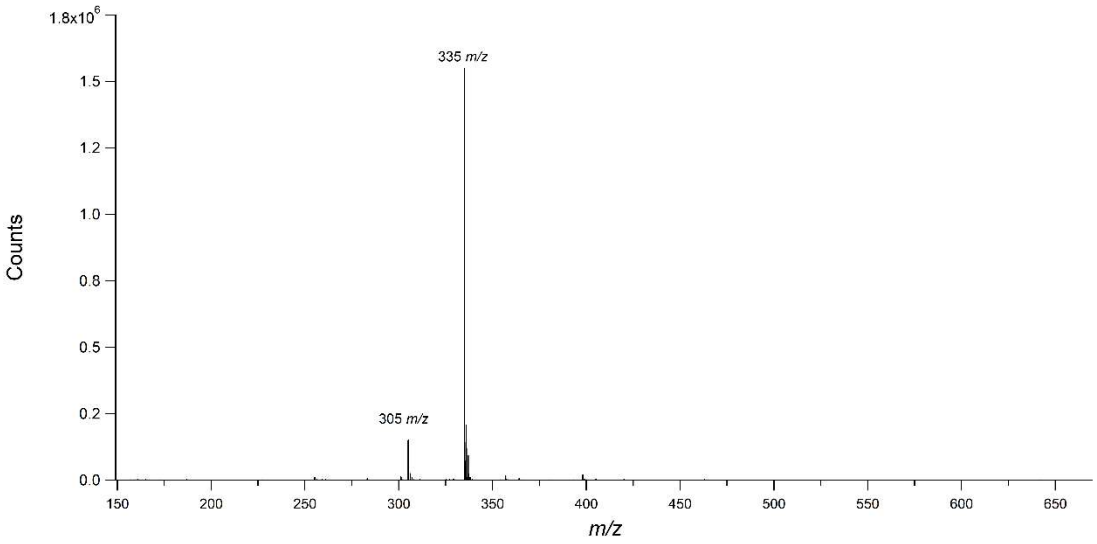

Figure 6.17. Mass spectrum of *S*-nitrosoglutathione (GSNO) in negative ion mode. The ion at 335 *m/z* is assigned to GSNO ($C_{10}H_{15}N_4O_7S^-$, $[M-H]^-$). The ion at 305 *m/z* is assigned to the thiyl radical formed from GSNO after homolytic cleavage of the S-N bond under ESI conditions ($C_{10}H_{15}N_3O_6S^{\cdot -}$, $[M-NO-H]^{\cdot -}$).

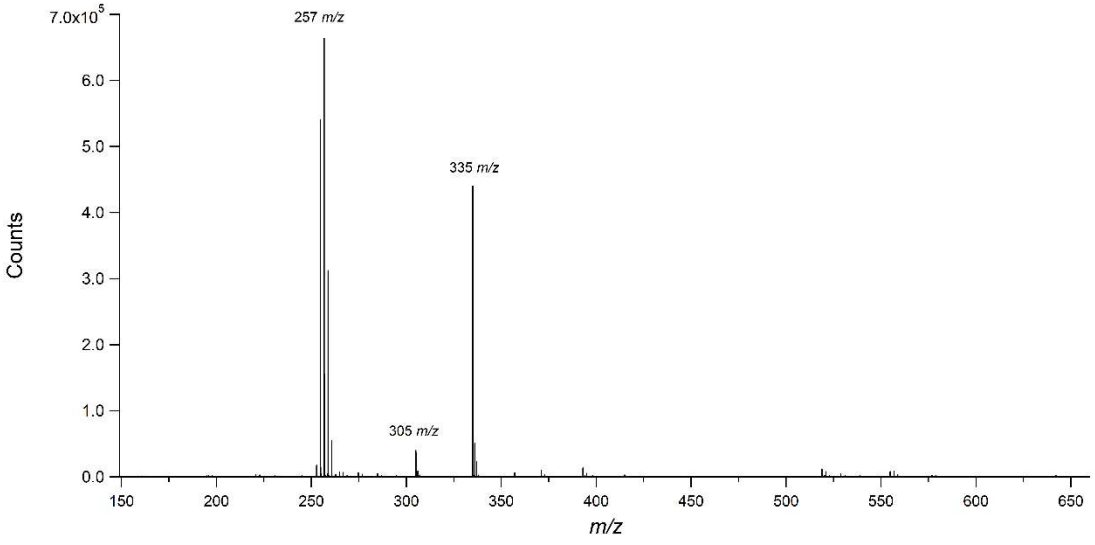

Figure 6.18. Mass spectrum of GSNO during reaction with InCl. The ions associated with GSNO itself (305 and 335 *m/z*) remain detectable, yet no distinct organic product is present. The cluster of peaks at 257 m/z can be assigned to an indium complex with the formula $InCl^{4-}$.

6.5 Conclusions

Our study indicates that a number of transition and post-transition metal ions are able to induce detectable NO release from GSNO, and that this activity includes a much broader variety of metal species than were previously identified. The established chemistry of RSNOs permits the prediction of two general reaction pathways: (a) the direct, NO-forming interaction of metal ions with RSNOs, and (b) hydrolysis of RSNOs to yield HNO_2, which subsequently decomposes to form a measurable gas-phase concentration of NO. It is reasonable to surmise that the latter pathway is significant exclusively in cases where the metal species possesses sufficient thiophilicity to inhibit the reverse reaction, or when such as a reversal is otherwise disfavored (*i.e.*, when rapid removal or consumption of HNO_2 prevails). The majority of practical applications for metal ion-induced RSNO decomposition are currently achieved through the use of Cu^{2+}/Cu^{+}. Moreover, many fundamental studies of RSNO interactions with metal ions are limited to Cu^{2+}/Cu^{+}, Fe^{2+}, and a small selection of other transition metals, yet it is clear that other species have NO-forming effects that merit further examination. In particular, the previously unknown activity of In^{+} is both unusual and distinctly confined to the low-valent form, in a manner that is potentially analogous to the behavior of Cu^{+}. The fact that In^{+} compounds must be added as measurable quantities of solid limits our ability to assess the comparative activity of InCl/InI relative to soluble metal species. This inherent limitation is compounded by the propensity of In^{+} compounds to disproportionate to In^{0}/In^{3+}. For these reasons, the precise concentration of the active species is unknown and it may be present in a significant excess over other tested species. At this stage, the stoichiometry associated with the reaction of In^{+} with RSNOs is uncertain, and the exact nature of the products and their comparative distribution is similarly undetermined. Moreover, the practical use of In^{+} species for NO generation from

RSNOs is clearly limited by the considerations addressed earlier. Nevertheless, further study of this system may provide useful mechanistic insight into metal-promoted decomposition of RSNOs.

CHAPTER 6

REFERENCES

(1) Giustarini, D.; Milzani, A.; Dalle-Donne, I.; Rossi, R. Detection of S-Nitrosothiols in Biological Fluids: A Comparison among the Most Widely Applied Methodologies. *J. Chromatogr. B Anal. Technol. Biomed. Life Sci.* **2007**, *851* (1–2), 124–139.

(2) Butler, A. R.; Williams, D. L. H. The Physiological Role of Nitric Oxide. *Chem. Soc. Rev.* **1993**, *22* (4), 233–241.

(3) Witte, M. B.; Barbul, A. Role of Nitric Oxide in Wound Repair. *Am. J. Surg.* **2002**, *183* (4), 406–412.

(4) Williams, D. L. H. The Chemistry of S-Nitrosothiols. *Acc. Chem. Res.* **1999**, *32* (10), 869–876.

(5) Dicks, A. P.; Swift, H. R.; Williams, D. L. H.; Butler, A. R.; Al-sa, H. H.; Cox, B. G. Identification of Cu+ as the Effective Reagent in Nitric Oxide Formation from S-Nitrosothiols (RSNO). *J. Chem. Soc., Perkin Trans. 2* **1996**, 2, 481–487.

(6) Vanin, A. F.; Malenkova, I. V; Serezhenkov, V. A. Iron Catalyzes Both Decomposition and Synthesis of *S*-Nitrosothiols: Optical and Electron Paramagnetic Resonance Studies. *Nitric Oxide – Biol. and Chem.* **1997**, *1* (3), 191–203.

(7) Wo, Y.; Brisbois, E. J.; Bartlett, R. H.; Meyerhoff, M. E. Recent Advances in Thromboresistant and Antimicrobial Polymers for Biomedical Applications: Just Say Yes to Nitric Oxide (NO). *Biomater. Sci.* **2016**, *4* (8), 1161–1183.

(8) Oh, B. K.; Meyerhoff, M. E. Spontaneous Catalytic Generation of Nitric Oxide from S-Nitrosothiols at the Surface of Polymer Films Doped with Lipophilic Copper(II) Complex. *J. Am. Chem. Soc.* **2003**, *125* (32), 9552–9553.

(9) Neufeld, M. J.; Lutzke, A.; Jones, W. M.; Reynolds, M. M. Nitric Oxide Generation from Endogenous Substrates Using Metal-Organic Frameworks: Inclusion within Poly(Vinyl Alcohol) Membranes to Investigate Reactivity and Therapeutic Potential. *ACS Appl. Mater. Interfaces* **2017**, *9* (41), 35628–35641.

(10) Major, T. C.; Brant, D. O.; Burney, C. P.; Amoako, K. A.; Annich, G. M.; Meyerhoff, M. E.; Handa, H.; Bartlett, R. H. The Hemocompatibility of a Nitric Oxide Generating Polymer That Catalyzes S-Nitrosothiol Decomposition in an Extracorporeal Circulation Model. *Biomaterials* **2011**, *32* (26), 5957–5969.

(11) Stamler, J. S.; Toone, E. J. The Decomposition of Thionitrites. *Curr. Opin. Chem. Biol.* **2002**, *6* (6), 779–785.

(12) Hart, T. W. SOME OBSERVATIONS CONCERNING THE S-NITROSO AND S-PHENYLSULPHONYL DERIVATIVES OF L-CYSTEINE AND GLUTATHIONE. *Tetrahedron Lett.* **1985**, *26* (16), 2013–2016.

(13) Field, L.; Dilts, R. V.; Ravichandran, R.; Lenhert, P. G.; Carnahan, G. E. An Unusually Stable Thionitrite from N-Acetyl-D,L-Penicillamine; X-Ray Crystal and Molecular Structure of 2-(Acetylamino)-2-Carboxy-l,Ldimethylethyl Thionitrite. *J. C. S. Chem. Comm.* **1978**, 249–250.

(14) Richter-Addo, G. B. Binding of Organic Nitroso Compounds to Metalloporphyrins. *Acc. Chem. Res.* **1999**, *32* (6), 529–536.

(15) Lee, J.; Yi, G.-B.; Powell, D. R.; Khan, M. A.; Richter-Addo, G. B. Synthesis, Characterization, and Protonation of Octaethylporphyrin Osmium Nitrosyl Complexes Containing Axial Thiolate Ligands - X-Ray Structures of an Alkyl Thionitrite (RSNO) and Its (OEP)Os(NO)(SR) Addition Product. *Can. J. Chem.* **2011**, *79* (5–6), 830–840.

(16) Perissinotti, L. L.; Estrin, D. A.; Leitus, G.; Doctorovich, F. A Surprisingly Stable S-Nitrosothiol Complex. *J. Am. Chem. Soc.* **2006**, *128* (8), 2512–2513.

(17) Cha, W.; Meyerhoff, M. E. Catalytic Generation of Nitric Oxide from S-Nitrosothiols Using Immobilized Organoselenium Species. *Biomaterials* **2007**, *28* (1), 19–27.

(18) Meyerhoff, M. E.; Hwang, S. Organoditelluride-Tethered Polymers That Spontaneously Generate Nitric Oxide When in Contact with Fresh Blood. *J. Mater. Chem.* **2008**, *18* (15), 1784–1791.

(19) Swift, H. R.; Williams, D. L. H. Decomposition of S-Nitrosothiols by Mercury (II) and Silver Salts. *J. Chem. Soc. Perkin Trans. 2* **1997**, *2*, 1933–1935.

(20) McCarthy, C. W.; Guillory, R. J.; Goldman, J.; Frost, M. C. Transition-Metal-Mediated Release of Nitric Oxide (NO) from S-Nitroso-N-Acetyl-D-Penicillamine (SNAP): Potential Applications for Endogenous Release of NO at the Surface of Stents Via Corrosion Products. *ACS Appl. Mater. Interfaces* **2016**, *8* (16), 10128–10135.

(21) Krężel, A.; Bal, W. Contrasting Effects of Metal Ions on S-Nitrosoglutathione, Related to Coordination Equilibria: GSNO Decomposition Assisted by Ni(II) vs Stability Increase in the Presence of Zn(II)and Cd(II). *Chem. Res. Toxicol.* **2004**, *17* (3), 392–403.

(22) Cao, G. J.; Fisher, C. M.; Jiang, X.; Chong, Y.; Zhang, H.; Guo, H.; Zhang, Q.; Zheng, J.; Knolhoff, A. M.; Croley, T. R.; et al. Platinum Nanoparticles: An Avenue for Enhancing

the Release of Nitric Oxide from: *S*-Nitroso-*N*-Acetylpenicillamine and *S*-Nitrosoglutathione. *Nanoscale* **2018**, *10* (23), 11176–11185.

(23) Jia, H.; Han, X.; Li, Z.; Tian, Q.; Miao, X.; Du, L.; Liu, Y. Gold Nanoparticles-Based Catalysis for Detection of S-Nitrosothiols in Blood Serum. *Talanta* **2011**, *85* (4), 1871–1875.

(24) Noble, D. R.; Swift, H. R.; Williams, D. L. H. Nitric Oxide Release from *S*-Nitrosoglutathione (GSNO). *Chem. Commun.* **1999**, No. 22, 2317–2318.

(25) Noble, D. R.; Williams, D. L. H. Structure-Reactivity Studies of the Cu^{2+}-Catalyzed Decomposition of Four S-Nitrosothiols Based around the *S*-Nitrosocysteine/*S*-Nitrosoglutathione Structures. *Nitric Oxide - Biol. Chem.* **2000**, *4* (4), 392–398.

(26) de Oliveira, M. G.; Shishido, S. M.; Seabra, A. B.; Morgon, N. H. Thermal Stability of Primary *S*-Nitrosothiols: Roles of Autocatalysis and Structural Effects on the Rate of Nitric Oxide Release. *J. Phys. Chem. A* **2002**, *106* (38), 8963–8970.

(27) Braman, R. S.; Hendrix, S. A. Nanogram Nitrite and Nitrate Determination in Environmental and Biological Materials by Vanadium(III) Reduction with Chemiluminescence Detection. *Anal. Chem.* **1989**, *61* (24), 2715–2718.

(28) Ewing, J. F.; Janero, D. R. Specific S-Nitrosothiol (Thionitrite) Quantification as Solution Nitrite after Vanadium(III) Reduction and Ozone-Chemiluminescent Detection. *Free Radic. Biol. Med.* **1998**, *25* (4–5), 621–628.

(29) Saville, B. A Scheme for the Colorimetric Determination of Microgram Amounts of Thiols. *Analyst* **1958**, *83*, 670–672.

(30) Park, J. Y.; Lee, Y. N. Solubility and Decomposition Kinetics of Nitrous Acid in Aqueous Solution. *J. Phys. Chem.* **1988**, *92* (22), 6294–6302.

(31) Timerghazin, Q. K.; Peslherbe, G. H.; English, A. M. Resonance Description of *S*-Nitrosothiols: Insights into Reactivity. *Org. Lett.* **2007**, *9* (16), 3049–3052.

(32) Melzer, M. M.; Mossin, S.; Cardenas, A. J. P.; Williams, K. D.; Zhang, S.; Meyer, K.; Warren, T. H. A Copper(II) Thiolate from Reductive Cleavage of an *S*-Nitrosothiol. *Inorg. Chem.* **2012**, *51* (16), 8658–8660.

(33) Kepp, K. P. A Quantitative Scale of Oxophilicity and Thiophilicity. *Inorg. Chem.* **2016**, *55* (18), 9461–9470.

(34) Laing, M. The Knight's Move in the Periodic Table. *S. Afr. J. Sci* **1991**, *87*, 285–287.

(35) Rayner-Canham, G.; Oldford, M. The Chemical "Knight's Move" Relationship: What Is Its Significance? *Found. Chem.* **2007**, *9* (2), 119–125.

(36) Pardoe, J. A. J.; Downs, A. J. Development of the Chemistry of Indium in Formal Oxidation States Lower than +3. *Chem. Rev.* **2007**, *107* (1), 2–45.

(37) Green, J. H.; Kumar, R.; Seudeal, N.; Tuck, D. G. Direct Electrochemical Synthesis of Alkane- and Arenethiolato Derivatives of Indium and Thallium. *Inorg. Chem*. **1989**, *28* (1), 123–127.